

One World Archaeology

Thomas E. Levy  
Ian W.N. Jones *Editors*

# Cyber-Archaeology and Grand Narratives

Digital Technology and Deep-Time  
Perspectives on Culture Change in the  
Middle East

 Springer

# One World Archaeology

## **Series Editors:**

K. Anne Pyburn  
Indiana University  
Department of Anthropology  
Bloomington, IN, USA

Arwa Badran  
The Hashemite University  
Zarqa, Jordan

More information about this series at <http://www.springer.com/series/8606>

Thomas E. Levy • Ian W.N. Jones  
Editors

# Cyber-Archaeology and Grand Narratives

Digital Technology and Deep-Time  
Perspectives on Culture Change  
in the Middle East

 Springer

*Editors*

Thomas E. Levy  
University of California, San Diego  
La Jolla, CA, USA

Ian W.N. Jones  
University of California, San Diego  
La Jolla, CA, USA

One World Archaeology

ISBN 978-3-319-65692-2

ISBN 978-3-319-65693-9 (eBook)

<https://doi.org/10.1007/978-3-319-65693-9>

Library of Congress Control Number: 2017953786

© Springer International Publishing AG 2018

This work is subject to copyright. All rights are reserved by the Publisher, whether the whole or part of the material is concerned, specifically the rights of translation, reprinting, reuse of illustrations, recitation, broadcasting, reproduction on microfilms or in any other physical way, and transmission or information storage and retrieval, electronic adaptation, computer software, or by similar or dissimilar methodology now known or hereafter developed.

The use of general descriptive names, registered names, trademarks, service marks, etc. in this publication does not imply, even in the absence of a specific statement, that such names are exempt from the relevant protective laws and regulations and therefore free for general use.

The publisher, the authors and the editors are safe to assume that the advice and information in this book are believed to be true and accurate at the date of publication. Neither the publisher nor the authors or the editors give a warranty, express or implied, with respect to the material contained herein or for any errors or omissions that may have been made. The publisher remains neutral with regard to jurisdictional claims in published maps and institutional affiliations.

Printed on acid-free paper

This Springer imprint is published by Springer Nature

The registered company is Springer International Publishing AG

The registered company address is: Gewerbestrasse 11, 6330 Cham, Switzerland

# Preface

This volume focuses on cyber-archaeology in the Middle East, particularly the Seventh World Archaeology Congress (WAC-7), held along the beautiful shores of the Dead Sea in Jordan between 14 and 18 January 2013. The meetings took place at the palatial King Hussein Bin Talal Convention Centre at the Dead Sea in the most relaxed, efficient, and hospitable context that can only occur in Jordan. The general theme of WAC-7 was “Preservation and Heritage Identities in Times of Conflict.” WAC-7 happened before the advent of the Islamic State (ISIS) targeting of UNESCO World Heritage Sites and the recent destruction of so many archaeological and cultural heritage sites in Iraq, Syria, and other parts of the Arab world. The chapters in this volume have evolved since 2013 and include papers that were not presented at the WAC-7 conference. However, they all reflect a concern with the preservation of Middle Eastern archaeological sites and the application of the digital data capture, curation, analysis, and dissemination tools of cyber-archaeology — the marriage of archaeology, computer science, engineering, and the natural sciences (Levy 2013). My own time spent on preparing this publication has been a result of a University of California Office of the President (UCOP) Catalyst grant that deals with “At-Risk World Heritage and the Digital Humanities,” for which I serve as the principal investigator. This UCOP Catalyst project focuses specifically on at-risk archaeological sites in the Middle East. Unfortunately, this is an ever-evolving problem for our region, and all the contributors to this volume are using cyber-archaeology not only to preserve Middle East cultural heritage but also for scientific storytelling to create grand narratives of culture change in the region.

At the WAC-7 conference, the organizers asked those of us who work in Jordan to highlight the scientific methods we develop and employ in that country. In our WAC-7 sessions, there were a number of papers from the University of California, San Diego, Edom Lowlands Regional Archaeology Project (ELRAP), which I co-direct with my friend and colleague Mohammad Najjar. Over the years since WAC-7, we published those papers in a wide range of publications, including peer-reviewed journals (Levy et al. 2014a; Ben-Yosef and Levy 2014; Gidding et al. 2014; Howland et al. 2014a, 2014b; Jones et al. 2014; Knabb et al. 2014; Levy 2014; Levy et al. 2014c; Petrovic et al. 2014; Savage and Levy 2014; Smith and Levy 2014; Smith et al. 2014; Vincent

et al. 2014a, 2014b) and a large two-volume study (Levy et al. 2014b) of Iron Age metal production and social evolution in Jordan's Faynan region. Thus, those WAC-7 papers are not presented in this volume as they have been published elsewhere.

It is important to highlight that our UC San Diego–Department of Antiquities of Jordan project in Faynan began in 1997 as an analogue project with excavations at the WFD 40 Iron Age Cemetery and Early Bronze I WFD 4 sites (Levy et al. 1999). By 1998, we carried out an archaeological survey along the Wadi Fidan where we began to implement some aspects of digital recording linked to the use of a Total Station (Levy et al. 2001a). However, it was in the fall of 1999 (Levy et al. 2001b) when our team went totally “paperless” and relied entirely on a digital recording system for the excavation of the Pre-Pottery Neolithic site at Tell Tifdan (WFD 001) and the Early Bronze Age III–IV copper production site at Khirbat Hamra Ifdan (Levy et al. 2002). The transition from analogue archaeology to digital archaeology was painful to say the least. There were sleepless nights and endless troubleshooting. However, the system worked and provided the basis for what has become a seamless digital data recording, curation, and dissemination excavation program. I did not know it then in 1999, but by “going digital” and using a geo-spatial database founded on the recording of X, Y, and Z (elevation) coordinates for every artifact and piece of data recorded in our Faynan region excavations, our research was “pre-adapted” to the world of scientific visualization at Qualcomm Institute, California Institute for Telecommunications and Information Technology (Calit2), University of California–San Diego (<http://calit2.net>). This has led to our UC San Diego team playing a significant role in the development of cyber-archaeology on the world scene (Forte 2008, 2010; Forte et al. 2012, 2015; Levy 2013, 2014; Levy et al. 2010, 2012, 2013; Lercari et al. 2016), as highlighted by this WAC-7 publication.

WAC-7's Academic Secretary, Talal Akasheh, and WAC's International Academic Secretary, Claire Smith, are to be congratulated for the excellent organization of the conference that welcomed participants from all the countries of the Middle East and world community. I would like to personally thank Anne Pyburn and Arwa Badran, the editors of the WAC-7 publication series, for their support in publishing this volume. Special thanks go to Teresa M. Krauss, the senior editor for Social Sciences at Springer in New York, for all her advice and help during the production of this book. I would also like to thank my colleagues from Calit2's Qualcomm Institute at UC San Diego for their support in the activities of the Center for Cyber-Archaeology and Sustainability: Ramesh Rao, Larry Smarr, Tom DeFanti, Margie Burton, Jurgen Schulze, Falko Kuester, Joe Keefe, Greg Dawe, Lisa Tauxe, Steve Savage, Philip Weber, and Chris McFarland. Special thanks also go to my former and current graduate students who have helped to develop cyber-archaeology in Jordan: Adolfo Muniz, Margie Burton, Yoav Arbel, Neil Smith, Marc Beherec, Erez Ben-Yosef, Kyle Knabb, Aaron Gidding, Kathleen Bennallack, Matt Vincent, Sowparnika Balaswaminathan, Matt Howland, Ian Jones (especially with regard to this volume), Brady Liss, Craig Smitheram, and Tony Tamberino. Finally, I am grateful to Mohammad Najjar and Alina Levy for making cyber-archaeology possible in Jordan and at home.

## References

- Ben-Yosef, E., & Levy, T. E. (2014). A ‘small town’ discovered twice: A forgotten report of major H.H. Kitchener. *Palestine Exploration Quarterly*, 146(3), 179–184.
- Forte, M. (2008). Cyber-archaeology: An eco-approach to the virtual reconstruction of the past. In *14th international conference on virtual systems and multimedia, Larnaca, Cyprus*. Larnaca.
- Forte, M. (Ed.). (2010). *Cyber-archaeology*. Oxford: Archaeopress.
- Forte, M., Dell’Unto, N., Issavi, J., Onsurez, L., & Lercari, N. (2012). 3D archaeology at Çatalhöyük. *International Journal of Heritage in the Digital Era*, 3, 351–378.
- Forte, M., Dell’Unto, N., Kristina, J., & Lercari, N. (2015). Interpretation process at Çatalhöyük using 3D. In I. Hodder, & M. Arkadiusz (Eds.), *Assembling Çatalhöyük* (pp. 43–57). Leeds: Maney Publishing.
- Gidding, A., Levy, T. E., & DeFanti, T. A. (2014). ArchaeoSTOR: The development and utilization of a web-based database for the field and lab. *Near Eastern Archaeology*, 77(3), 198–202.
- Howland, M. D., Kuester, F., & Levy, T. E. (2014a). Photogrammetry in the field: Documenting, recording, and presenting archaeology. *Mediterranean Archaeology and Archaeometry*, 14(4), 101–108.
- Howland, M. D., Kuester, F., & Levy, T. E. (2014b). Structure from motion: Twenty-first century field recording with 3D technology. *Near Eastern Archaeology*, 77(3), 187–191.
- Jones, I. W. N., Najjar, M., & Levy, T. E. (2014). “Not found in the order of history”: Toward a “medieval” archaeology of Southern Jordan. In S.D. Stull (Ed.), *From West to East: Current Approaches to Medieval Archaeology* (pp. 179–205). Newcastle-upon-Tyne: Cambridge Scholars Publishing.
- Knabb, K. A., Schulze, J. P., Kuester, F., DeFanti, T. A., & Levy, T. E. (2014). Scientific visualization, 3D immersive virtual reality environments, and archaeology in Jordan and the Near East. *Near Eastern Archaeology*, 77(3), 228–232.
- Lercari, N., Schulze, J., Wendrich, W. Z., Porter, B., & Levy, T. E. (2016). 3-D Digital preservation of at-risk global cultural heritage. In C.E. Catalano, & L. De Luca (Eds.), *Eurographics workshop on graphics and cultural heritage, 2016*. Aire-la-Ville: Eurographics Association. doi: [10.2312/gch.20161395](https://doi.org/10.2312/gch.20161395).
- Levy, T. E. (2013). Cyber-archaeology and world cultural heritage: Insights from the Holy Land. *Bulletin of the American Academy of Arts and Sciences*, LXVI, 26–33.
- Levy, T. E. (Ed.). (2014). Cyber-archaeology [Special issue]. *Near Eastern Archaeology*, 77(3).
- Levy, T. E., Adams, R. B., & Shafiq, R. (1999). The Jabal Hamrat Fidan Project: Excavations at the Wadi Fidan 40 Cemetery, Jordan (1997). *Levant*, 31, 293–308.
- Levy, T. E., Adams, R. B., Witten, A. J., Anderson, J., Arbel, Y., Kuah, S., et al. (2001a). Early metallurgy, interaction, and social change: The Jabal Hamrat Fidan (Jordan) research design and 1998 archaeological survey: Preliminary report. *Annual of the Department of Antiquities of Jordan*, 45, 159–187.
- Levy, T. E., Anderson, J. D., Waggoner, M., Smith, N., Muniz, A., & Adams, R. B. (2001b). Interface: Archaeology and technology – Digital archaeology 2001: GIS-based excavation recording in Jordan. *The SAA Archaeological Record*, 1(3), 23–29.
- Levy, T. E., Adams, R. B., Hauptmann, A., Prange, M., Schmitt-Strecker, S., & Najjar, M. (2002). Early bronze age metallurgy: A newly discovered copper manufactory in Southern Jordan. *Antiquity*, 76(292), 425–437.
- Levy, T. E., Petrovic, V., Wypych, T., Gidding, A., Knabb, K., Hernandez, D., et al. (2010). On-site digital archaeology 3.0 and cyber-archaeology: Into the future of the past – New developments, delivery and the creation of a data avalanche. In M. Forte (Ed.), *Introduction to cyber-archaeology* (pp. 135–153). Oxford: Archaeopress.
- Levy, T. E., Smith, N. G., Najjar, M., DeFanti, T. A., Yu-Min Lin, A., & Kuester, F. (2012). *Cyber-archaeology in the Holy Land: The future of the past*. Washington, DC: Biblical Archaeology Society eBook.

- Levy, T. E., Tuttle, C. A., Vincent, M., Howland, M., Richter, A., Petrovic, V., et al. (2013). The 2012 petra cyber-archaeology cultural conservation expedition: Temple of the winged lions and environs, Jordan. *Antiquity (Project Gallery)*, <http://antiquity.ac.uk/projgall/levy335/>
- Levy, T. E., Munger, S., & Najjar, M. (2014a). A newly discovered scarab of Sheshonq I: Recent iron age explorations in southern Jordan. *Antiquity*, 341. <http://journal.antiquity.ac.uk/projgall/levy341>
- Levy, T. E., Najjar, M., & Ben-Yosef, E. (Eds.). (2014b). *New insights into the iron age archaeology of Edom, Southern Jordan — surveys, excavations and research from the Edom Lowlands regional archaeology project (ELRAP)*. Los Angeles: Cotsen Institute of Archaeology Press.
- Levy, T. E., Vincent, M. L., Howland, M., Kuester, F., & Smith, N. G. (2014c). The art of implementing SfM for reconstruction of archaeological sites in Greece: Preliminary applications of cyber-archaeological recording at Corinth. *Mediterranean Archaeology and Archaeometry*, 14(4), 125–133.
- Petrovic, V., Vanoni, D. J., Richter, A. M., Levy, T. E., & Kuester, F. (2014). Visualizing high resolution three-dimensional and two-dimensional data of cultural heritage sites. *Mediterranean Archaeology and Archaeometry*, 14(4), 93–100.
- Savage, S., & Levy, T. E. (2014). DAAHL – The digital archaeological atlas of the Holy Land: A model for mediterranean and world archaeology. *Near Eastern Archaeology*, 77(3), 243–247.
- Smith, N. G., & Levy, T. E. (2014). ArchField in Jordan: Real-time GIS data recording for archaeological excavations. *Near Eastern Archaeology*, 77(3), 166–169.
- Smith, N. G., Passone, L., al-Said, S., al-Farhan, M., & Levy, T. E. (2014). Drones in archaeology: Integrated data capture, processing, and dissemination in the al-Ula Valley, Saudi Arabia. *Near Eastern Archaeology*, 77(3), 176–181.
- Vincent, M. L., Kuester, F., & Levy, T. E. (2014a). OpenDig: Contextualizing the past from the field to the web. *Mediterranean Archaeology and Archaeometry*, 14(4), 109–116.
- Vincent, M. L., Kuester, F., & Levy, T. E. (2014b). OpenDig: Digital field archaeology, curation, publication, and dissemination. *Near Eastern Archaeology*, 77(3), 204–208.

# Contents

|          |  |            |
|----------|--|------------|
| <b>1</b> | <b>Cyber-archaeology and Grand Narratives:<br/>Where Do We Currently Stand? . . . . .</b>  | <b>1</b>   |
|          | Ian W.N. Jones and Thomas E. Levy  |            |
| <b>2</b> | <b>3D Recording in the Field: Style Without Substance? . . . . .</b>   | <b>19</b>  |
|          | Matthew D. Howland   |            |
| <b>3</b> | <b>Integrating Micro- and Macro-Archaeology at a<br/>Multi-period Site: Insights and Outcomes from Tell es-Safi/Gath . . .</b>                       | <b>35</b>  |
|          | Aren M. Maeir  |            |
| <b>4</b> | <b>Using Tools in Ways in Which They Were Not Intended:<br/>A Test Case of the Use of PlanGrid for<br/>Field Registration at Tel Burna . . . . .</b> | <b>51</b>  |
|          | Chris McKinny and Itzhaq Shai  |            |
| <b>5</b> | <b>From Multispectral 3D Recording and Documentation<br/>to Development of Mobile Apps for Dissemination<br/>of Cultural Heritage . . . . .</b>      | <b>67</b>  |
|          | Miriam Cabrelles, Silvia Blanco-Pons, Berta Carrión-Ruiz,<br>and José Luis Lerma   |            |
| <b>6</b> | <b>Toward a Grand Narrative of Bronze Age Vegetation Change<br/>and Social Dynamics in the Southern Levant. . . . .</b>                              | <b>91</b>  |
|          | Patricia L. Fall, Mariela Soto-Berelev, Elizabeth Ridder,<br>and Steven E. Falconer  |            |
| <b>7</b> | <b>The Challenge of Digitized Survey Data. . . . .</b>   | <b>111</b> |
|          | Moti Haiman  |            |

**8 The West Bank and East Jerusalem Archaeological Database:  
Narratives of Archaeology and Archaeological Practices . . . . . 123**  
Adi Keinan-Schoonbaert

**9 At-Risk World Heritage, Cyber, and Marine Archaeology:  
The Kastrouli–Antikyra Bay Land and Sea Project,  
Phokis, Greece . . . . . 143**  
Thomas E. Levy, T. Sideris, M. Howland, B. Liss, G. Tsokas,  
A. Stambolidis, E. Fikos, G. Vargemezis, P. Tsourlos,  
A. Georgopoulos, G. Papatheodorou, M. Garaga,  
D. Christodoulou, R. Norris, I. Rivera-Collazo, and I. Liritzis

**Index . . . . . 235**

# Contributors

**Silvia Blanco-Pons** Department of Cartographic Engineering, Geodesy and Photogrammetry Photogrammetry & Laser Scanning Research Group (GIFLE), Universitat Politècnica de València, Valencia, Spain

**Miriam Cabrelles** Department of Cartographic Engineering, Geodesy and Photogrammetry, Photogrammetry & Laser Scanning Research Group (GIFLE), Universitat Politècnica de València, Valencia, Spain

**Berta Carrión-Ruiz** Department of Cartographic Engineering, Geodesy and Photogrammetry Photogrammetry & Laser Scanning Research Group (GIFLE), Universitat Politècnica de València, Valencia, Spain

**D. Christodoulou** University of Patras, Department of Geology, Lab of Marine Geology and Physical Oceanography, Patras, Greece

**Steven E. Falconer** Department of Anthropology, University of North Carolina Charlotte, Charlotte, NC, USA

**Patricia L. Fall** Department of Geography & Earth Sciences, University of North Carolina Charlotte, Charlotte, NC, USA

**E. Fikos** Aristotle University of Thessaloniki, Exploration Geophysics Lab, School of Geology, Thessaloniki, Greece

**M. Garaga** University of Patras, Department of Geology, Lab of Marine Geology and Physical Oceanography, Patras, Greece

**A. Georgopoulos** National Technical University of Athens, Laboratory of Photogrammetry, School of Rural & Surveying Engineering, Athens, Greece

**Moti Haiman** Israel Antiquities Authority, Jerusalem, Israel

**M. Howland** University of California, San Diego, Department of Anthropology, Center for Cyber-Archaeology and Sustainability, Scripps Center for Marine Archaeology, La Jolla, CA, USA

**Matthew D. Howland** University of California, San Diego, CA, USA

**Ian W.N. Jones** Department of Anthropology, Center for Cyber-Archaeology and Sustainability, University of California, San Diego, CA, USA

**Adi Keinan-Schoonbaert** University College London, London, UK

**José Luis Lerma** Department of Cartographic Engineering, Geodesy and Photogrammetry Photogrammetry & Laser Scanning Research Group (GIFLE), Universitat Politècnica de València, Valencia, Spain

**Thomas E. Levy** Department of Anthropology, Center for Cyber-Archaeology and Sustainability, University of California, San Diego, CA, USA

**B. Liss** University of California, San Diego, Department of Anthropology, Center for Cyber-Archaeology and Sustainability, Scripps Center for Marine Archaeology, La Jolla, CA, USA

**I. Liritzis** University of the Aegean, Department of Mediterranean Studies, Lab of Archaeometry and Lab of Environmental Archaeology, Rhodes, Greece

**Aren M. Maeir** The Tell es-Safi/Gath Archaeological Project, Bar-Ilan University, Ramat-Gan, Israel

**Chris McKinny** Texas A&M University Corpus Christi, Corpus Christi, Texas, United States

**R. Norris** University of California, San Diego; Scripps Center for Marine Archaeology, Scripps Institution of Oceanography, La Jolla, CA, USA

**G. Papatheodorou** University of Patras, Department of Geology, Lab of Marine Geology and Physical Oceanography, Patras, Greece

**Elizabeth Ridder** Department of Liberal Studies, California State University San Marcos, San Marcos, CA, USA

**I. Rivera-Collazo** University of California, San Diego, Department of Anthropology, Center for Cyber-Archaeology and Sustainability, Scripps Center for Marine Archaeology, La Jolla, CA, USA

**Itzhaq Shai** Israel Heritage Department, Ariel University, Ariel, Israel

**T. Sideris** University of the Aegean, Department of Mediterranean Studies, Lab of Archaeometry and Lab of Environmental Archaeology, Rhodes, Greece

**A. Stambolidis** Aristotle University of Thessaloniki, Exploration Geophysics Lab, School of Geology, Thessaloniki, Greece

**Mariela Soto-Berelov** School of Mathematical and Geospatial Sciences, RMIT University, Melbourne, VIC, Australia

**G. Tsokas** Aristotle University of Thessaloniki, Exploration Geophysics Lab,  
School of Geology, Thessaloniki, Greece

**P. Tsourlos** Aristotle University of Thessaloniki, Exploration Geophysics Lab,  
School of Geology, Thessaloniki, Greece

**G. Vargemezis** Aristotle University of Thessaloniki, Exploration Geophysics Lab,  
School of Geology, Thessaloniki, Greece

# About the Editors

**Thomas E. Levy** is a distinguished professor and holds the Norma Kershaw Chair in the Archaeology of Ancient Israel and Neighboring Lands at the University of California, San Diego. He is a member of the Department of Anthropology and Judaic Studies Program and leads the cyber-archaeology research group at the Qualcomm Institute, California Institute for Telecommunications and Information Technology (Calit2).

**Ian W.N. Jones** is a Ph.D. candidate in the Department of Anthropology at the University of California, San Diego. His research focuses primarily on copper production during the Islamic period in southern Jordan and the economy of the southern Levant in the early 2nd millennium CE. As part of his work with UCSD's Center for Interdisciplinary Science in Art, Architecture, and Archaeology (CISA3), he is also interested in the integration of spatial technologies such as GIS and satellite remote sensing with traditional archaeological field methods for investigating processes of settlement and landscape change.

# Chapter 9

## At-Risk World Heritage, Cyber, and Marine Archaeology: The Kastrouli–Antikyra Bay Land and Sea Project, Phokis, Greece

Thomas E. Levy, T. Sideris, M. Howland, B. Liss, G. Tsokas, A. Stambolidis, E. Fikos, G. Vargemezis, P. Tsourlos, A. Georgopoulos, G. Papatheodorou, M. Garaga, D. Christodoulou, R. Norris, I. Rivera-Collazo, and I. Liritzis

### Introduction to the Land and Sea Project

The Kastrouli–Antikyra Bay Land and Sea Project near Greece’s Gulf of Corinth was inspired by a number of interwoven research goals including: (a) applying a range of cyber-archaeology and geophysical tools to address the issue of at-risk cultural heritage in the eastern Mediterranean; (b) using this study to help develop a marine archaeology methodology suitable for studying human coastal adaptation during the late Holocene across time and space; (c) focusing on the end of the Late Bronze Age in the eastern Mediterranean to address the problem of the collapse of Mycenaean, Hittite, and New Kingdom Egypt civilizations to investigate the role that

---

T.E. Levy (✉) • M. Howland • B. Liss • I. Rivera-Collazo  
University of California, San Diego, Department of Anthropology, Center for Cyber-Archaeology and Sustainability, Scripps Center for Marine Archaeology, La Jolla, CA, USA  
e-mail: [tlevy@ucsd.edu](mailto:tlevy@ucsd.edu)

T. Sideris • I. Liritzis  
University of the Aegean, Department of Mediterranean Studies, Lab of Archaeometry and Lab of Environmental Archaeology, Rhodes, Greece

G. Tsokas • A. Stambolidis • E. Fikos • G. Vargemezis • P. Tsourlos  
Aristotle University of Thessaloniki, Exploration Geophysics Lab, School of Geology, Thessaloniki, Greece

A. Georgopoulos  
National Technical University of Athens, Laboratory of Photogrammetry, School of Rural & Surveying Engineering, Athens, Greece

G. Papatheodorou • M. Garaga • D. Christodoulou  
University of Patras, Department of Geology, Lab of Marine Geology and Physical Oceanography, Patras, Greece

R. Norris  
University of California, San Diego; Scripps Center for Marine Archaeology, Scripps Institution of Oceanography, La Jolla, CA, USA

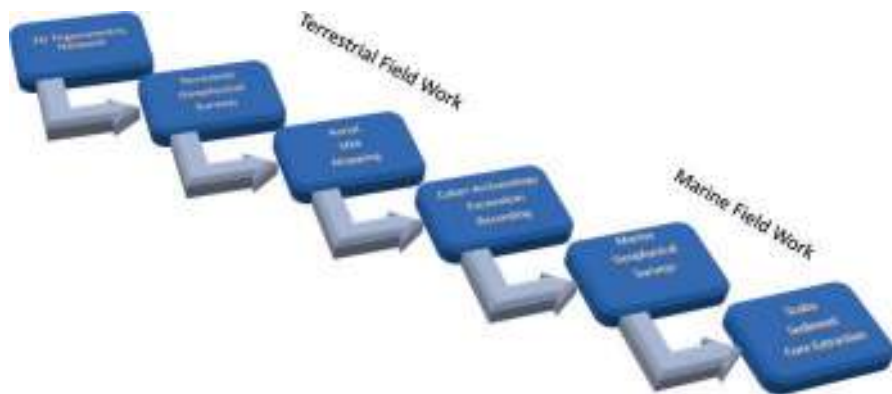


**Fig. 9.1** The transdisciplinary workflow for the 2016 Kastrouli–Antikyra Bay, Greece, Land and Sea Project

climate, environmental, and social factors may have played in this process; and (d) finally to engage in the more local problem of understanding the nature of Mycenaean coastal worlds.

This integrated approach takes a transdisciplinary approach to research opening new understandings of issues concerning climate change, human adaptation, and culture change in sensitive coastal environments. The workflow for the 2016 land and sea expedition is shown in Fig. 9.1.

In the study presented here, we focus on describing the workflow and methods used in the Kastrouli–Antikyra Bay Project, which integrates recent developments in terrestrial cyber-archaeology (Levy 2013) and marine archaeology with the aim of developing a more effective field methodology for studying human adaptation to coastal environments during the Holocene around the world. As the focus of our research is on the archaeology of the eastern Mediterranean, issues concerning connectivity between societies and local cultural evolution from the Aegean region to the southern Levant are of great interest. A number of pan-eastern Mediterranean problems are of interest to the Kastrouli–Antikyra Bay project (Figs. 9.2 and 9.3): 1) the collapse of Late Bronze Age (LBA) civilizations ca. 1200–1100 BCE that brought the end of palatial culture of Mycenaean Greece, the Hittite Empire, and the Egyptian New Kingdom (Cline 2014); the nature of climate change during the Late Bronze–Iron Age based on proxy paleoenvironmental data including pollen, marine resources, geomorphology, and other datasets (Cramer et al. 2017; Langgut et al. 2013, 2014); and how the power vacuum that resulted from the LBA collapse opened up new economic, ideological, and trade opportunities for small-scale societies in the region such as the Israelites, Edomites, Sea Peoples, and others to evolve (cf. Ben-Shlomo et al. 2008; Killebrew 2005; Levy et al. 2014; Lipschitz and Maier 2017). As suggested by Weiner (n.d.), some of the responses to climate and environmental deterioration at the end of the Late Bronze Age included famine, pandemics, and warfare.



**Fig. 9.2** Map of Gulf of Corinth region and location of Kastrouli in relation to major sites and towns on the mainland of Greece (Map by M. Howland, Center for Cyber-Archaeology and Sustainability, UC San Diego)

On the local scale, the Kastrouli–Antikyra Project aims to investigate what Thomas Tartaron (2013:7–11) defines as Mycenaean coast worlds, in particular at the end of the Late Bronze Age or Late Helladic (LH) period, which coincides the period leading up to and after the LBA collapse. There are no sharp chronological boundaries with archaeological periods. The LH begins ca. 1600 BCE and ends ca. 1050 BCE when it reached an apex, or *koine*, in the high palatial period of LH IIIA2 to early LH IIIB (ca. 1370 – 1250 BCE) with a “complex sociopolitical system based on the palaces and recorded using a syllabic script (Linear B) that represents an archaic form of the Greek language, and sometimes even an ethnicity...” (2013:7). Scholars debate whether there was a sharp end to the Mycenaean period. However, as Marina Thomatos (2006) points out, there was a kind of revival in LH IIIC of the Mycenaean culture. For the purposes of this paper, the end of the LH IIIC is 1190–1070 BCE (Tartaron 2013:3). It seems everything is debated in Mycenaean archaeology, including the notion of a “core area” of settlement. For this study, we assume that the Peloponnese and central Greece, which include Kastrouli and the Gulf of Corinth, are indeed part of the Mycenaean core area of settlement making this project a significant data source for examining the LBA issues noted above. The Kastrouli and Antikyra Bay coastlines were and still are tightly linked as a locus for economic and social intercourse making them an ideal setting for investigating a Mycenaean coastal world.



**Fig. 9.3** Map of the area of Kastrouli. Red dots represent Mycenaean sites (After A. Sideris 2014:17; map by M. Howland)

## Terrestrial Excavation at Kastrouli

Kastrouli (E375419.559, N4250792.352), a small fortified site in the Phokis region of central Greece (near the modern village of Desfina), was the focus of excavations in the summer of 2016 (July 20–August 3; Fig. 9.2) in the context of an at-risk cultural heritage site. An ancient fortification wall encompassing an area of 1.67 ha defines the size of the site where both archaeological features and ceramic sherds are found in abundance. The project aimed to fully and systematically excavate the exposed tomb on the site's surface and to section its fortification wall. The site was previously excavated in 2005, but this short project (lasting several days) performed little systematic excavation (primarily cleaning) to evaluate the condition of tombs at the site that were previously looted as evidenced by their disturbed nature (Raptopoulos 2012: 1074). Based on the brief excavations, the tomb was

determined from the architecture to be a small Mycenaean Tholos tomb and was dated to the Late Helladic IIIB2 based on the ceramic typology. These were the only excavations at the site to date. The 2016 excavation season was directed by Thomas E. Levy (PI, University of California, San Diego), Athanasios Sideris (Excavation Director, University of the Aegean), and Ioannis Liritzis (Co-PI, University of the Aegean). Graduate students Matthew D. Howland and Brady Liss (University of California, San Diego) functioned as field supervisors, and a team of undergraduate students from the University of California, San Diego, were the primary excavators along with three local workers. In addition, three computer programmers (Rose Smith, Carolyn Breeze, and Taylor Harman) developing the web-based *ArchaeoSTOR* artifact database joined the team to manage and organize all excavated artifacts. Before the excavation started, the site was georeferenced, mapped, and surveyed using an array of state-of-the-art photogrammetric and geophysical methods described below (Sideris et al. 2017).

## Transdisciplinary Methodologies

### *3D Network of Trigonometric Points for Georeferencing Archaeological Fieldwork*

To facilitate high spatial accuracy for all recorded finds, the 2016 excavation season at Kastrouli began by establishing reliable control points throughout the site. Andreas Georgopoulos and Panagiotis Agrafiotis (National Technical University of Athens) headed the project to create a network of nine control points (numbered T1-T9, see Fig. 9.4), which were referenced to the Greek (Hellenic) Geodetic Reference System (GGRS'87-ΕΓΣΑ'87; see below). The locations for control points were selected based on the need to avoid any perceivable interventions at the Kastrouli site and to ensure the permanence of their position not only during the measurements but also for the future needs of the work. The nine points were permanently marked with concrete pillars, 0.1 m diameter and 10–15 cm height, equipped with steel marks to enable centering of the instruments (total stations, GPS, etc.). The coordinates of these locations were collected using a Topcon GPT 3003 total station.

Unfortunately, the control points were not established before the first day of excavation. As such, recording of loci and artifact finds during the excavation were based on two control points established by GPS provided by Grigoris Tsokas (University of Thessaloniki) (Table 9.1). These points provided the base control points for the total station/*ArchField* recording for the entire excavation to maintain consistency. However, in checking the accuracy of the coordinates of the GPS control points from the established control points described above, it was discovered that the GPS points were inaccurate by roughly 22 centimeters in the southeast direction. To correct this error, test points were recorded both from the GPS control



**Fig. 9.4** The 3D trigonometric network at Kastrouli, Phokis, Greece. A total of nine points were established, each labeled with the letter “T” (Image: Courtesy A. Georgopoulos, Google Earth)

**Table 9.1** Table of GPS points provided by Grigoris Tsokas used for recording artifact and loci locations

| Kastrouli GPS point coordinates (m) |             |             |           |
|-------------------------------------|-------------|-------------|-----------|
| Point name                          | Easting     | Northing    | Elevation |
| d1                                  | 375364.1344 | 4250804.235 | 547.87001 |
| d2                                  | 375372.1963 | 4250809.271 | 548.24936 |

point and from T1 by total station. By having the same point recorded from both positions, all points and polygons recorded based on the GPS control point could subsequently be shifted in GIS based on the apparent difference. The accuracy of the points after correction became  $\pm 2$  cm, in line with the levels of accuracy obtained by total station survey across the site.

## Selection of Positions

In consultation with the excavation team, careful examination of the site surface was made that led to the decision to establish a network composed of nine points (Fig. 9.4) numbered T1, T2, ..., T9. These positions were selected in order to:

- Avoid any perceivable interventions at the archaeological site
- Ensure the permanence of their position not only during the measurements but also for the future needs of the work

## The Greek Geodetic Reference System

In accordance with Greek antiquities laws, it was required that the Kastrouli network be referenced to the Greek (Hellenic) Geodetic Reference System (GGRS'87–ΕΓΣΑ'87). The Greek Geodetic Reference System 1987 or GGRS87 (ΕΓΣΑ'87) is a geodetic system commonly used in Greece. The system specifies a local geodetic datum and a projection system. GGRS87 specifies a non-geocentric datum that is tied to the coordinates of the key geodetic station at the Dionysos Satellite Observatory (DSO) northeast of Athens (38.078400°N 23.932939°E). The central pedestal (CP) at this location has by definition GGRS87 coordinates 38° 4' 33.8000" N - 23° 55' 51.0000" E, N = +7 m. Although HGRS87 uses the GRS80 ellipsoid, the origin is shifted relative to the GRS80 geocenter, so that the ellipsoidal surface is best for Greece. The specified offsets relative to WGS84 are  $\Delta x = -199.87$  m,  $\Delta y = 74.79$  m, and  $\Delta z = 246.62$  m. The GGRS87 datum is implemented by a first-order geodetic network, which consists of approximately 30 triangulation stations throughout Greece and is maintained by the Hellenic Military Geographical Service. The initial uncertainty was estimated as 0.1 ppm. However, there are considerable tectonic movements that move parts of Greece toward different directions causing incompatibilities between surveys taking place at different times.

HGRS87 also specifies a transverse Mercator cartographic projection (TM) with  $m_0 = 0.9996$ , covering six degrees of longitude either side of 24 degrees east (18–30 degrees east). This way all Greek territory (stretching to approximately 9° of longitude) is projected in one zone. References are in meters. Northings are counted from the equator. A false easting of 500,000 m is assigned to the central meridian (24° east), so eastings are always positive.

## Accurate Geodetic Measurements

The established network at Kastrouli was connected and related to the Greek Geodetic Reference System '87 (GGRS '87) by using static GPS measurements. The elevation heights are orthometric and refer to the mean sea level. The nine points were permanently marked with concrete pillars, 0.1 m diameter and 10–15 cm



**Fig. 9.5** For geodetic measurements, a TopCon GPT 3003 total station was employed. For daily excavation recording, a Leica TS02 Reflectorless Total Station was used

height, equipped with steel marks to enable centering of the instruments (total stations, GPS, etc.). Global Navigation Satellite System (GNSS) and classic geodetic measurements were used for two reasons: firstly, to adjust the network in the Greek Reference System and, secondly, to make sure that this reference is done with minimum constraints, thus maintaining its internal accuracy.

The geodetic measurements for the network constituted of vertical and horizontal angles and slope distances between the various vertices. These measurements were performed using the Topcon GPT 3003 Total Station (Figs. 9.5 and 9.6), which ensures accuracy of  $\pm 3''$  (1 mgon) for the angle measurements and  $\pm (3 \text{ mm} + 2 \text{ ppm} \times D)$  (D: measuring distance (mm)) for the distances to a prism. For the GNSS measurements, a Spectra Precision receiver was used to perform static determination of selected points of the network.

For the geodetic measurements apart from the total station, the following ancillary equipment were used:

- Tripods for the total station and reflector setting
- Tribrachs for the reflector placement
- Reflector supporting bases
- Reflectors

**Fig. 9.6** Tribrach, supporting base and reflector (Image: Courtesy A. Georgopoulos)



**Table 9.2** The coordinates X, Y, the orthometric heights H, and their respective residuals for control points used at Kastrouli

| Point name | Point coordinates in EGSA '87 geodetic system (m) |         |         | Standard error $\sigma_o$ (m) |       |       |
|------------|---|---------|---------|-------------------------------|-------|-------|
|            | X   | Y       | H       | X                             | Y     | H     |
| T1         | 375359.215  | 4250817 | 547.578 | 0.002                         | 0.003 | 0.008 |
| T2         | 375385.464  | 4250846 | 548.052 | 0.003                         | 0.003 | 0.008 |
| T3         | 375400.279  | 4250816 | 549.36  | 0.004                         | 0.003 | 0.013 |
| T4         | 375443.318  | 4250774 | 547.775 | 0.002                         | 0.002 | 0.007 |
| T5         | 375449.559  | 4250839 | 547.394 | 0.003                         | 0.003 | 0.008 |
| T6         | 375467.651  | 4250738 | 544.375 | 0.003                         | 0.002 | 0.006 |
| T7         | 375443.609  | 4250706 | 542.125 | 0.003                         | 0.001 | 0.006 |
| T8         | 375389.142  | 4250718 | 542.08  | 0.002                         | 0.001 | 0.006 |
| T9         | 375351.359  | 4250756 | 543.048 | 0.002                         | 0.002 | 0.007 |

**Adjustment and Results**

The measurements were adjusted as a network and not a simple traverse, and the adjusted coordinates (Table 9.2) were referenced with the minimum constraints to GGRS'87 based on T1 and T9. The determination of the coordinates of the points was performed with an accuracy of 0.9mm. In Table 9.2, the coordinates X, Y and the orthometric heights H are presented. For archaeoastronomical purposes at the site, we use the following coordinates -

Latitude: 38.399° N (38 23' 58" N)  
 Longitude: 22.574° E (22 34' 28" E)

## Geophysical Investigations at Kastrouli: Introduction

A variety of geophysical methods (resistivity mapping, total field or differential magnetometry, electrical tomography, and ground-penetrating radar (GPR)) are usually employed to explore the subsurface with the aim of detecting and mapping concealed antiquities. However, the setting of each site dictates the particular methods to be employed. The decision of which methods to use is a collaborative one between the geophysicist responsible for the survey and the archaeologist who is in charge of the excavation. The most critical factor for the selection of suitable methods is the magnitude of the contrast in the physical properties between the targets and the hosting medium at the site.

As shown below, almost all the available geophysical methods were applied, a kind of “shotgun” approach (cf. Witten 2006) for the investigation of relatively small areas at the Mycenaean site of Kastrouli in Desfina in the region of continental Greece (central Greece). In fact, magnetic gradiometry, GPR, and electrical resistivity tomographies (ERTs) were carried out during the summer of 2016 (11, 12, 20, and 21 of August). Grids were established on the ground surface for carrying out the geophysical measurements which were referenced to the Hellenic Geodetic Reference System 1987 (ΕΓΣΑ 1987) described above. Processing and interpretation of the data took place in the installations of the Laboratory of Exploration Geophysics in Thessaloniki, immediately after the fieldwork. Below we present short descriptions of the principles of the methods used, followed by a discussion of the surveys, the data processing, and results.

## The Resistivity Tomography Method

### *General*

Resistivity techniques are well-established and widely used to solve a variety of geotechnical, geological, and environmental subsurface detection problems (Ward 1990) (i.e., foundation and integrity of dams, cavity detection, planning of infrastructure, assessing the hydraulic and anisotropical properties of the subsurface, location of man-made structures, etc.).

The goal of the resistivity method is to measure the potential differences on the surface due to the current flow within the ground. The measured drop of potential reflects the difficulty with which the electrical current can be made to flow through the earth, giving an indication of the earth’s electrical resistivity, which is directly dependent on the way the current is being conducted within the earth. Since current conduction is related to the composition and the groundwater of the subsurface, a knowledge of resistivity can be the basis for distinguishing existing earth features (layering, voids, man-made structures, etc.).

Since the factors deciding the electrical current conduction into the soil (porosity, water distribution, chemical composition, etc.) are quite variable, it is often

observed that similar formations at different sites can appear to have entirely different variations in resistivity. This fact renders resistivity as a property quite unstable and hence sometimes inadequate for extracting exact lithological conclusions for the subsurface. Therefore, it should be kept in mind while interpreting resistivity data that the measured resistivity values are not absolute but relative, and therefore only relative conclusions about the area's lithology can be made.

For instance, by observing the data, it can be said that there is a formation which is less resistive than the surrounding formations, but it will not be safe to determine its identity just by its resistivity value. Erroneous interpretations can be made when this fact is not taken into account. Conversely, this resistivity disadvantage (which is common in every geophysical technique) does not prohibit successful interpretations, but in order to achieve good results, prior information concerning the studied area should be considered. This prior information could include geological maps of the area, results from possible drilling and excavation, or in general any kind of information that could enhance the knowledge of what is possible to be found beneath the soil. This information is used to calibrate the interpretation and should be collected before the measuring procedure to allow the optimum resistivity array and survey strategy to be chosen.

### ***Resistivity Tomography***

In the resistivity technique, two current electrodes (a source and a sink) are inserted into the ground, and at the same time two different probes are used to measure the drop of electrical potential; thus, every measurement involves four electrodes in total. The depth that each measurement can “view” into the ground can be controlled by adjusting the electrode separation: the penetration depth increases as the distance between the electrodes gets bigger. Based on these principles, it is possible to obtain a series of measurement profiles with increased electrode spacing in order to get an indication of the earth resistivity variation of the studied area in both lateral and vertical directions. As in any geophysical technique, these measurements (called apparent resistivity measurements) do not provide a direct “image” of the subsurface but simply constitute the integrated effect of the subsurface property which could be (in cases of complex subsurface property distribution) far away from reality.

Traditionally the interpretation of these measured datasets is being made by the use of the pseudosection method (Edwards 1977; Griffiths et al. 1990). It is based on the fact that the larger the electrode separation, the more the measured apparent resistivity is related to greater depths. Hence, each measured resistivity value is arbitrarily placed under the center of the particular four-electrode arrangement at a depth proportional to the overall electrode separation. By doing this for every measurement, a trapezoidal pseudo-image of the subsurface can be obtained. Various arrays (e.g., dipole–dipole, Wenner, pole–dipole) can be used for the production of pseudosections. The term ERT includes the traditional geoelectrical method but can be considered more general as it also involves measurements obtained with no

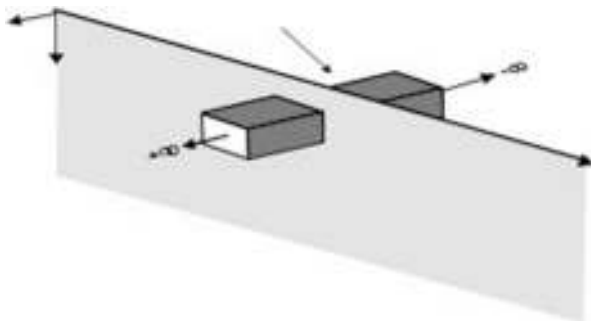


**Fig. 9.7** Geoelectrical parameter of three dimensions. A section of the block is considered as 2D parameter (After Tsourlos 1995)

conventional arrays, while electrodes can be also positioned into boreholes (Shima 1990). Interpretation of the pseudosection images involves a great amount of “expertise,” and yet for cases of complex resistivity, accurate interpretation is not possible. The advent of fast computers allowed the development of fully automated algorithms known as inversion algorithms which can produce “accurate” subsurface resistivity images. The term “inversion” in the resistivity method describes the (usually fully computerized) procedure of constructing an image of the “real” subsurface’s resistivity distribution given the respective observed datasets. Such algorithms are mathematically complicated and allow the processing of any measured dataset independent of the electrode arrangement. Furthermore the advent of resistivity measuring instruments allowed the automation of the measuring procedure, and in that sense any type of measurements (even cross borehole) can be obtained easily.

The combination of the automated measuring systems with the new interpretation (inversion) schemes is described with the term resistivity tomography: the term is due to the similarities of the procedure to medical imaging techniques (X-ray tomography).

The techniques aiming to solve the inverse geoelectric problem use either approximation methods (e.g., Method of Zhody–Barker; Barker 1992; Tsourlos et al. 1993) or employment of fully nonlinear inversion schemes (e.g., Tripp et al. 1984; Shima 1990; Tsourlos et al. 1995).

During the 2D resistivity inversion procedure, the subsurface is considered as a set of individual blocks (parameters) that are allowed to vary their resistivity independently (Fig. 9.7). The aim is to calculate a subsurface resistivity estimate  $x$  for which the difference  $dy$  between the observed data  $d_{obs}$  and the modeled data  $d_{calc}$  (calculated using the forward modeling technique) is minimized.

Since we are dealing with a nonlinear problem, this procedure has to be iterative: in every iteration an improved resistivity estimate is sought, and eventually the procedure stops until certain convergence criteria are met (i.e., until the RMS error is practically stable).

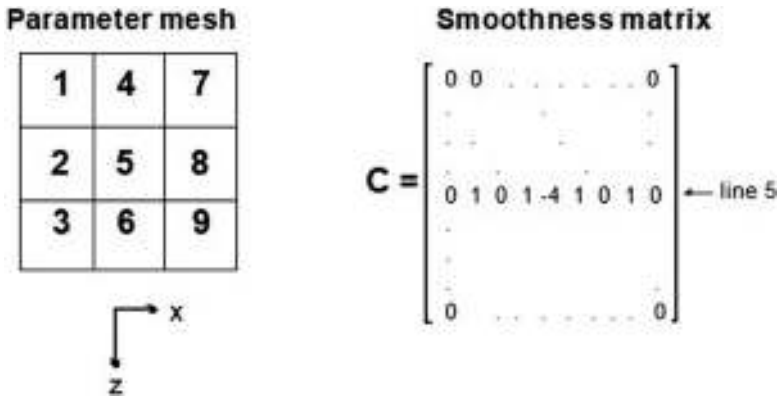


**Fig. 9.8** Formation of the smoothness matrix for the case of nine parameters (After Tsourlos 1995)

Assuming a 2D case, a nonlinear smoothness-constrained inversion algorithm was used (Tsourlos 1995). The inversion is iterative, and the resistivity  $\mathbf{x}_{k+1}$  at the  $k+1$ th iteration is given by:

$$\mathbf{x}_{k+1} = \mathbf{x}_k + \mathbf{dx}_k = \mathbf{x}_k + [(\mathbf{J}_k^T \mathbf{J}_k + \mu\kappa (\mathbf{C}_x^T \mathbf{C}_x + \mathbf{C}_z^T \mathbf{C}_z))]^{-1} \mathbf{J}_k^T \mathbf{dy}_k \quad (9.1)$$

where  $\mathbf{C}_x$  and  $\mathbf{C}_z$  are matrices which describe the smoothness pattern (Fig. 9.8) of the model in the  $x$  and  $z$  axes, respectively (Degroot-Hedlin and Constable 1990),  $\mathbf{dy}_k$  is the vector of differences between the observed data  $\mathbf{dobs}$  and the modeled data  $\mathbf{dkcalc}$  (calculated using the forward modeling technique), and  $\mathbf{J}_k$  and  $\mu\kappa$  are the Jacobian matrix estimate and the Lagrangian multiplier, respectively, for the  $k$ th iteration.

A proven 2.5D finite element method (FEM) scheme is used as the platform for the forward resistivity calculations (Tsourlos et al. 1999). In 2.5D modeling the resistivity is allowed to vary only in two dimensions, but the sources are 3D which allows us to obtain values, which are realistic. The adjoint equation approach was incorporated into the FEM scheme in order to calculate the Jacobian matrix  $\mathbf{J}$  (Tsourlos 1995). A flowchart of the algorithm is shown in Fig. 9.9.

### *Short Description of the Magnetic Prospecting Method*

The magnetic prospecting method aims to detect variations of subsurface magnetization that reflect the presence of subsurface inhomogeneities. It is consisted in measuring the spatial distribution of the total magnetic field on the Earth’s surface. Small changes of this field (anomalies) are caused by the subsurface variation of

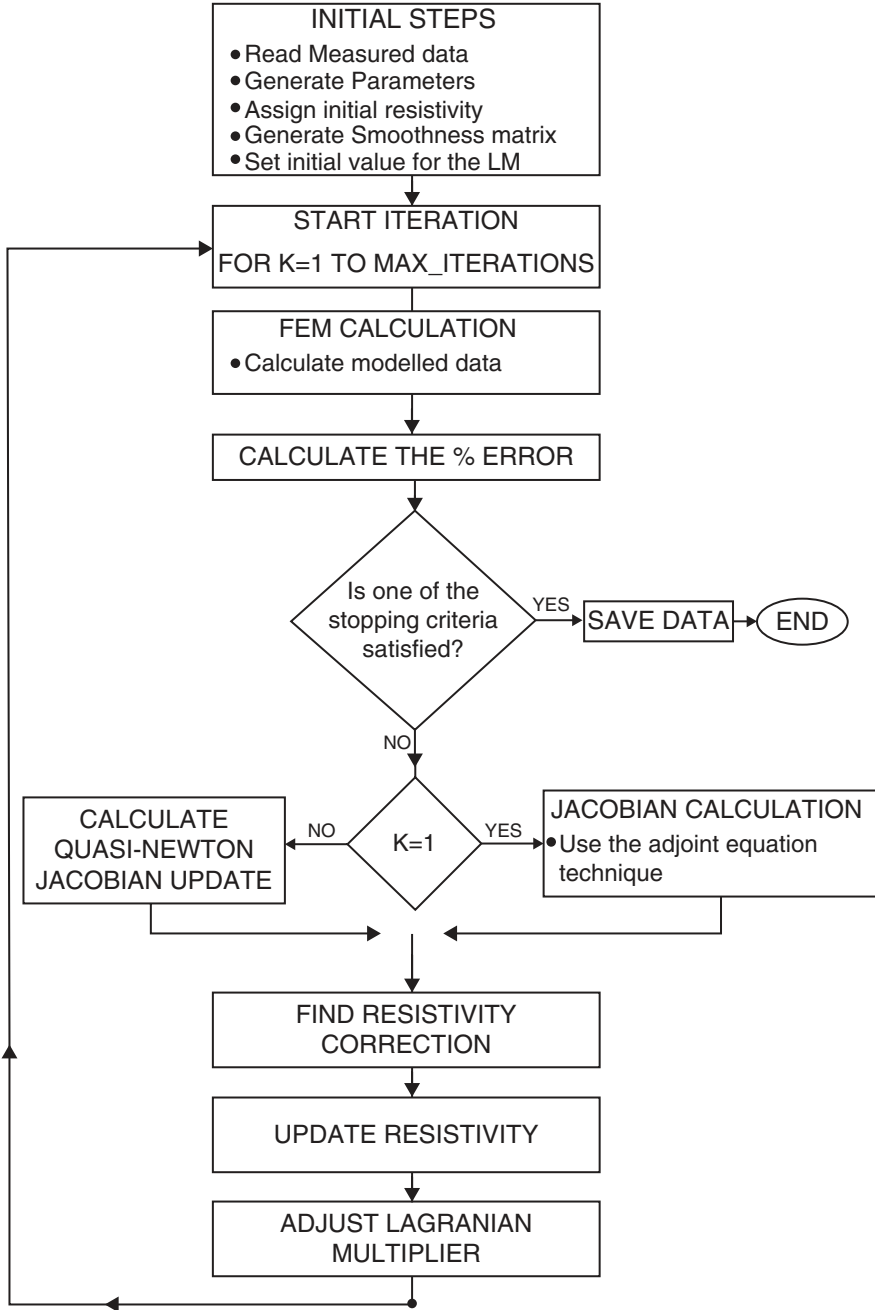


Fig. 9.9 A simplified flowchart of the algorithm (After Tsourlos 1995)

magnetization. Therefore, the location of the anomalies leads to the detection of the subsurface targets. The characteristics of the anomaly can be then analyzed and yield quantified parameters of the targets, such as its dimensions, its burial depth and susceptibility contrast with respect to the hosting medium. The method has been used successfully to study concealed natural and man-made structures. Its use in archaeology was introduced in the decade of 1950 (Aitken 1974). Suppose that we have a buried structure who poses a susceptibility contrast  $\Delta\kappa$  with respect to the medium where it is hosted. If the Earth's magnetic field has a strength  $H$  at that particular location, then it creates induced magnetization in the structure having the magnitude of:

$$M = \Delta\kappa XH.$$

Consequently, a new field is produced whose intensity is  $H'$  and it is added locally to the inducing Earth's field. The vector addition of these two fields is called magnetic induction, and this parameter is recorded by the geophysical instruments. The magnitude of the induced magnetization and therefore the magnitude of the induced field are generally small with respect to the Earth's field. This is because most of the rocks found on Earth are paramagnetic (Parasnis 1997).

In case of prospecting for buried antiquities, the structures concealed in the subsurface are generally of small dimensions, usually having one or two orders of magnitude difference in their magnetic susceptibility with respect to the surrounding environment. Therefore, they create anomalies of small wavelength and usually of small amplitude in comparison to other applications of magnetic prospecting (e.g., mineral exploration). Consequently, dense spatial sampling of the total magnetic field (magnetic induction) is necessary to record the anomalies created by buried remnants of the past human activity.

Subsurface areas of increased magnetization will cause positive anomalies, while those of decreased magnetization will cause negative. Generally, buried ancient ditches, ruins of kilns, ruins of walls made by bricks, destruction phases, buried collapsed tiled roofs, etc. are expected to show positive anomalies. On the other hand, ruins of walls, whether made by hewn or raw stones, will show either negative or positive anomalies depending on the magnetic properties of the rock from which they were extracted. Limestone shows usually negligible magnetic susceptibility. On the contrary, the soils appear magnetized if the site was occupied by human activity in the past (Aitken 1974). Further, the soils that have been exposed to heating show also enhanced magnetic susceptibility (Le Borge 1955; Tite and Mullins 1971; Aitken 1974). Heating is most likely to have occurred in cultivated fields due to the practice of burning vegetation to clear the land. However, modern views (Linford 2006; Fassbinder 2015) on the mechanisms responsible for the enhancement of magnetic susceptibility of the topsoil and the lands occupied by humans indicate that the processes forming maghemite and magnetite are different and more complex than described in the early studies mentioned above.



**Fig. 9.10** The gradiometer used for the Kastrouli geophysical survey described here

### ***Magnetic Gradiometry***

If two magnetic sensors are used to record the Earth's field at two different height levels, their difference is an approximation of the vertical gradient of the field (Parasnis 1997). In strict physics terms, it is an approximation of the first vertical difference, and divided by the height, difference yields the approximation of the gradient. This mode of measuring the Earth's field is operationally advantageous since no correction is needed for the diurnal variation of the Earth's field. This is why it has become very popular in archaeological prospection where large numbers of measurements are necessary to sample densely the spatial variation of the field.

For the Kastrouli study, the FM256 *Fluxgate* gradiometer from *Geoscan Research* was used. This is shown in Fig. 9.10. More precisely, the particular instrument measures the first vertical difference of the vertical component of the magnetic field.

### ***Ground-Penetrating Radar (GPR)***

Ground-penetrating radar (GPR) is the general term applied to techniques which employ radio waves, typically in the frequency range from 1 to 2000 MHz, for mapping features buried in the ground or beneath floors and inside walls.

The operating principle (Annan 1992) is that an electromagnetic pulse (energy) is emitted by an antenna called transmitter. This pulse travels into the subsurface and is partly reflected when it encounters media with different electrical properties

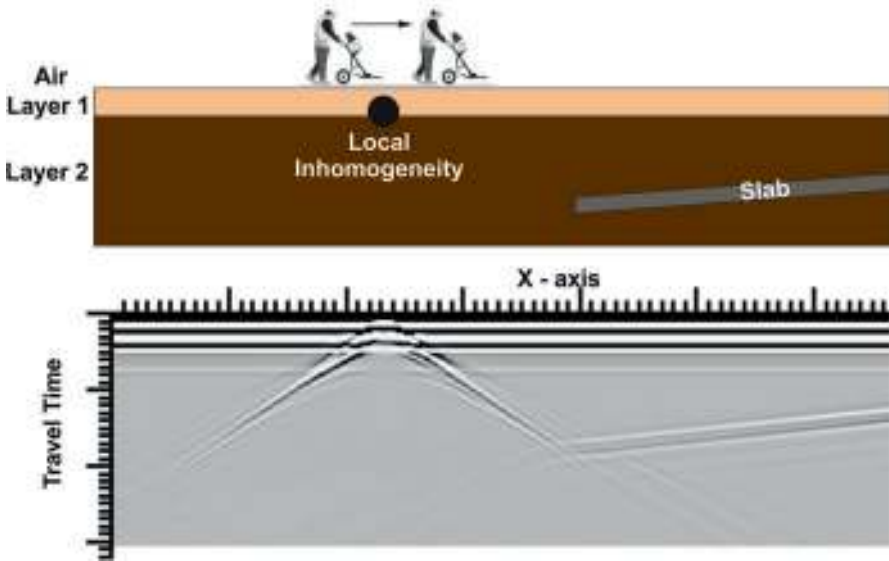


**Fig. 9.11** Schematic view of a reflection mode GPR survey. A GPR unit is moved along a survey line (*top*) acquiring responses at regular intervals and creating a cross-sectional image of the subsurface (*bottom*)

and partly propagated into deeper layers. The reflected energy is recorded by an antenna called receiver, which is either in a separate antenna box or in the same antenna box as the transmitter. The GPR unit measures how long it takes for a reflected signal to return to the receiving antenna as well as its strength. Hence, measuring this time interval and estimating the velocity of pulse propagation in the subsurface, it is possible to determine the location of underground reflectors.

As the GPR antennas are moved on the ground surface, a two-dimensional (2D) radargram is built up by time-domain traces when collecting data in the field, in real time (Fig. 9.11). This is the typical way of GPR data display. The horizontal axis of the cross-sectional view is the horizontal distance along the survey line, while the vertical axis is the two-way travel time of signals. If the electromagnetic velocity of pulse propagation in the subsurface is known, the time scale can be converted in a depth scale.

After data acquisition, a number of processing techniques are applied to GPR datasets in order to produce a clearer image for data interpretation and evaluation. When GPR data have been collected in a grid, along parallel profiles, one closely next to the other, it is possible to produce three-dimensional (3D) images and/or depth slices (i.e., horizontal sections of the subsurface along the depth axis). Seeing these images, it is straightforward to determine the location, depth, form, and size of subsurface anomalies (Goodman et al. 1995; Goodman and Piro 2013). The depth of penetration of GPR is mainly controlled by the dielectric properties of the ground. The limiting factor for the application of GPR is the presence of materials

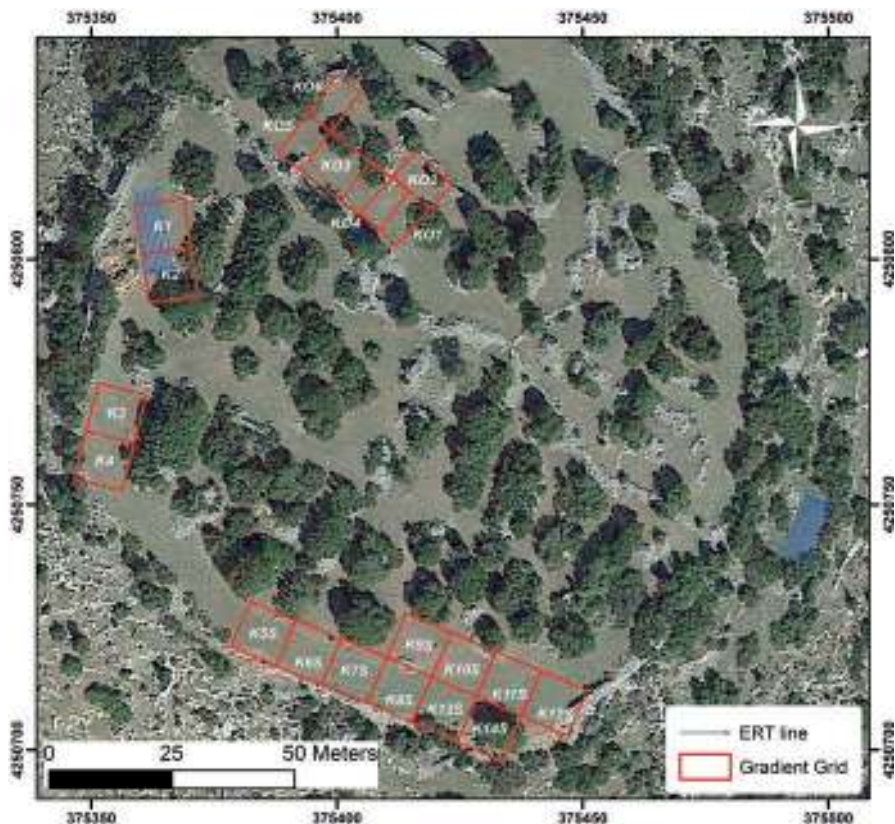


**Fig. 9.12** Layout of the cells (red color) established on the ground surface for the needs of the magnetic gradiometry and the GPR survey. The blue lines mark the tomographic transects (A Google Earth satellite image is used as background)

with high electrical conductivity at the area of prospection. In a highly conductive environment (e.g., clays, saline soils), electromagnetic waves attenuate rapidly, which results in poor penetration. Moreover, the GPR pulse depth of penetration and its resolution (i.e., the smallest object that can be detected) are dependent on the transmitting antenna central frequency. A high antenna frequency gives shallower depth of signal penetration but better resolution. On the other hand, a lower frequency antenna provides poorer resolution but deeper penetration.

## Survey Layout

Several meshes of grids (square cells) were established on the ground surface as shown in Fig. 9.12 to cope with the rather uneven topography. The cells denoted by red color were used for the magnetic gradiometry and the GPR survey, whereas the

ERTs carried out are depicted by blue lines. The resistivity tomography method was preferred wherever we were investigating for underground tombs, and thus the burial depth was expected to be big. On the other hand, wherever we were trying to image the buried remnants of walls, the classical magnetic gradiometry mapping method was used. The ground-penetrating radar (GPR) was also tested by carrying out parallel profiles in the cells K1 and K7S.

The ERT method was not extensively used during the first phase of the geophysical investigations which is reported in these pages. This is because ERT requires considerably more effort to set up. Thus, it was decided that it is better to use our resources to cover as large area as possible in order to get an idea of the urban complex inside the ancient walls. The survey was carried out during the highly dry period of the year, and thus the soil condition was rather optimum for the GPR survey. On the other hand, the dryness of the topsoil created some problems at the ERT survey since high contact resistances were encountered, and they had to be lowered by pouring water at the electrodes. Thus, good electrical coupling with the ground was established. It is clear that more than one method was applied in some cells. The subsurface of the cells K1 and K2 was explored with all the methods employed (gradiometry, GPR, and ERT). Also, both magnetic and GPR methods were used for the cell K7S.

### *The Resistivity Tomography Survey*

The resistivity tomography survey at Kastrouli aimed to image the subsurface at two particular portions of the site in both 2D and 3D contexts. The area eastward of the already excavated tombs and that in the so-called eastern circle was investigated. The first area is referred to as the “western tomb area” and includes Tomb A. The layout of the profiles along which the ERTs were performed is shown in Fig. 9.12. In fact, eight two-dimensional tomography surveys were carried out in the western tomb area and ten in the eastern circle on the other side of the site.

The dipole–dipole array (Parasnis 1997) was used in both cases because it is very sensitive to lateral inhomogeneities of resistivity (Ward 1990). Since relatively shallow depths were investigated and antique structures were expected to be buried in the particular locations, the resistivity should vary laterally in an intense manner. The inter-probe spacing, as well as the separation between the traverses, was set accordingly for each case. The SYSCAL pro resistivity meter of IRIS instruments was used. The instrument is equipped with an automated switch and supported by custom built connectors. The instrument is capable of maximum ten simultaneously receiving channels. The multicore cables used are custom built by the Laboratory of Exploration Geophysics of the Aristotle University of Thessaloniki. Figures 9.13 and 9.14 show components of the instrumentation used for the resistivity tomography survey at Kastrouli and several tomographic transects established on the ground surface.

Each individual tomography section was inverted using the algorithm of Tsourlos (1995). This procedure resulted into 2D images. However, the set of the tomographic



**Fig. 9.13** Parts of the instrumentation used and members of the field crew at the “eastern circle”

data of each sector were subjected to 3D inversion according to the scheme published by Tsourlos and Ogilvy (1999). Although the data acquisition cannot be considered as full 3D in our case, Papadopoulos et al. (2006) have proved that negligible imaging detail is lost provided that the inversion is performed by a full 3D algorithms. Also, the data have to be collected along dense parallel traverses, which should be ideally spaced at intervals equal to the spacing of the electrodes along the traverse. Both these constraints are fulfilled in our case.

The 3D inversion scheme performs an iterative optimization based on a 3D finite element modeling scheme. The algorithm is fully automated and self-correcting and performs smoothness-constrained inversion (Constable et al. 1987). The inversion procedure is accelerated by the use of a quasi-Newton technique for updating the Jacobian matrix. All inversions produced a low RMS error (less than 3%), indicative of the high data quality and of the high credibility of the results. The inversion results shown in the following pages of this report effectively depict the “real” sub-surface resistivity.



**Fig. 9.14** The blue lines show the tomographies conducted in July 2016 at the location having the conventional name “western tomb area.” The sketch is referenced to the Hellenic Geodetic System (ΕΓΣΑ 1987). A Google Earth satellite image is used as background

### *Western Tomb Area*

Eight (8) parallel tomographies were carried out in area where the Mycenaean tombs had been disturbed in the past (Tomb A and associated features). The layout is seen in Figs. 9.12, 9.14, and 9.15. The inter-probe spacing was set to 0.75 m ( $a = 0.75$  m), while 24 channels were used. Thus, the length of each tomography was 17.25 m. The maximum dipole separation was set to  $n = 8$ . The length of the measuring dipole was then doubled ( $2a$ ), and  $n_{max}$  was set to 6. Similarly, the length of the dipole increased up to  $5a$  (3.75 m). The tomographies were established 0.75 m apart each from the other.



**Fig. 9.15** Another view of the layout of the tomographies at the “western tomb area.” The sketch is referenced to the Hellenic Geodetic System (ΕΓΣΑ 1987). A Google Earth satellite image is used as background

### *Eastern Circle*

Situated on the eastern edge of the Kastrovli village site, the circular feature selected for detailed geophysical investigation could be another Mycenaean mortuary feature. Ten (10) parallel tomographies were carried out inside the circle, each one having 24 channels and being 0.6 m apart one from the other. Thus, a very good 3D mesh was formed. The inter-probe spacing was set to 0.60 m ( $a = 0.60$  m), and therefore the length of each tomography was 13.8 m. The maximum dipole separation was set to  $n = 8$ . The length of the measuring dipole was then doubled ( $2a$ ), and  $n_{max}$  was set to 7. Similarly, the length of the dipole increased up to  $5a$  (3.00 m) (Fig. 9.16).



**Fig. 9.16** Layout of the tomographies conducted at the eastern circle is in July 2016. A Google Earth satellite image is used as background

## ERT Interpretation

### *Western Tomb Area*

Figure 9.17 shows the distribution of the resistivity in the subsurface of the “western tomb area” at 1.70 m depth. The distribution was inferred from the 3D inversion of the data. Note that the color scale of the variation of the resistivity values is logarithmic. The high resistivities form a very clear pattern. Therefore, they are attributed to possible ancient structures.

Figures 9.18 and 9.19 show different views of the 3D subsurface distribution. The high resistivity anomaly at the western end of the sampled volume reflects the tomb whose entrance was exposed at the commencement of the survey. Ground truth testing in this area is described in the section below concerning excavations at Kastrouli.

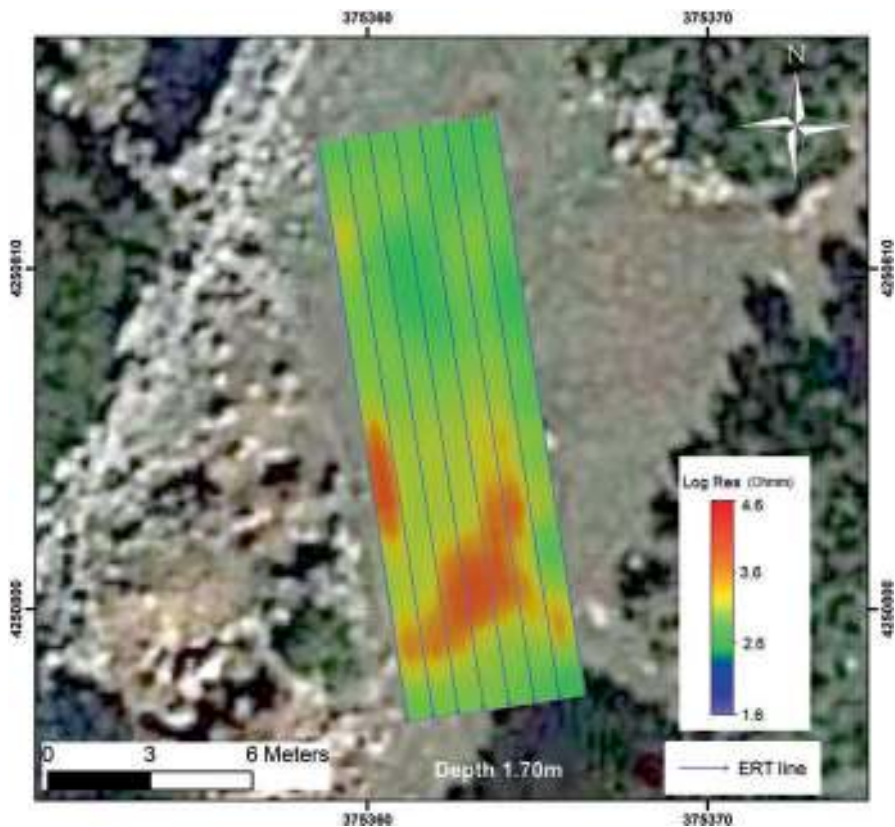
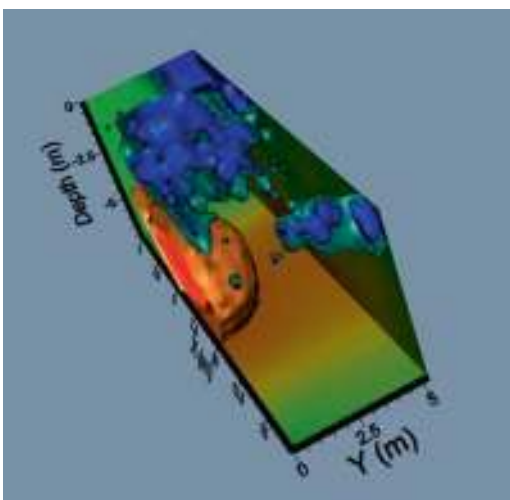
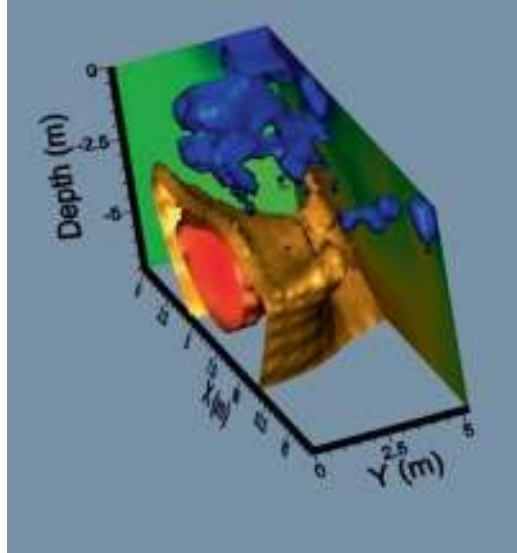


Fig. 9.17 Resistivity distribution (slice) at the depth of about 1.70 m for the “western tomb area”

Fig. 9.18 Three-dimensional distribution of the subsurface resistivity at the “western tomb area”



**Fig. 9.19** Three-dimensional distribution of the subsurface resistivity at the “western tomb area”



### *Eastern Circle*

Figures 9.20, 9.21 and 9.22 show the resistivity distribution at various depth slices for area at the “eastern circle.” These two-dimensional distributions of resistivity at various depths were inferred by slicing the three-dimensional volume of the inverted data. In all figures the depth to which each slice corresponds is marked on the relevant figure, but also it is referred in the captions. Note that the color scale of the variation of the resistivity values is logarithmic.

A pronounced magnetic anomaly is observed in all figures showing the subsurface resistivity at the “eastern circle” area. This anomaly is obviously caused by a

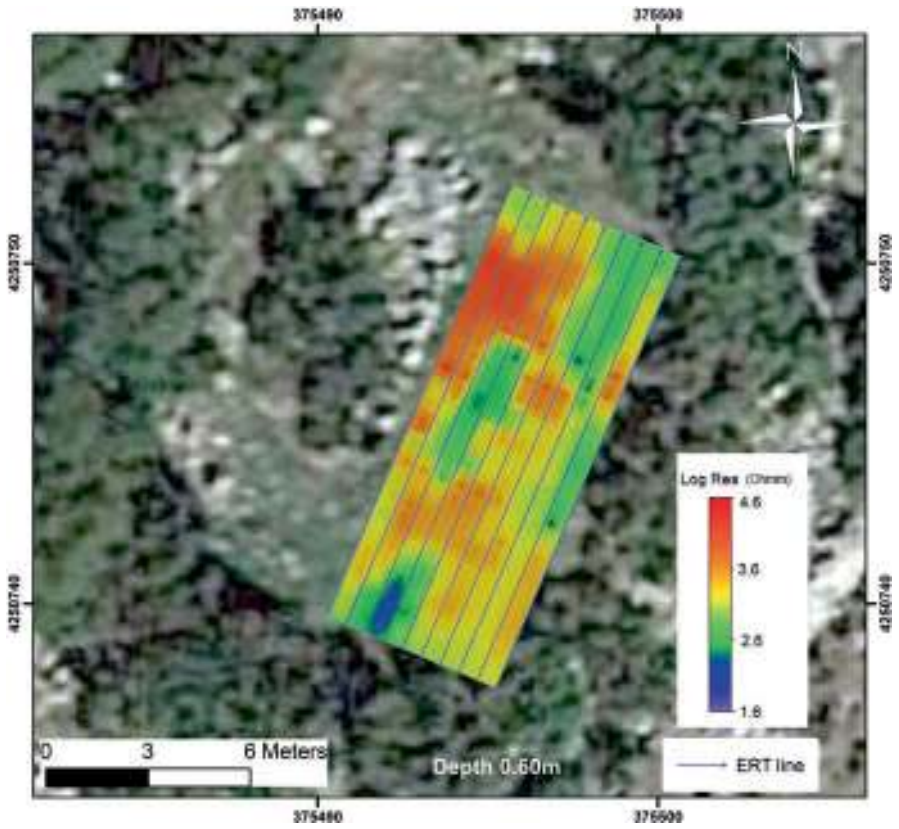


**Fig. 9.20** Resistivity distribution (slice) at the depth of about 0.60 m for the area of the “eastern circle”

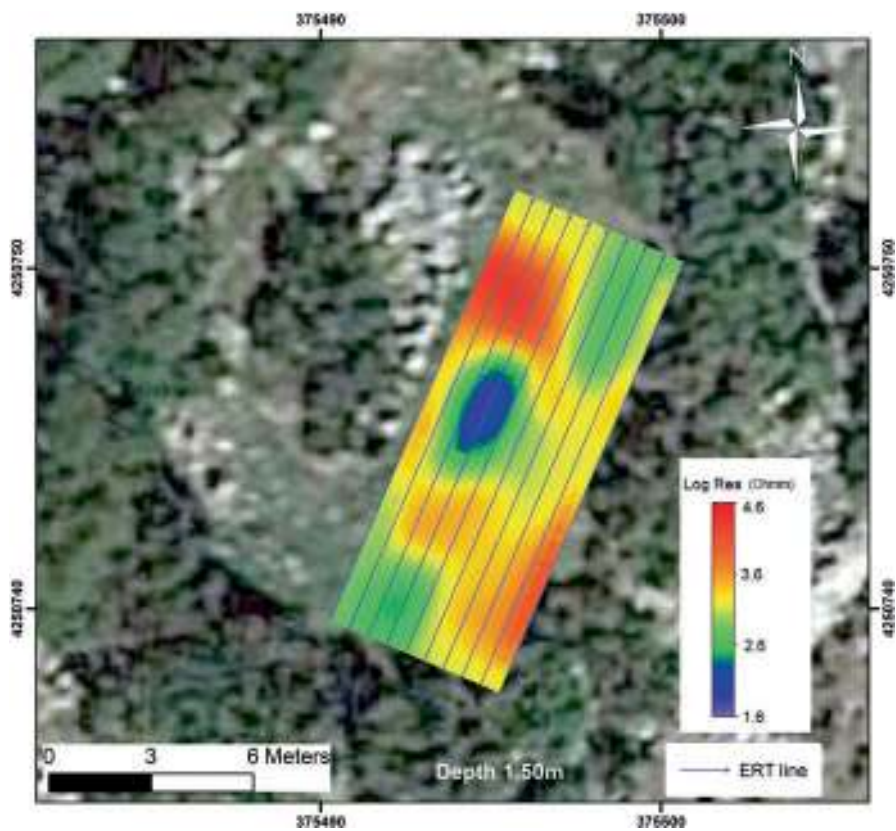


**Fig. 9.21** Resistivity distribution (slice) at the depth of about 1.50 m for the area of the “eastern circle”

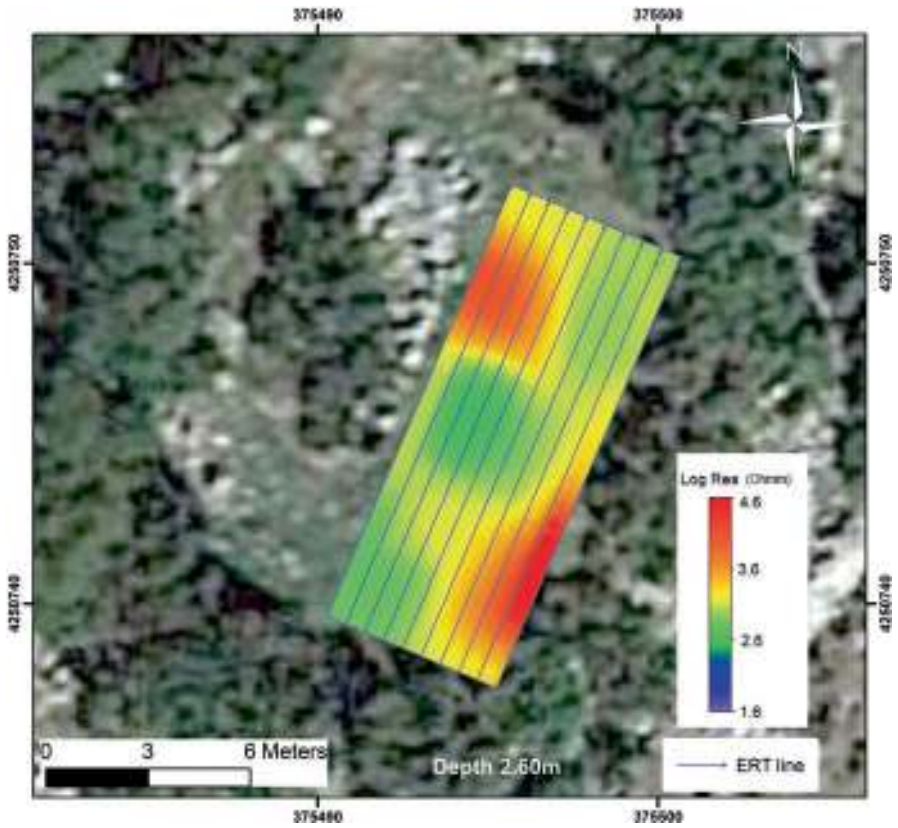


**Fig. 9.22** Resistivity distribution (slice) at the depth of about 2.60 m for the area of the “eastern circle”

hole at the resistive bedrock which may be a man-made pit. Figures 9.23 and 9.24 show different views of the 3D subsurface distribution. These images confirm the finding commented previously. The low resistivities are very clearly imaged both in the 2D slices and in the full 3D views suggesting the presence of a void that merits future investigation.

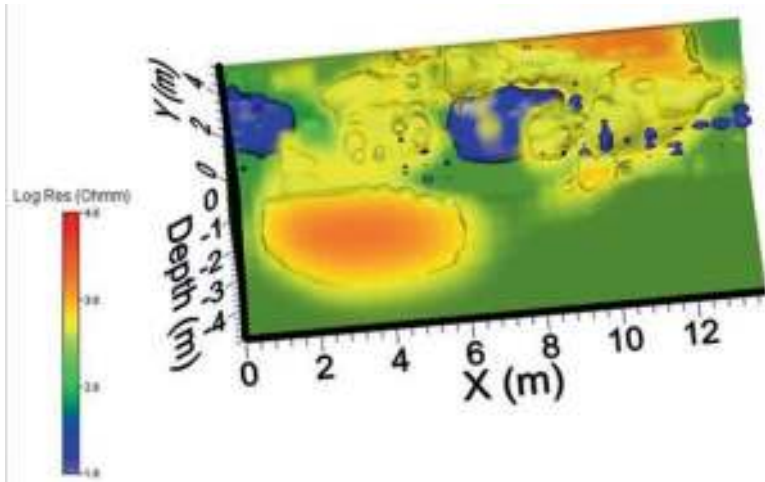


Fig. 9.23 Three-dimensional distribution of the subsurface resistivity at the “eastern circle”

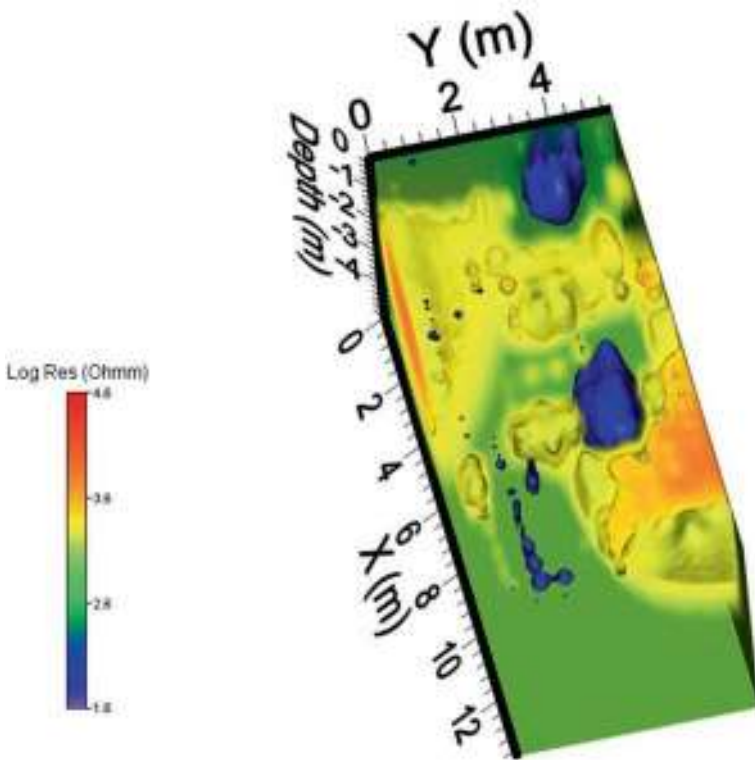


Fig. 9.24 Three-dimensional distribution of the subsurface resistivity at the “eastern circle”

### *Magnetic Survey in Sector C, Kastrouli*

A magnetic gradiometer survey was carried out northern and southern aspects of the site that are shown in Fig. 9.12. Also, magnetic susceptibility readings were carried out on pieces of masonry material (exclusively limestone) but also on the soil hosting the ancient ruins. The readings were performed using a SM-20  $\kappa$ -meter of *GF Geoinstruments*, and they are shown in Table 9.3.

It is evident from Table 9.3 that a pronounced difference of susceptibilities exists between the topsoil and the main material (limestone) used for building. Thus, magnetic prospecting was expected to produce reasonable results provided that other factors were also favorable (burial depth, size of targets, no ferrous garbage spread on the surface, no archaeological or man-made interferences, etc.).

Several meshes of grids were set on the ground surface at the top of the Kastrouli hill. In each mesh, 10×10 m<sup>2</sup> square cells were established that are shown in Fig. 9.12. The cells were referenced to the Greek Geodetic Reference System 1987 or Hellenic Grid (ΕΓΣΑ 1987). The corners of each cell were marked on the ground by wooden pegs. Then, a 0.5 m × 0.5 m grid was created in each cell using measuring tapes. That is, measurements were taken along traverses spaced 0.5 m apart each from the other, stepwise at 0.50 m intervals. For the square cells K3, K4, K5S, K6S, K7S, and K8S, the measuring step was set at 0.25 m. The orientational variation and zeroing of the instrument were checked initially and periodically after about 1.4 h of operation. Figure 9.25 shows members of the field crew when measuring at Kastrouli.

**Table 9.3** Mean values of magnetic susceptibility measurements

| Material                             | No of Samples | Susceptibility (SI)  |
|--------------------------------------|---------------|----------------------|
| Stones (masonry material), limestone | 4             | 7X10 <sup>-6</sup>   |
| Soil (Terra Rossa)                   | 5             | 3.7X10 <sup>-3</sup> |



**Fig. 9.25** Member of the field crew taking magnetic measurements

### **Processing of the Magnetic Data**

Data processing started essentially during the fieldwork and was completed afterward at the Laboratory of Exploration Geophysics, Aristotle University of Thessaloniki. The processing sequence was decided after various tests and included the following steps:

- Statistical analysis of the data.
- Transfer of the mean of each traverse to zero (zero mean traverse).
- Despiking by median filter which was performed in 3X3 windows of the data.
- Destagger of the even traverses to correct for small positional shifts between the traverses.
- High-pass filter.
- Interpolation both in the X and Y direction using cubic splines of the form  $\sin X/X$  (Scollar et al. 1986). This processing step was applied twice.
- Application of Wallis filter (Scollar et al. 1986).
- Creation of gray-scale images in order to have the result in a form which resembles the result that would have been pictured if excavation had taken place (Scollar et al. 1986).
- Transformation of the local coordinate system of each grid to the Greek Geodetic Reference System (1987). That is, the mesh of the geophysical cells was georeferenced.

## Result of the Magnetic Survey

Figures 9.26 and 9.27 show the spatial distribution of the processed gradients in the form of gray-scale image. The magnetic susceptibility readings shown earlier imply that the expected anomaly signatures of the buried Mycenaean ruins would have negative character. This is because the susceptibility of the limestone hewn blocks found to have almost negligible values whereas that of the covering soil to be about two orders of magnitude higher. Therefore, in our presentation, the low values appear with dark tones of gray, while the high ones are whiter. The gradients in the range of  $[-7, 7]$  nT/0.5 m are shown in Fig. 9.26 which are distributed in the gray-scale levels seen at the left side of the plot. All values that lie out of the defined range are depicted with white color if they are greater than 7 nT/m and black if they are lower than  $-7$  nT/m.

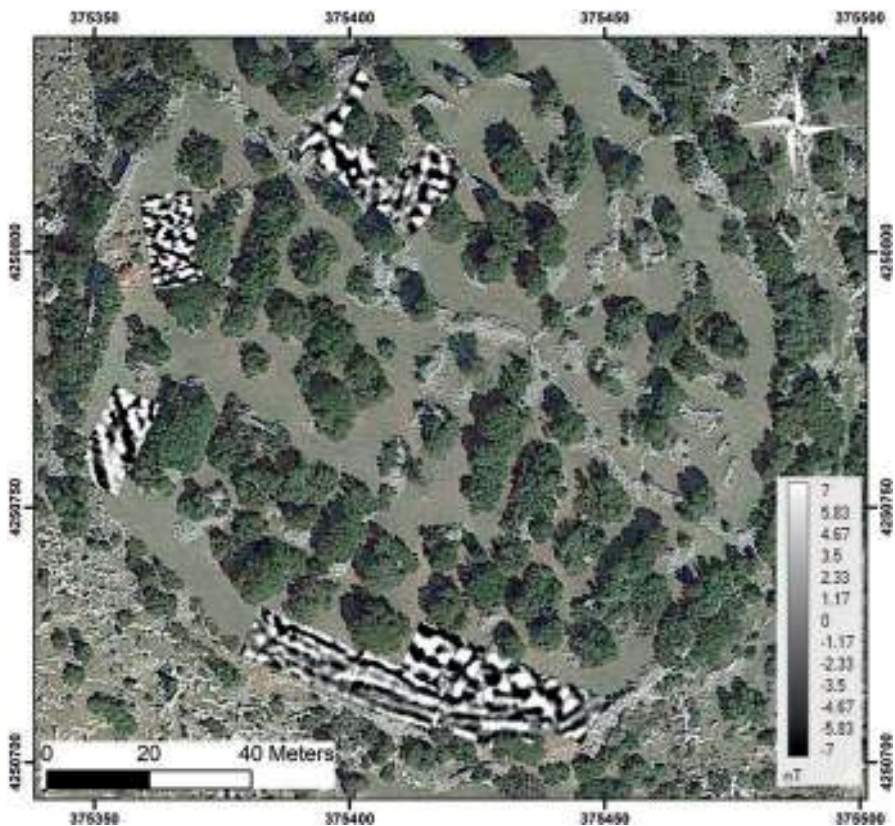


**Fig. 9.26** Distribution of the magnetic gradient in the area surveyed. The gradients are clipped to the range  $[-7,7]$ . The satellite picture of Google Earth has been used as background. The survey area at the south of the site was sampled in the summer of 2017 and revealed the foundations of a house (Liritzis, personal communication)

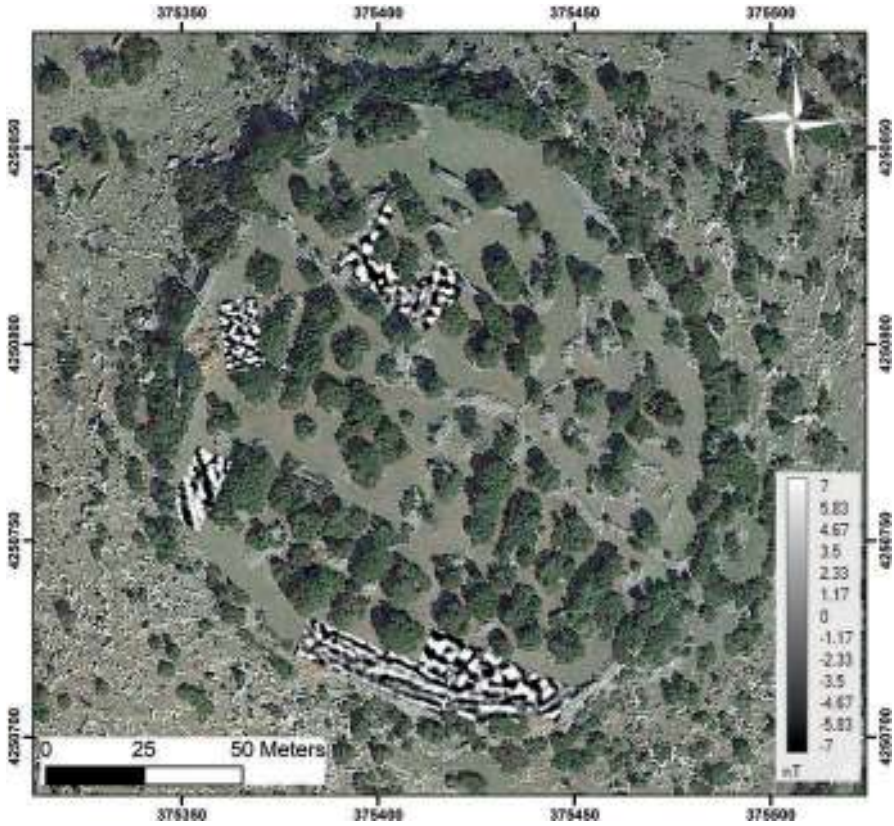


**Fig. 9.27** Another view of the distribution of the magnetic gradient. The plotting parameters are identical to those used for Fig. 9.2

The magnetic gradient records as they show up in the maps of figures presented above show that alignments of negative anomalies exist. They are articulated to form geometrical shapes, and therefore they are interpreted as being caused by sub-surface ruins of foundation walls. Figs. 9.28, 9.29, 9.30 and 9.31 show parts of the result of the magnetic gradiometer survey.



**Fig. 9.28** Distribution of the magnetic gradient in the area of the cells K1 and K2. This bit of land is in contact with the open pit that revealed the Mycenaean tomb at the western side of the hill of Kastrouli. The gradients are clipped to the range  $[-7,7]$ nT/m. The satellite picture of Google Earth has been used as background

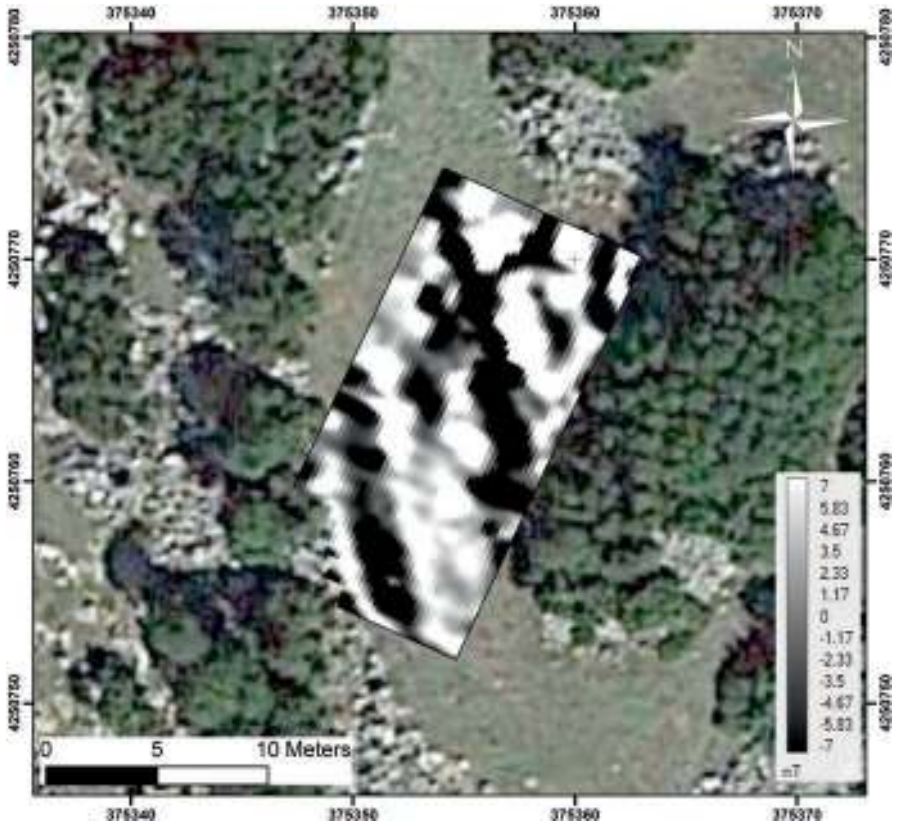


**Fig. 9.29** Distribution of the magnetic gradient in the area of the cells K3 and K4. The foundations of a Mycenaean building are exposed in the northeastern part of this bit of land. The gradients are clipped to the range  $[-7,7]$ nT/m, and the satellite picture of Google Earth has been used as background

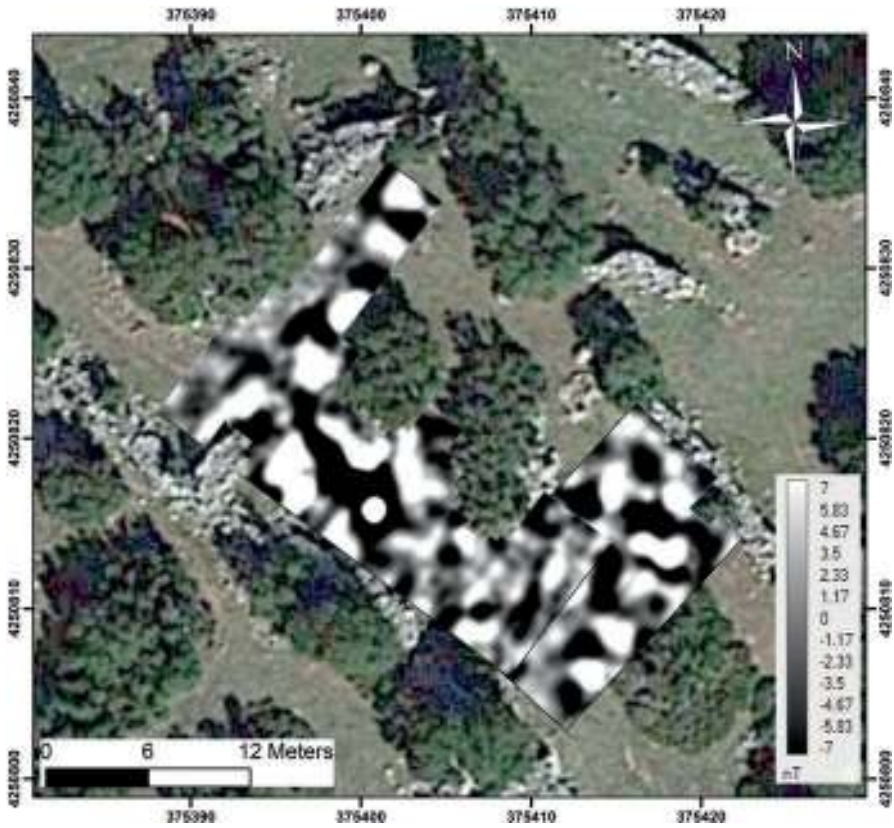


**Fig. 9.30** Distribution of the magnetic gradient in the area of the cells KO1, KO2, KO3, KO4, KO5, and KO5B. This bit of land is almost at the top of the Kastrouli hill. The gradients are clipped to the range  $[-7,7]$  nT/m, and the satellite picture of Google Earth has been used as background

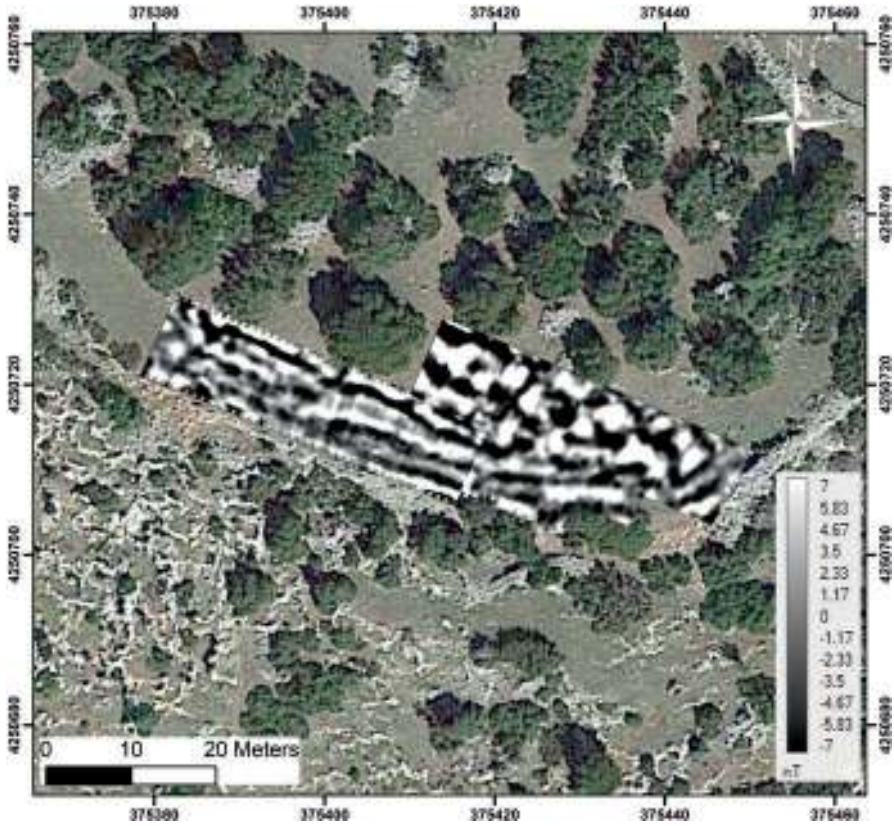


**Fig. 9.31** Distribution of the magnetic gradient in the area of the cells K5S, K6S, K7S, K8S, K9S, K10S, K11S, K12S, K13S, and K14S. This bit of land is at the south side of the Kastrouli hill. The gradients are clipped to the range  $[-7,7]$  nT/m, and the satellite picture of Google Earth has been used as background

***The Ground-Penetrating Radar (GPR) Survey: Data Acquisition and Processing***

GPR transects were carried out in cell K1 and K7S (Fig. 9.12), on the same grids that were established on the ground surface for carrying out the resistivity tomographies and magnetic gradiometry. Each transect was placed 0.5 m apart from its adjacent ones. One radiogram was recorded every 0.02 m. Evidently, the case comprises a high-resolution survey. The antennae ABEM RAMAC of MALA Company were used having central frequency at 500 MHz. Figure 9.32 shows members of the crew during the fieldwork. The radiograms subjected to removal of the inductive component (Dewow filtering) by calculating the moving averages into windows of



**Fig. 9.32** Members of the field crew carrying out GPR measurements at Kastrouli

15.068 ns. Trace equalization was applied next and median filtering in distance followed using an operator of three traces wide. A custom gain function applied to account for the losses resulted by geometrical spreading and attenuation.

### **GPR Results**

Regarding the “western tomb area,” i.e., the cell K1 of the grid established both for magnetics and GPR (Fig. 9.12), the processed radar transects were combined to produce depth slices. Two depth slices showing the subsurface distribution of the amplitude of the electromagnetic waves at about 0.74 and 0.93 m are shown, respectively, in Figs. 9.33 and 9.34. The results are rather pure showing very little signal, a fact that is attributed to the high attenuation rate of the soil in the particular site because of the clay cover. The inadequacy of the method in the specific conditions is pronounced when its results are compared with the respective magnetic and ERT results. Nevertheless, some linear features are revealed also in these slices reinforcing the interpretation of the magnetic gradiometry map. A subterranean hollow identified with GPR was found through ground truth excavations and described in the section below concerning the Tomb A excavation.

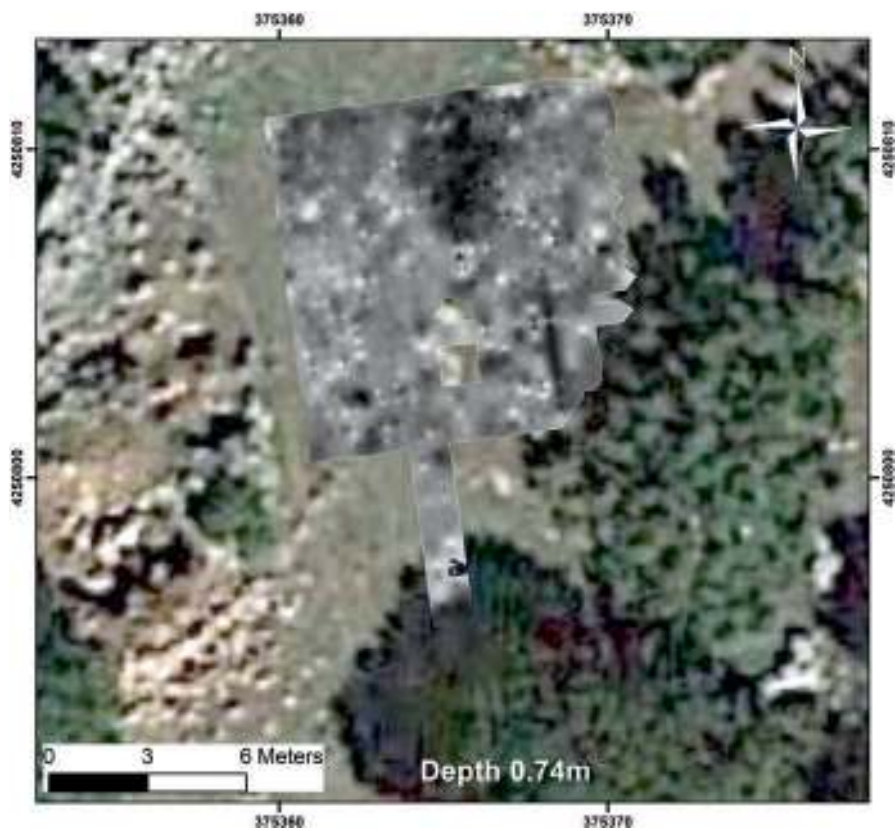


Fig. 9.33 The GPR slice at 0.74 m depth



Fig. 9.34 The GPR slice at 0.98 m depth

Respectively, the results in the cell K7S (Fig. 9.12) are shown as depth slice depicting the subsurface distribution of the amplitude of the electromagnetic waves at about 0.99 m in Fig. 9.35 in gray scale. Figure 9.36 shows the same slice but in color scale.

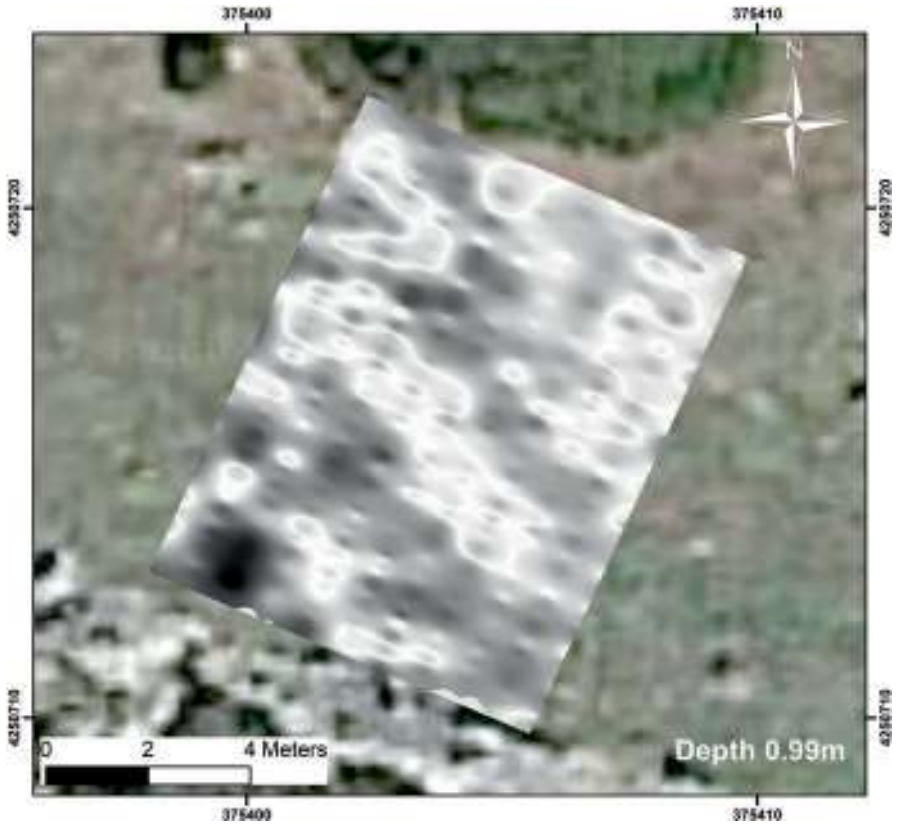


Fig. 9.35 The GPR slice at 0.99 m depth for cell K7S

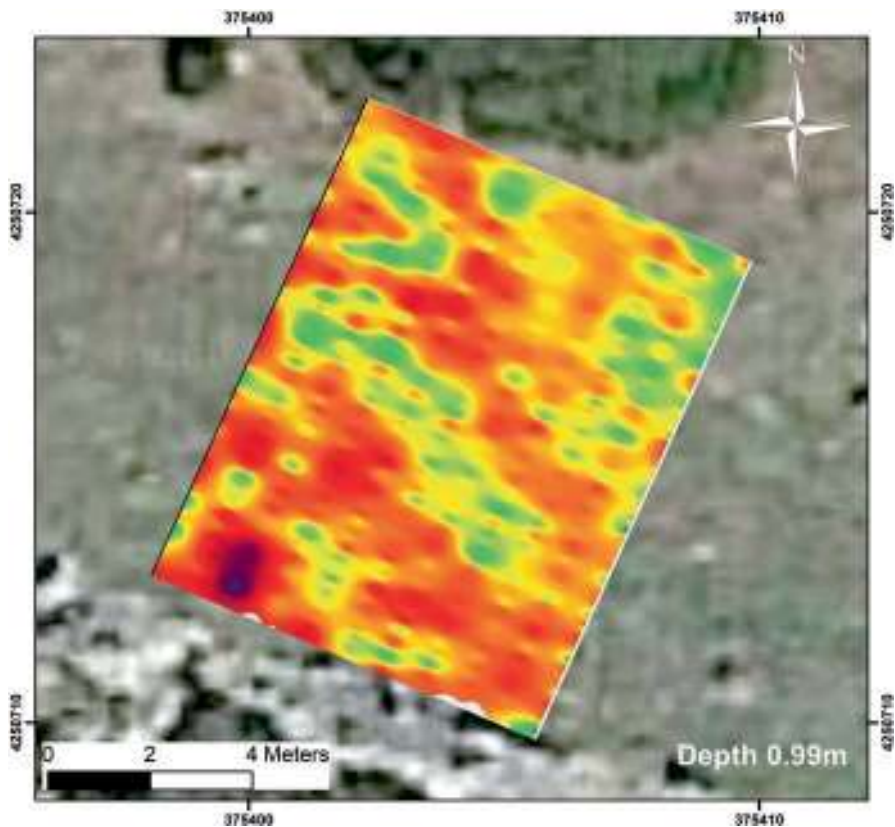


Fig. 9.36 The GPR slice at 0.99 m depth for cell K7S in color scale

## Summary

Almost all the existing methods for archaeological prospection were applied at the investigations at Kastrouli. Anomalies of the geophysical fields were detected which were attributed to the presence of concealed ancient remains or structures. In some cases, these anomalies appear with linear shape or tend to create well-defined geometrical shapes. The geophysical images must be seen as a dynamic element, and their interpretation may be altered or complemented with new aspects after the excavations. In other words, the final conclusions should be inferred after the excavation of a part of the surveyed area. Ground-truth excavations confirmed many of the subterranean targets identified with the different geophysical techniques applied

at the Kastrouli, Mycenaean settlement. The preliminary results presented here indicate the great potential for extensive excavation at the site and the need for more intensive data processing to facilitate further interpretation.

### ***Excavations at Kastrouli 2016***

Excavation at the site was based on an arbitrary site grid, consisting of 5 m × 5 m squares, covering the entire site. Squares were named based on their position in the grid by counting squares in the x and y directions, respectively, and separating these values with a slash (e.g., Square 4/20 is the fourth square east and the 20th square north from the arbitrary origin to the southwest of the site). This was a system determined by A. Sideris. During the 2016 season, excavations took place in three areas: Area A, consisting of excavation in Squares 5/19, 6/19, and 7/19, and two small wall section samples in unnamed areas. One sampling of the northwestern fortification wall of the site occurred in squares 5/21 and 5/22, while a sampling of the southern fortification wall occurred in Square 21/2. Since Tomb A stretched across both Squares 5/19 and 6/19, no balk was established between these squares. During excavation in Area A, a 100% sieving strategy was adopted in order to ensure the collection of material culture missed in excavation or smaller finds not immediately apparent (1 cm mesh for loci outside the tomb and ~3 mm mesh for those within the tomb). All artifact finds and locus boundaries were recorded using a total station (see below for further details).

The contour map of Kastrouli was produced using balloon aerial photography, image-based modeling in Agisoft Photoscan and ArcGIS (Fig. 9.37). Once aerial images of the site were acquired and processed in Agisoft, the dense point cloud was classified to remove vegetation from the 3D model in order to generate a digital surface model (DSM). This DSM was used as the basis for contour generation in ArcGIS. The production of this map took a total of 32 h (balloon photography, 2 h; Agisoft processing, 24 h; point cloud classification and digital surface model (DSM) production, 3 h; final GIS work, 3 h (Map by M. Howland, Center for Cyber-Archaeology and Sustainability, UC San Diego).



custom computer programs/hardware developed specifically for solving archaeology/cultural heritage problems that researchers face worldwide. The current excavation season utilized several aspects of this spatial recording methodology in order to precisely document the coordinates of archaeological remains at the highest possible spatial resolution in three dimensions. Spatial data was collected with a Leica TS02 total station and the data interface software, *ArchField* (developed by Dr. Neil Smith), that provides real-time data recording and review in the field (the total station was connected to a Microsoft Surface with *ArchField* installed). *ArchField* allows the excavators to record and visualize both points and polygons (i.e., artifact finds and loci) in the field, and the relevant data (i.e., locus type, artifact type, etc.) can be immediately provided and databased. In addition, spatial information collected by *ArchField* is easily exported to a geographic information system (GIS) for further manipulation and analysis (Fig. 9.38). All artifacts collected and recorded with *ArchField* were attributed a unique basket number and bar code to facilitate entry into the *ArchaeoSTOR* artifact database, another custom application allowing for the categorization and sorting of artifacts in the field and in the lab, along with spatial visualization and statistics applications (Gidding et al. 2011). Following field data collection, spatial data linked with artifacts through their basket number/bar code were processed into *ArchaeoSTOR* (Gidding et al. 2014) along with all relevant artifact information (weights, counts, material type, etc.). *ArchaeoSTOR* was recently redeveloped by three undergraduate students from the University of California, San Diego (Rose Smith, Carolyn Breeze, and Taylor Harman) who managed the database and artifact entry in the lab after each day of excavation. Qualitative data regarding archaeological contexts (i.e., loci) was recorded using a Microsoft Access database.

### ***Aerial Photography and Structure from Motion***

In addition to the recording of point finds and locus outlines using *ArchField*, the excavation team also adopted an intensive Structure from Motion (SfM) recording campaign in order to document the site in 3D over the course of excavation using the UC San Diego helium balloon system. SfM is a software technology allowing for the creation of highly accurate and photo-realistic 3D models through photogrammetric techniques. The team adopted a two-part approach to SfM data capture: terrestrial and aerial SfM photography. In both approaches, overlapping photographs encompassing the area of interest are captured with complete coverage to facilitate the construction of a 3D model. For aerial photography, a Canon EOS 50D digital single-lens reflex camera (outfitted with a 18 mm lens) is attached by frame to a Kingfisher Aerostat balloon which is walked in overlapping transects over the area of interest. This data collection strategy, an ideal approach to SfM modeling developed through trial and error, was sufficient to develop high-quality 3D models on the site and excavation area scale. The same camera equipment was used terrestrially to capture data used for the production of SfM models at an excavation square scale. In both cases of data capture, these models were subsequently georeferenced,

### Final ArchField Points and Polygons from Kastrouli, 2016

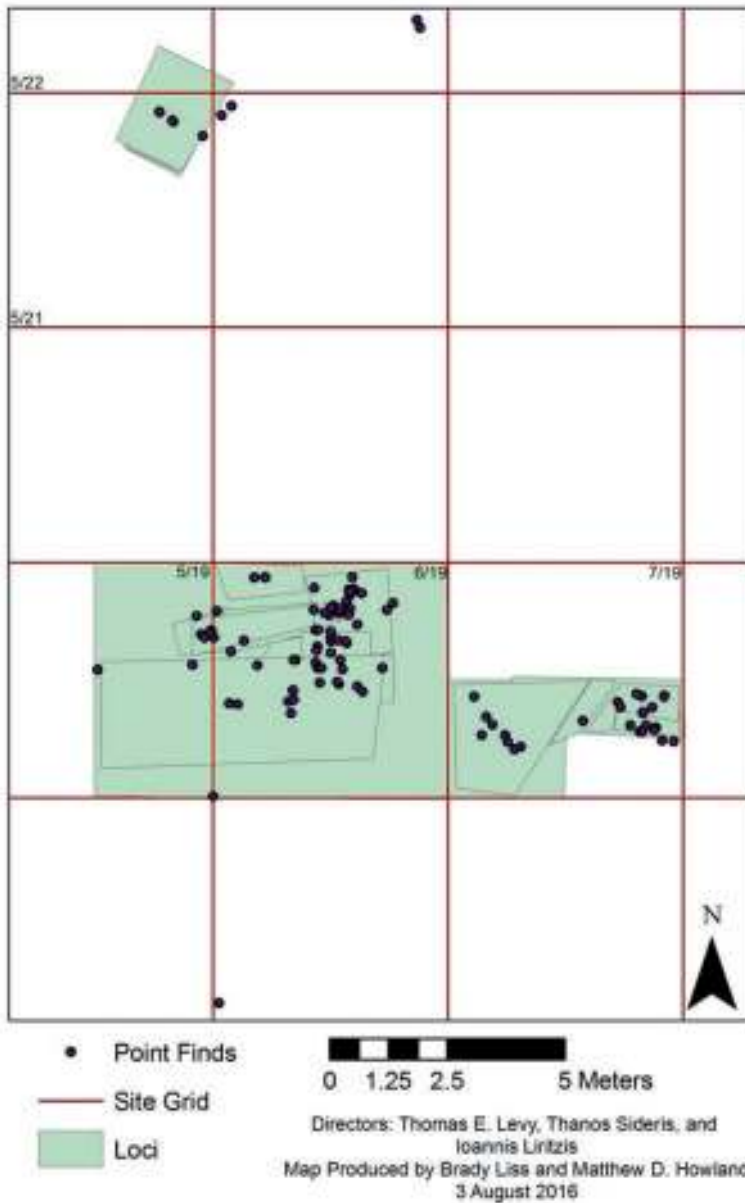


Fig. 9.38 Final export of all *ArchField* points and polygons

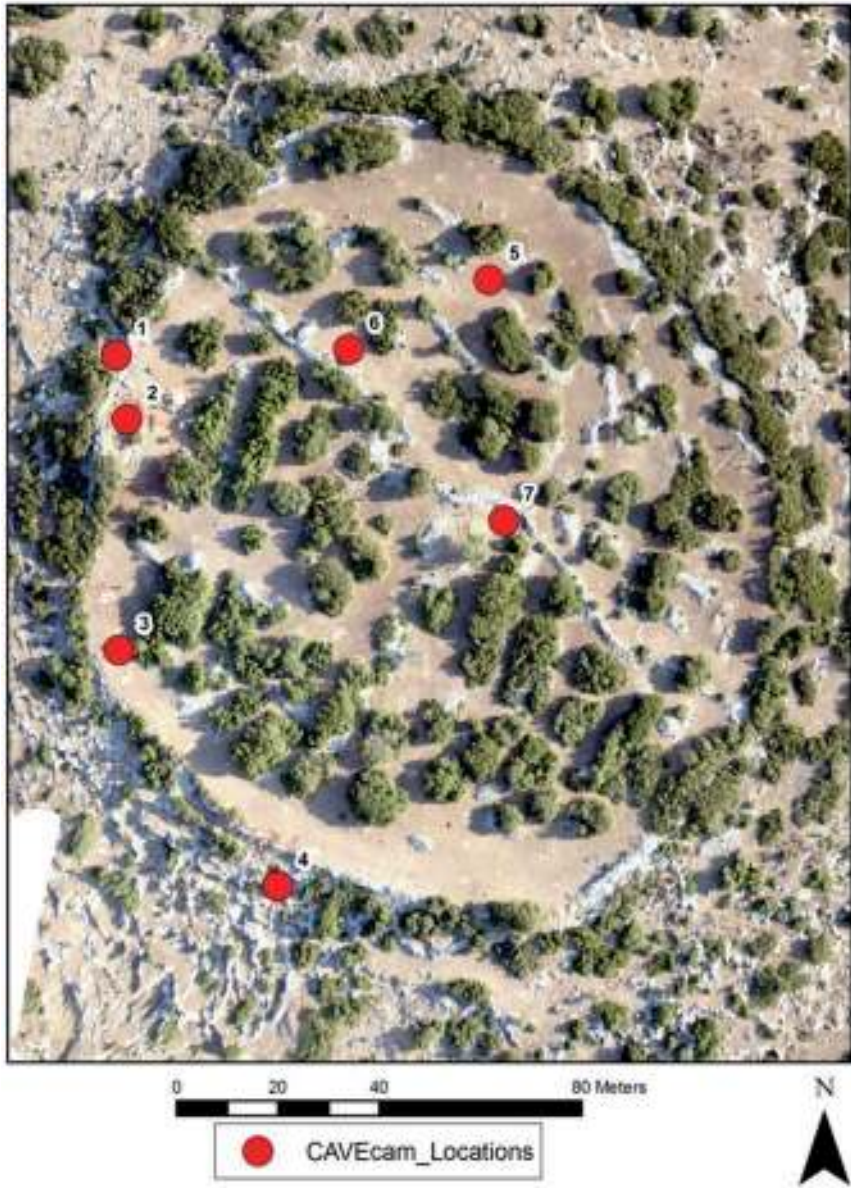
facilitating the export of high-resolution orthophotos which serve as an excellent basis for GIS-based digitization of architectural features. This strategy was used for the digitization of top plans. Furthermore, SfM was used for section drawing the walls in the dromos and tomb; orthophotos provided a base for digitization within in GIS rather than hand drawing in the field.

### *CAVEcam Stereo Photography*

Along with SfM, many parts of Kastrouli were documented in 3D using the CAVEcam system (Ainsworth 2012). The CAVEcam is a platform for shooting stereo photography in 360 degrees. The system creates 3D GigaPan images by shooting a grid of photographs across an area of interest with two cameras. To do so, it combines a dual-camera image capture system with a GigaPan EPIC Pro Robotic Controller (Ainsworth 2012). The dual-camera system includes two Panasonic Lumix® GF-1 cameras which provide 12.1 megapixel resolution despite being relatively small for mounting side by side in the controller (Ainsworth 2012: 3). By bracketing the cameras next to each other, they collect two sets of images with slightly differing perspectives to provide stereoscopic vision (much like human eyes). The robotic mount affords automated movement for the cameras in 360 degrees horizontally and up to 180 degrees vertically; this is outfitted with an Ainsworth CC-1 Dual-Camera Controller to automatically capture images from both cameras simultaneously. The GigaPan mount can be programmed to accommodate the desired number of images for the location. Together, the dual cameras and robotic platform create two grids of images (6x12 photos) covering up to 360 degrees from distinct perspectives. These grids of photographs are individually stitched (using the PTGui® Pro software) and displayed to create a single, high-resolution 3D image, which cannot be portrayed in 3D here but represented in Fig. 9.69.

At Kastrouli, CAVEcam photography was captured (by graduate student Tom Holm, University of California, San Diego) at seven locations of interest around the site (Fig. 9.39). Locations 1 and 2 represent two of the excavation areas during the 2016 season, the northern wall section and the tomb excavations, respectively. Location 3 was selected to capture part of the site's fortification wall and the valley in which the site is positioned. Location 4 similarly captured part of the fortification wall but from an outside perspective and some of the terracing around the site. Locations 5, 6, and 7 were all selected to image various architectural features around the center of the site.

### CAVEcam Locations at Kastrouli



Directors: Thomas E. Levy, Thanos Sideris, and Ioannis Liritzis  
Map Produced by: Brady Liss and Matthew D. Howland  
CAVEcams Captured by: Tom Holm

Fig. 9.39 Locations of CAVEcam imagery around Kastrouli (Map by M. Howland Center for Cyber-Archaeology and Sustainability, UC San Diego)

## Stratigraphy and Excavation

The 2016 excavations at Kastrouli are preliminarily divided into three strata (Sideris et al. 2017). Surface materials and loci are clearly disturbed by looting, and/or the previous excavations are attributed to Stratum I. The site's fortification wall is believed to be later in date than the tombs based on its close (potentially cutting) construction to the dromos entrance of the tomb. As such, loci associated with the wall section excavations are assigned Stratum II. In addition, undisturbed loci from square 7/19 (Wall 116, Fill 114, and Ashy-Feature 115) are also attributed to Stratum II as it is likely that they are later in date than the tomb (however, this requires further investigation through ceramic typology or other dating methods). Undisturbed loci from within the tomb itself (Loci 112 and 121) are attributed to Stratum III as they are likely the earliest excavated loci. These loci (112 and 121) are associated with the human remains and seem to be the only undisturbed contexts within the tomb.

### *Area A*

#### **Squares 5/19 and 6/19: Tomb Excavation**

##### Stratum I

Stratum I in Squares 5/19 and 6/19 consist of all loci that are considered to have been disturbed by looting, excavation, or by general surface disturbance (Fig. 9.40). These include Loci 100, 101, 102, 104, 107, 108, 109, 110, 111, 119, and 120.

Excavation of Squares 5/19 and 6/19 began with the opening of two general cleaning loci (L100 and L101) (Fig. 9.41), which related to the weeding and cleaning of the surface areas of squares 5/19 (L101) and 6/19 (L100). These loci included the cleaning of some very disturbed fill/topsoil, which was sieved at 100% through 1 cm mesh. Also included in these loci was the cleaning of some disturbed fill inside the tomb.

Following the cleaning of the surface areas of each square and limited cleaning within the tomb, Locus 102 was opened below L100 in order to excavate the area immediately south of the tomb in Square 6/19 and to delineate the southern edge of the largest lintel stone covering the tomb (Fig. 9.42). Excavation in this locus both defined the edge of the large lintel stone and also cleaned and delineated the stones to the south of the lintel. Locus 104 was subsequently opened below L100 on the north end of the lintel stone in order to delineate its northern edge in Square 6/19. The excavated material was disturbed fill from the looting and previous excavation of the tombs. The locus successfully discovered the edge of the lintel stone, resulting in the complete exposure of the two lintel stones still in place over the top of the dromos and the leveling of fill to a height equivalent to the top course of stones in the walls of the tomb. Excavation in Locus 102 and 104 was ceased at this level to avoid destabilizing the tomb walls.

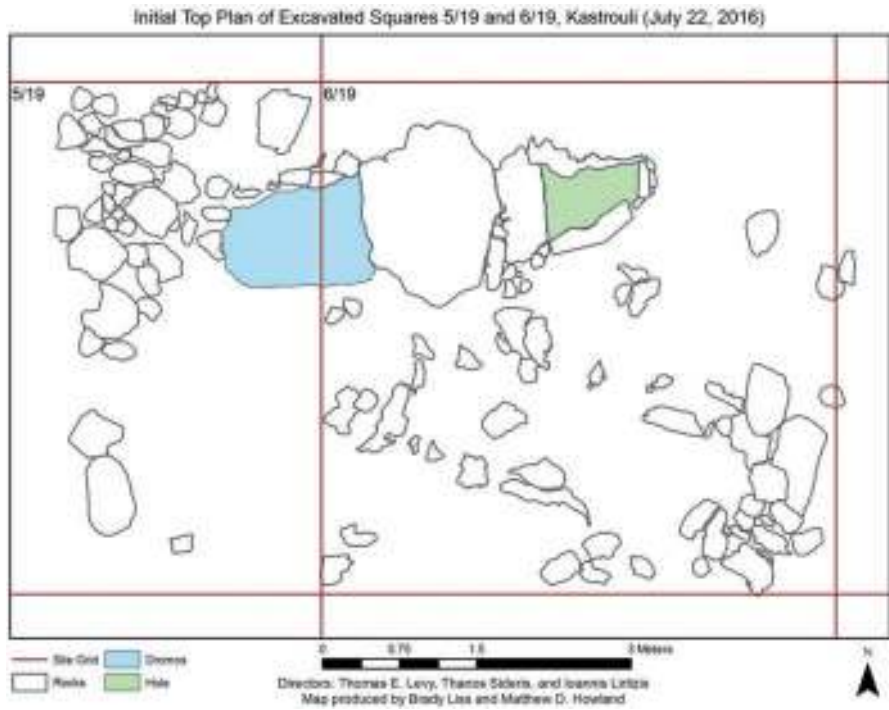


Fig. 9.40 Top plan from the beginning of excavation in Squares 5/19 and 6/19 at Kastrouli



Fig. 9.41 Locus 100 (cleaning locus of Square 5/19) and Locus 101 (cleaning locus of Square 6/19) (Photo – T.E. Levy, Center for Cyber-Archaeology and Sustainability, UC San Diego)

**Fig. 9.42** Locus 102 (excavating southern end of lintel stone) and Locus 104 (excavating northern end of lintel stone) (Photo – T.E. Levy, Center for Cyber-Archaeology and Sustainability, UC San Diego)



**Fig. 9.43** Locus 107 –excavating in eastern access hole to tomb in Square 6/19 (Photo – T.E. Levy, Center for Cyber-Archaeology and Sustainability, UC San Diego)

Locus 107 (Fig. 9.43) was a fill locus in Square 6/19 arbitrarily opened below Locus 100 and contemporary with L108. This locus represents excavation in the interior of the tomb within Square 6/19, accessed through the eastern “opening” to the tomb. The aim of the locus was to remove disturbed fill from the tomb while defining the northern and southern interior walls of the tomb. Excavation in this

**Fig. 9.44** Locus 108 – excavating in dromos in Square 5/19 (Photo – T.E. Levy, Center for Cyber-Archaeology and Sustainability, UC San Diego)



locus discovered some fragments of human remains and a stone spindle whorl. While the *ArchField* polygon for this locus represents only the eastern opening to the tomb, the interior of the tomb opens up into a larger area once inside. In practice, the western boundary of this locus was the eastern edge of the eastern lintel, with the entire interior of the tomb east of that line being considered part of L107, resulting in point finds appearing to be outside the locus. A collapsed lintel stone in the tomb was clarified through excavation in this locus. This stone also served as an informal western boundary of the locus in the tomb. This large lintel stone was removed, and a new locus (110) was opened in order to excavate the entire tomb and dromos as a single locus, resulting in the closing of L107.

Locus 108 (Fig. 9.44) was a fill locus in Square 5/19 arbitrarily opened below Locus 101 and contemporary with L107. This locus represented the dromos (western) entrance to the previously looted tomb in Area A. The aim of the locus was to remove disturbed fill from the area of the tomb in Square 5/19 and continue to define the northern and southern walls of the dromos. Excavation in this locus was rapid with large picks and hoes, due to the disturbed nature of the sediment. A conical stone bead was discovered in the sifted material excavated from the locus. This locus was closed after the collapsed lintel stone in the tomb was removed, and a new locus (110) was opened in order to excavate the entire tomb and dromos as a single locus.

Locus 109 (Fig. 9.45) was opened below L100 and contemporary with L102 and L104 in order to remove the disturbed fill material on top of the lintel support stones around the eastern opening to the tomb. The goal of the locus was to delineate the edges of the lintel support stones (i.e., the top stones in the walls of the tomb, just



**Fig. 9.45** Locus 109 – excavating around eastern access hole to reveal lintel supports in Square 6/19 (Photo – T.E. Levy, Center for Cyber-Archaeology and Sustainability, UC San Diego)



**Fig. 9.46** Locus 110 – excavating across dromos and tomb in Squares 5/19 and 6/19 (Photo – T.E. Levy, Center for Cyber-Archaeology and Sustainability, UC San Diego)

below where the collapsed lintels would have sat) on the north, east, and south edges of the opening. L109 successfully discovered and defined the exterior edges of the lintel support stones, but it was left open in case excavation should continue. The locus was closed on the final day of the 2016 season.

Locus 110 (Fig. 9.46) was originally opened in order to excavate the sediment beneath the collapsed lintel stone (following its removal) within the tomb in square 6/19. Once the sediment immediately beneath the stone was leveled to be consistent

with the rest of the tomb (loci 107 and 108), Locus 110 was extended to encompass the entire interior of the tomb and dromos, replacing Loci 107 and 108 and below them. The goal of the locus was to continue to excavate the fill material within the tomb to discover its floor and the founding levels of the walls. During excavation in the locus, a modern safety pin was discovered in the sieve reiterating the disturbed nature of the locus and the tomb. Locus 110 was excavated down to bedrock in the central part of the dromos. At the eastern end of the locus, a vertical slab of worked bedrock was discovered representing the eastern end of the tomb. However, the tomb appeared to have another chamber to the south, and Locus 111 was opened in order to further pursue this possibility, at which time Locus 110 was closed.

Locus 111 (Fig. 9.47) was arbitrarily opened below L110 in Square 6/19 to excavate fill material in the eastern end of the tomb. The locus was opened beneath locus 110 when vertical, worked bedrock was discovered at the eastern edge of the tomb. The goal of the locus was to excavate the fill down to the floor of the tomb which was presumably bedrock and had been discovered in the dromos. During excavations of the locus, a modern fragment of film was discovered in the sieve reiterating the disturbed nature of the locus and the tomb. The locus was closed when a significant concentration of bone was discovered, a comingled secondary burial, which was excavated as Locus 112 (Fig. 9.48; Chovalopoulou et al. 2017).

Locus 119 (Fig. 9.49) was opened to the south of the eastern access hole to the tomb (Square 6/19) in order to excavate the topsoil around the surface of the tomb. While the locus was initially restricted to only the area immediately south of the eastern access, it was subsequently expanded to the south and west, running into Square 5/19. Locus 119 was primarily excavated by three local workers, and it was excavated quickly with large picks. Despite the disturbed nature of the locus, it still



**Fig. 9.47** Locus 111 – excavating in eastern end of tomb in Square 6/19 (Photo – T.E. Levy, Center for Cyber-Archaeology and Sustainability, UC San Diego)

**Fig. 9.48** Locus 112 – dense collection of human remains, possible secondary burial, in Square 6/19 (Photo – T.E. Levy, Center for Cyber-Archaeology and Sustainability, UC San Diego)



**Fig. 9.49** Locus 119 – excavating fill to the south of the tomb in Squares 5/19 and 6/19 (Photo – T.E. Levy, Center for Cyber-Archaeology and Sustainability, UC San Diego)

yielded significant pottery and a broken Phi-figurine. As the locus was excavated to a lower elevation, many large stones were discovered that are potentially part of the tomb architecture. Two large slabs discovered in the southeast corner of Square 6/19 are possibly lintel stones (similar in size and shape to those associated with the tomb), and one is clearly collapsed or disturbed by looters as it is tipped on its side. To the west of these large slabs, many smaller stones (ca. 30 cm in diameter) were discovered that are possible architectural collapse from the tomb(s) as well.

Locus 120, the final locus in Area A attributed to Stratum I, was opened to excavate the fill in the southern chamber of the tomb (Fig. 9.50). This chamber was not

**Fig. 9.50** Locus 120 – excavating fill (disturbed by looters) in the tomb in Square 6/19. South section prior to removal of fill to expose full extent of comingled burial (Photo – T.E. Levy, Center for Cyber-Archaeology and Sustainability, UC San Diego)



excavated with the rest of the tomb/dromos, and it appeared to be topped with a large, masoned lintel stone and backed by a vertical, flat slab. This initial locus consisted primarily of fill with some pottery and bone fragments. During excavation, a plastic cup was found, likely indicating that this locus was disturbed by looters or the recent excavations. Locus 120 was excavated down to the possible secondary burials within the tomb across its eastern end and southern chamber (opened as Locus 121 and contemporary with Locus 112).

### Stratum II

No loci from Square 5/19 and Square 6/19 were assigned to Stratum II as loci in this stratum are insecure contexts that likely postdate the tomb.

### Stratum III

The only loci attributed to Stratum III in Squares 5/19 and 6/19 are Locus 112 and Locus 121. Moreover, these are the only loci that appeared to be from undisturbed contexts; this is evidenced by the well-preserved conditions of the human remains and the compact sediment in which they were embedded. Locus 112 was opened

beneath Locus 111 in the eastern end of the tomb in Area A when a significant concentration of human remains was discovered against the worked bedrock. The goal of the locus was to excavate the bones and associated material culture. The human remains did not appear to be articulated but were significant in number (hundreds of complete bones and fragments). It is possible that these bones represent a secondary burial. This locus focused only on the human remains at the eastern extent of the tomb (against the worked bedrock), but the bones continued to the south into a possible second chamber (Locus 121). The locus was closed when all the bones were removed and the bedrock floor was discovered.

Locus 121 (Fig. 9.51) represents the continuation of the bones seen in Locus 112 into the southern chamber of the tomb (below Locus 120). Excavation in this locus uncovered hundreds of human bones (thousands of bone fragments) and many sherds of Mycenaean stirrup jars in situ. Excavation in this locus also recovered a spindle whorl, three figurines (Phi- and Psi-figurines), and a fragment of gold (crumpled gold foil) in situ. In addition a bone bead, a possible seal, and three gold fragments (also crumpled gold foil) were recovered from the sieve. The locus was closed on the final day of excavation; the bedrock beneath the locus was fully exposed, and all of the human remains were excavated. Top plans and section plans of the fully exposed tomb are shown in Figs. 9.52, 9.53 and 9.54.



**Fig. 9.51** Locus 121 – dense collection of human remains, probably secondary burial, in Square 6/19 (Photo – T.E. Levy, Center for Cyber-Archaeology and Sustainability, UC San Diego)

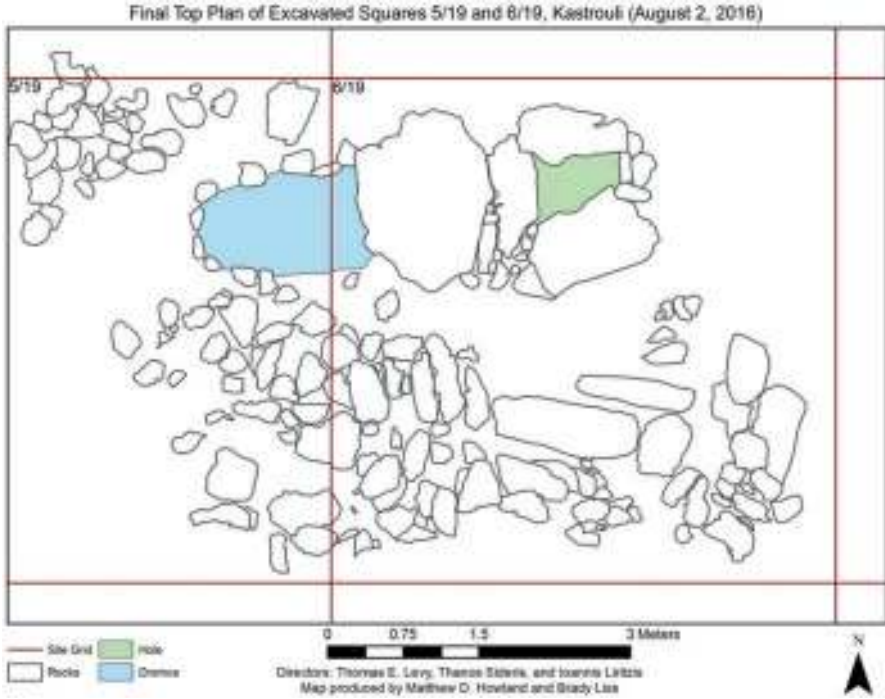


Fig. 9.52 Final top plan from the last day of excavation in Squares 5/19 and 6/19 at Kastrouli

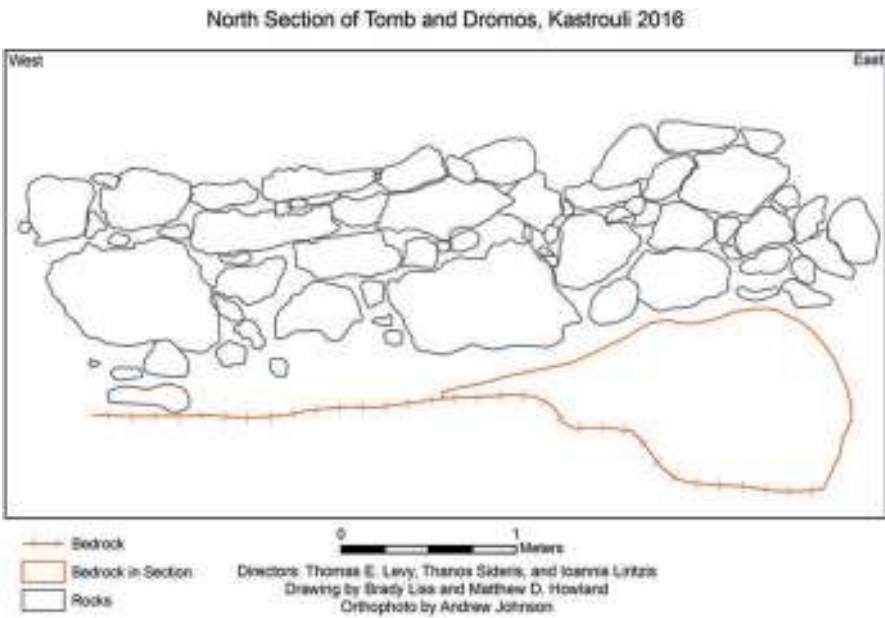


Fig. 9.53 Northern section drawing of tomb and dromos

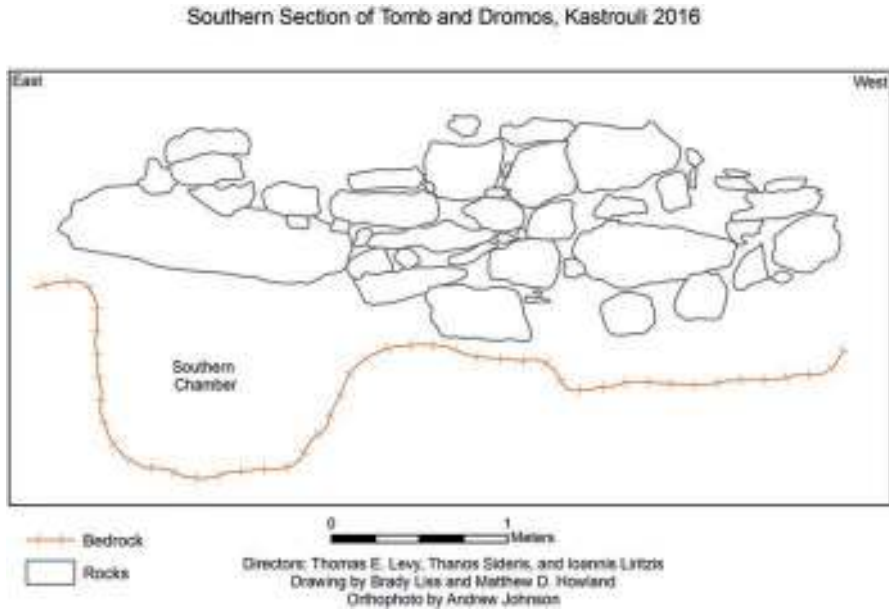


Fig. 9.54 Southern section drawing of tomb and dromos

### Interpretation

Tomb A represented the main focus of excavation during the 2016 field season. All loci in squares 5/19 and 6/19 are grouped into Strata I and III, reflecting a general divide in excavated loci between disturbed and undisturbed contexts, respectively. In the area of the tomb, the potential for disturbance was high given the recent occurrence of looting and limited archaeological excavation. Excavation in all loci now grouped in Stratum I corroborates the likelihood of disturbance, given a lack of clear stratification and the limited density of finds. The presence of two fragments of modern debris (a piece of photographic film and a fragment of a plastic cup), the latter of which was found during excavation, also evidence the disturbed nature of these loci. Loci (112 and 121) classified in Stratum III, however, seem to be undisturbed, based on the density of relatively intact human bones interspersed with relatively large fragments of diagnostic pottery sherds. L112 and L121, which represent the same ancient context and are separated only for reasons of excavation process, seem to represent a multiple secondary burial, based on the disarticulation of the bones. The comingled bones of multiple individuals and grave goods with no apparent orientation also suggest that multiple burials in the tomb may have been collected and condensed in one part of the tomb in order to clear space for later burials or activities in ancient times. The discovery of gold foil fragments, figurines, and finely decorated ceramics indicates that at least one of the ancient burials would have contained grave goods of fine quality (Figs. 9.55, 9.56 and 9.57). Diagnostic



**Fig. 9.55** Mycenaean stirrup jar sherds found in association with human remains in Locus 121, Square 6/19 (Photo – T.E. Levy, Center for Cyber-Archaeology and Sustainability, UC San Diego)

**Fig. 9.56** Psi-figurine found in association with human remains in Locus 121, Square 6/19 (Photo – T.E. Levy, Center for Cyber-Archaeology and Sustainability, UC San Diego)



**Fig. 9.57** Gold fragment (crumpled foil) found from sieve of Locus 121, Square 6/19 (Photo – T.E. Levy, Center for Cyber-Archaeology and Sustainability, UC San Diego)



figurines and Mycenaean stirrup jar fragments, along with the tomb architecture, also suggest that the tomb was Mycenaean/Late Helladic in date, though verification of this and increasing the precision of the dating depend on subsequent typological and scientific dating (Liritzis et al. 2016).

### **Square 7/19: Investigation of Geophysical Survey Results (Ground Truth)**

#### Stratum I

Square 7/19 was opened to the immediate east of the tomb excavation with the primary goal of exploring a possible subsurface void in the area detected by geophysical survey (by Grigoris Tsokas and his team). Only the southern half of the square was opened for excavation due to the time constraints of the short season (Figs. 9.58, 9.59 and 9.60). In this square, only Locus 106 and Locus 113 were assigned to Stratum I because they were primarily topsoil (Figs. 9.58 and 9.59). Excavation began in the southwest corner of the square with Locus 106 which was dedicated to excavating the topsoil in this area of the square. The locus was excavated quickly with large picks, and collected material culture consisted mostly of pottery. The top of a large stone was also discovered, but its edges were not fully delineated (it is unclear if this was simply a large stone or a bedrock outcropping). Locus 106 was closed in order to expand excavations to the east (Locus 113, still within the southern half of the square). Locus 113 was a roughly 0.5 m × 3.5 m trench opened to expand excavation across the east-west length of the square. During excavation, 1–2 rows of ca. 5 stones were discovered resembling a possible wall, and at this time Locus 113 was extended an additional 0.5 m to the immediate south. Excavation in this newly expanded portion of locus revealed a continuation to these stones, and it also appeared that this possible wall continued outside the square to the southwest. To the east of the wall feature, excavation in Locus 113 also discovered a possible fire pit feature (Locus 115). With this discovery and the presence of the wall feature



**Fig. 9.58** Locus 106 – excavating topsoil in southwestern corner of Square 7/19 (Photo – T.E. Levy, Center for Cyber-Archaeology and Sustainability, UC San Diego)

**Fig. 9.59** Locus 113 – expanded excavations in Square 7/19 to the east (Photo – T.E. Levy, Center for Cyber-Archaeology and Sustainability, UC San Diego)



### Final Top Plan of Excavated Square 7/19, Kastrouli (July 30, 2016)

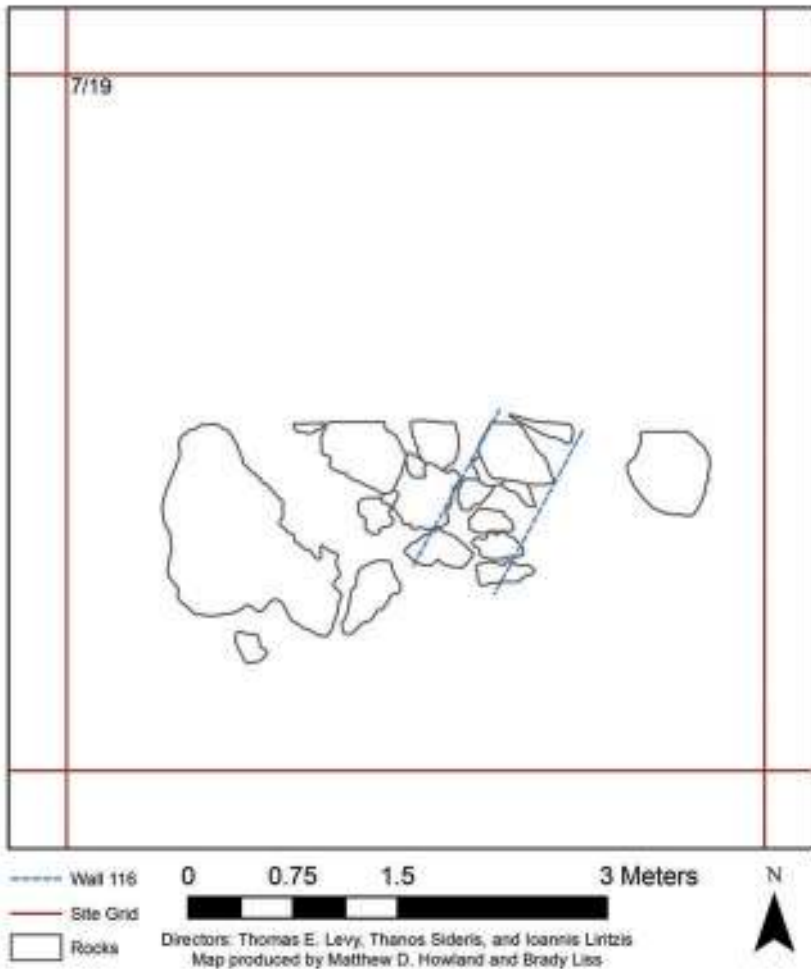


**Fig. 9.60** Final top plan from the last day of excavation in Square 7/19 at Kastrouli

(Locus 116), Locus 113 was closed. Material culture collected from the locus included mostly pottery and a highly fired loom weight.

#### Stratum II

In Square 7/19, Loci 114, 115, 116, and 117 were assigned to Stratum II (Figs. 9.61, 9.62, 9.63 and 9.64). These loci were attributed to Stratum II based on their assumed later date than the tomb, but their undisturbed contexts would be inappropriate to



**Fig. 9.61** Locus 114 – excavating to the east of Wall 116, possible structure interior in Square 7/19 (Photo – T.E. Levy, Center for Cyber-Archaeology and Sustainability, UC San Diego)



**Fig. 9.62** Locus 115 – excavation of possible fire pit feature in Square 7/19 (Photo – T.E. Levy, Center for Cyber-Archaeology and Sustainability, UC San Diego)

include in Stratum I. Locus 116 represents the wall feature described above which included 1–2 rows and 1–2 courses of unworked stones. Locus 115 (Fig. 9.62) encompassed the fire pit feature (to the east of Wall 116) based on the presence of dark, ashy sediment and unique, possibly worked stones. Locus 114 (Fig. 9.61) was opened in the immediate area around the burn feature and up to Wall 116. The area to the west of Wall 116 (and below Locus 106) was assigned Locus 117. Excavation focused in Locus 115 where some in situ pottery was collected (a possible cup



**Fig. 9.63** Locus 116 – Wall feature in Square 7/19 (Photo – T.E. Levy, Center for Cyber-Archaeology and Sustainability, UC San Diego)



**Fig. 9.64** Locus 117 – excavating to the west of Wall 116 in Square 7/19 (Photo – T.E. Levy, Center for Cyber-Archaeology and Sustainability, UC San Diego)

base – Basket 20,079) and the possible worked stones around the fire pit feature were excavated (Basket 20,086–20,088). These stones also appeared to be fire cracked reiterating the possible presence of significant heat (the over-fired loom weight from Locus 113 also supports this understanding). Locus 115 was closed with the bottom of the ashy sediment, at which time Locus 114 was excavated to a similar elevation. Locus 114 was closed once level with Locus 115. The excavations in Locus 117 west of the wall continued until the closing of the square, but it was

unable to delineate the large stone originally discovered in Locus 106. The square and all associated loci were closed on 29 July in order to focus all excavations within the tomb. The square was covered with a thick plastic sheet and backfilled for protection during the off-season.

### Interpretation

Despite the limited excavation in Square 7/19, it is possible that the wall and interior of a structure were partially excavated (Figs. 9.63 and 9.64). While only a small part of the wall (Locus 116) was excavated, it appeared to be in line with several large stones to the southwest of the square suggesting both the wall and possible structure continued in that direction. Loci excavated to the immediate east of the wall were consistent with a possible habitation or activity area, i.e., the interior of the structure. Locus 115 yielded a potential fire pit, and the in situ pottery and loom weight from Loci 115 and 113, respectively, reiterate the possibility of an activity area. In contrast, excavations to the immediate west of Wall 116 in Locus 117 only discovered some pottery and the presence of a large stone or bedrock outcrop; perhaps this area represents the exterior of the structure. However, due to the limited size of the excavation in Square 7/19, these conclusions remain highly speculative but should be further pursued in the future.

## *Fortification Wall Section Excavations*

### **Squares 5/21 and 5/22**

#### Stratum II

The two wall section excavations (Squares 5/21 and 5/22 and Square 21/2) attempted to discover the founding levels of the fortification wall that surrounds the site to facilitate its dating (Figs. 9.65 and 9.66). Both wall section excavations (Loci 103, 105, and 118) were attributed to Stratum II based on the hypothesis that the wall postdates the tomb. The excavation in Squares 5/21 and 5/22 focused on a northwest section of the wall where there appeared to be two phases of construction. The earlier phase consisted of 2–3 courses of large, unhewn stones (50+ centimeters in diameter), while the later phase was constructed of smaller field stones of 5–6 courses (using the earlier wall as a foundation). It was assumed that the earlier, larger construction can be attributed to the Mycenaean occupation at the site and excavations intended to address this hypothesis. Excavation focused on the exterior side of the wall where much of its construction was visible. Two loci were opened during excavation: Wall Collapse Locus 103 and Fill Locus 105. Locus 103 was dedicated only to removing the wall collapse (no excavation or material culture collected), and it was immediately closed once all stones were cleared. Locus 105 was

**Fig. 9.65** Locus 103  
(removing wall collapse at  
northwest wall section  
excavation) and Locus 105  
(excavating fill at  
northwestern wall section  
(Photo – T.E. Levy, Center  
for Cyber-Archaeology  
and Sustainability, UC San  
Diego)



**Fig. 9.66** Locus 118 –  
excavating southern wall  
section in Square 21/2  
(Photo – T.E. Levy, Center  
for Cyber-Archaeology  
and Sustainability, UC San  
Diego)



dedicated to excavating the fill abutting the wall to reveal its lowest courses. The locus revealed one additional course of large stones before discovering its foundations directly on the local bedrock. In addition, pottery was discovered within the bottom course of the wall (Basket 20,008), thus providing a secure dating method for its construction. After the bedrock foundation was discovered, Locus 105 was closed with all excavation in this area. For future analysis, samples for optically stimulated luminescence (OSL) were collected by Ioannis Liritzis to date the construction of the wall.

## **Square 21/2**

### **Stratum II**

Excavation in Square 21/2 occurred on the exterior edge of the fortification wall at the southern end of the site and was assigned Locus 118 (Stratum II). The goal of the locus was to discover the founding levels of the site's fortification wall to facilitate its dating. Excavation in this area uncovered stones likely collapsed from the wall embedded in a fine grayish brown fill. These presumably collapsed stones were not removed with excavation. As with the wall section excavated in the northwest, the wall was discovered to be constructed directly on bedrock, which was exposed at the western edge of the locus. The exposed wall consists of five courses of large (ca. 50 cm diameter) stones, with smaller stones placed into the gaps between the large stones. This wall appears to have been constructed in one phase. Excavation did not continue in this area, and Locus 118 was closed following the exposing of bedrock in the western edge of the locus. As with the northwestern wall section, samples for OSL were collected by Ioannis Liritzis to date the construction of the wall.

### **Interpretation**

The excavations at each wall section achieved the goal of discovering the founding levels of the site's fortification wall. In both cases, the wall constructed of large stones was constructed directly on the local bedrock. Post-excavation analysis will be critical in facilitating the dating of the walls. Both the ceramic typology from the pottery collected from Locus 105 and the OSL analysis will be critical in this investigation.

## ***Summary***

The 2016 excavation at Kastrouli was successful in achieving the goals of its research design. The exposed tomb in Area A was fully and systematically excavated down to its bedrock surface. All remaining material culture and human

remains (following the looting and previous excavations) were excavated and will be critical in interpreting and dating the tomb. At the moment, based on the typology of the ceramics and stratigraphy of the site, the comingled burial represents a use span from ca. 1300 to 1150 BC. In addition, the site's large fortification wall was sectioned in two areas finding the foundations of its construction directly on the local bedrock. These excavations facilitated the collections of OSL samples which will be essential in providing an absolute date for the construction of the wall.

### **Contextualizing the Mycenaean Coastal World: 3D Documentation of Steno and the Potami Bays**

In order to contextualize the interface between the land and sea in this Mycenaean coastal world, the Kastrouli–Antikyra Project captured a portion of the local coastline in 3D using terrestrial and aerial photography methods. The 3D documentation focused on the Potami Bays and the Mycenaean Steno archaeological site (described further below). Steno's unique position atop a rocky outcrop just off the coast provides an ideal vantage point over the Potami Bays suggesting it was an integral component of the coastal world (Figs. 9.67, 9.68 and 9.69). Using the balloon and CAVEcam systems described above, two team members recorded the site and bays over the course of a few hours. The balloon was used for one flight focusing on Steno to produce a 3D model of the site and its extreme topography (Fig. 9.67). The aerial photography was also used to create an orthophoto for future site mapping or other GIS analyses (Fig. 9.68). The CAVEcam was positioned in three locations along the coast of the bays for stereo photography of the entire feature – once in each smaller bay (Potami and Sotira) and once on the small peninsula separating them. An additional panorama was taken from atop Steno to capture the site and its perspective of the coast/bays (Fig. 9.69). Together, these datasets provide a complete digital record of Steno and Potami Bays.

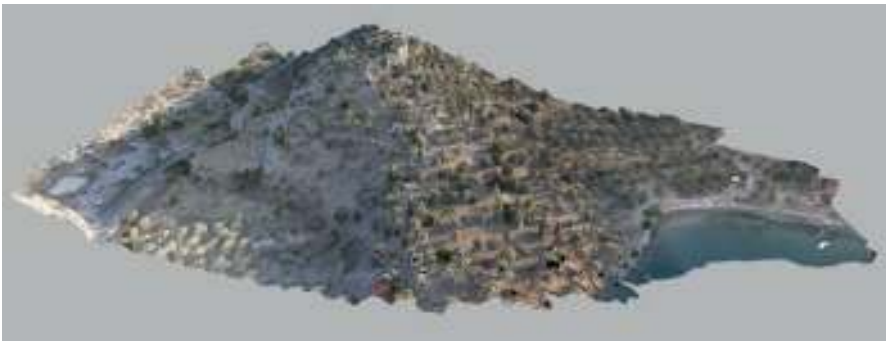


**Fig. 9.67** Screenshot of Steno 3D model in Agisoft software created from balloon photography

**Fig. 9.68** Orthophoto of Steno created from balloon photography



**Fig. 9.69** The 360 degree panorama from the top of Steno with views of the Potami Bays (Captured with the CAVEcam)

## **Marine Remote Sensing: The Mycenaean Coastal World (from Kastrouli to the Antikyra Bay)**

### ***Introduction***

In the Antikyra Bay project, we have taken up Thomas Tartaron's (2013) challenge to identify and work up a methodology for the investigation of ancient Mycenaean coastal worlds – the local land and sea interfaces of the Late Bronze Age Aegean. This report describes the fieldwork of a marine remote sensing survey, which was carried out in the coastal zone of Antikyra Bay, Central Gulf of Corinth, in Greece. The survey was planned and carried out between 4th and 9th of August 2016, by the Laboratory of Marine Geology and Physical Oceanography of the University of Patras in cooperation with the University of California, San Diego, under the direction of Prof. Thomas Levy.

The Antikyra marine remote sensing survey is an ongoing research project designed:

- To define the sub-bottom stratigraphy of the recent sediment sequence
- To illustrate the seabed morphology of the survey area
- To collect long (up to 6 m) sediment cores in specific locations based on the results of the marine remote sensing survey
- Besides the selection of the sediment cores, the project aimed:
- To define the evolution of the coastline configuration of the Antikyra Bay over the last 18,000 yrs. BP based on the seismic stratigraphy and the mapping of possible paleo-shoreline features
- To detect targets (surface and subsurface) of potential archaeological interest

### ***Fieldwork***

Field activities in the Antikyra Bay during August 2016 survey period included:

- Mapping of the morphology of the seafloor
- Study of the seabed seismic stratigraphy
- Sediment core sampling

The marine remote sensing survey was carried out using a Kongsberg GeoPulse Plus (GeoAcoustics Universal) chirp sub-bottom profiler system and an EG and G side-scan sonar. A Hemisphere V100 GPS system with accuracy of approximately 1.5 m was used for the navigation and the positioning.

In order to meet the objectives of the survey, a 16 m-long wooden vessel (MY LORD, MY LADY) was used (Fig. 9.70). The vessel had been suitably modified to meet the specific needs for the remote sensing survey and the sediment sampling (Fig. 9.71).



**Fig. 9.70** My Lord, My Lady research vessel from the University of Patras used for coring expedition in the Antikyra Bay, Gulf of Corinth, Greece, 2016 expedition (Photo courtesy G. Papatheodorou, University of Patras)



**Fig. 9.71** The vessel “MY LORD, MY LADY” which was used for the remote sensing survey and the sediment sampling, equipped with (a) the sub-bottom profiler (over the side), (b) the side-scan sonar, (c) acquisition unit, and (d) sampling devices (Photo courtesy G. Papatheodorou, University of Patras)

### Side-Scan Sonar Survey

The side-scan sonar survey aimed at (i) the mapping of the geomorphological and textural features of the seafloor and (ii) the detection and positioning of targets which may represent man-made features. The side-scan sonar system emits acoustic pulses providing a plan view seafloor acoustic image. The main advantage of a side-scan sonar system is the ability to survey wide seafloor areas at a greater “over the ground” speed. The side-scan sonar system consists of:

- A dual frequency (100 and 500 kHz) towfish 272TD (Fig. 9.72)
- Kevlar cables 50, 150, and 200 m
- Digital recording unit Edgetech 4100P topside (Fig. 9.73)

Over 40 side-scan sonar lines having a length of 40 km and covering a total area of about 2 km<sup>2</sup> were surveyed in the coastal zone of Antikyra at water depths



**Fig. 9.72** Dual frequency towfish 272TD with the Kevlar-type cable



**Fig. 9.73** The digital recording unit Edgetech 4100P topside (Photo courtesy G. Papatheodorou, University of Patras)



**Fig. 9.74** Map of the surveyed areas showing the tracklines of the side-scan sonar and sub-bottom profiling. From right to left – Ag. Isidoros, Potami/Ag. Sotirios, and Valtos (Photo courtesy G. Papatheodorou, University of Patras)

between 3 and 30 m (Fig. 9.74). The side-scan sonar lines were running almost parallel and perpendicular to the central axis of the three small coves, Ag. Isidoros, Potami/Ag. Sotirios, and Valtos up to 30 m water depth (Fig. 9.74). The side-scan sonar survey of the abovementioned areas was carried out with range of 50–100 m each side with the 100 and 500 kHz frequency, in order to achieve the best resolution of the side-scan sonar system. The line spacing was such that the seafloor area covered between two lines was overlapped by 50%.

The excellent quality of the acquired side-scan sonar raw data will provide important information regarding the morphology of the seafloor (Figs. 9.75 and 9.76) and possible man-made targets lying on the seafloor.

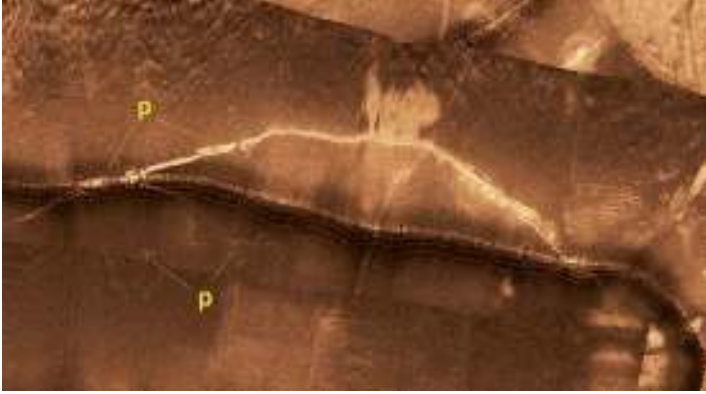


**Fig. 9.75** High-resolution side-scan sonar mosaic showing submerged paleo-shorelines (p) in Ag. Isidoros cove. *Light-tone area represents hard substrate and low-tone area seafloor covered by fine-grained sediments* (Photo courtesy G. Papatheodorou, University of Patras)



**Fig. 9.76** High-resolution side-scan sonar mosaic showing Collagen formations (c) (small reefs) on the seafloor (Photo courtesy G. Papatheodorou, University of Patras)

### Sub-Bottom Profiling Survey

The sub-bottom profiling survey at Antikyra Bay was carried out using a chirp sub-bottom profiler. A Kongsberg GeoPulse Plus (GeoAcoustics Universal) chirp sub-bottom profiler system has been used for the examination of the upper (<30 m) seismic stratigraphy of the seabed. The system can operate using various signal waveforms, but for optimum performance a chirp signal with frequency ranges between 1.5 and 11.5 kHz has been used, providing high-penetration, high-resolution data. The penetration of the system can reach up to 80 m in loose sediments, and its resolution is less than 10 cm.

The sub-bottom profiler system emits medium to high frequency acoustic pulse in the form of acoustic conical beams providing a geological profile (seismic profile) of the sub-bottom beneath the path over which the system is towed.

The GeoPulse Plus chirp sub-bottom profiler consists of:

- An over-the-side Transducer Mounting and the trailing single-channel hydrophone (Fig. 9.77)
- The Universal Transceiver (Fig. 9.77)



**Fig. 9.77** (a, b) O.R.E. Model 132A/132B over-the-side Transducer Mounting (c) Universal Transceiver of the chirp system and (d) a chirp seismic profile collected from the surveyed area (Photo courtesy G. Papatheodorou, University of Patras)

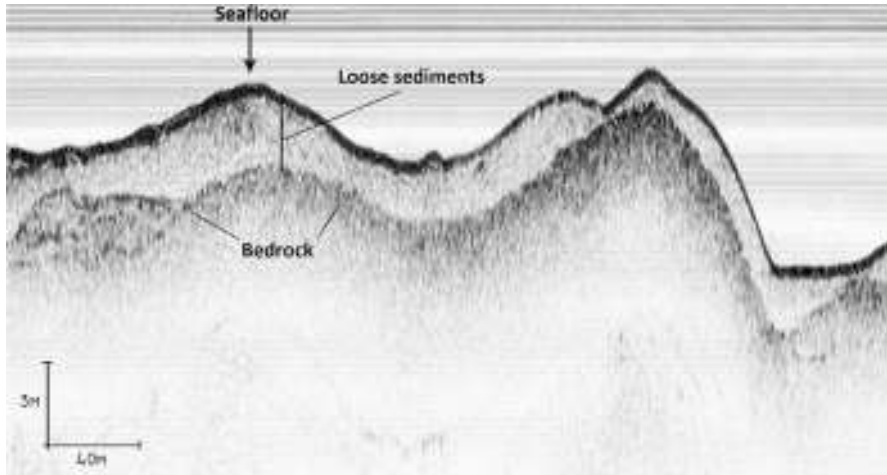


**Fig. 9.78** High-resolution chirp seismic profile showing surface loose sediments, 3 m in thickness, overlying the bedrock (Photo courtesy G. Papatheodorou, University of Patras)

- Data acquisition was achieved through Sonarwiz (Chesapeake Technology Inc.) software (Fig. 9.77).

Over 40 chirp sub-bottom profiler lines having a total length of 40 km were surveyed. Additionally, for the reconstruction of the paleogeography and the detection of submerged paleo-shorelines, sub-bottom profiler lines were acquired parallel and almost perpendicular to the shoreline of the surveyed coves (Fig. 9.74).

A time base (TB) of 0.10 sec and a 0.1 msec pulse was used for the sub-bottom profiling survey in the area. The vertical resolution of the system was about 10 cm. The collected chirp raw data is of excellent quality and allows the identification of the stratigraphy of the seafloor of the survey area (Fig. 9.78).

### *Sediment Core Sampling*

A 6 m long corer has been used to collect sediment core samples from the seabed. Richard Norris (Scripps Institution of Oceanography) and Thomas Levy (University of California, San Diego) and students Rishi Sugla and Thomas Holm were responsible for the operation of the corer and the collection of the sediment cores. The sampling positions were chosen after the completion of the geophysical survey and on the basis of the high-resolution chirp seismic profiles. In total nine (9) sediment cores were collected from the three coves, two (2) from Valtos, six (6) from Potami/Ag. Sotirios, and one (1) from Ag. Isidoros (Table 9.4). Table 9.4 presents the geographical coordinates of the collected sediment cores and the thickness of the loose surface sediments above the bedrock at the sampling sites (chirp data).

**Table 9.4** Coring sites with coordinates and sediment thickness in study area

| Core site        | X (latitude)   | Y (longitude)  | Sediment thickness (m) |
|------------------|----------------|----------------|------------------------|
| Valtos 1         | 38° 21' 02.06" | 22° 35' 57.70" | 2.5                    |
| Valtos 2         | 38° 21' 03.18" | 22° 35' 57.08" | 2.5                    |
| Potami 1 and 3   | 38° 21' 29.91" | 22° 36' 16.10" | 3.6                    |
| Potami 2 and 4   | 38° 21' 28.05" | 22° 36' 09.97" | 2.9                    |
| Agios Sotirios 1 | 38° 21' 30.68" | 22° 36' 23.31" | 3                      |
| Agios Sotirios 2 | 38° 21' 29.68" | 22° 36' 20.96" | 2.6                    |
| Agios Isidoros   | 38° 21' 38.30" | 22° 37' 16.17" | 2.3                    |



**Fig. 9.79** Map of the surveyed areas showing the sediment cores sites (Photo courtesy G. Papatheodorou, University of Patras)

### Sediment Core Extraction and Preliminary Study

Sediment cores were collected in four small bays within the larger Antikyra Bay: these include (from west to east) Valtos, Potami, Sotirios, and Agios Isodoros in the Gulf of Corinth (Fig. 9.79). These smaller bays and inlets are characterized by pebble beaches that were and still are used as small harbors for fishing, aqua farming, and recreation. As pointed out by Sideris (2014:176–177), the four small bays studied here can be characterized as follows (from west to east): *Valtos* – is exposed to southern and western winds. No archaeological remains have been found here, but there is a freshwater stream on to NW side of the bay. Only modern occupation

evidence is known for this small bay; Potami – there are two small bays here, and they are exposed only to southern winds. Potami has a spring emerging on the beach and a partially filled wetland on the north side of the bay. The area took its name (Greek for “rivers”) from the network of small springs that are found less than a hundred meters from the shore. The small western bay is referred to as “Potami,” which is where our team carried out most of its coring activities. There is no evidence of antiquities along the Potami shore – only modern occupation linked to a tavern and fish farm. However, the two small Potami bays here (Potami and Sotira) are separated by a small inlet and promontory called Steno that has multiple ancient occupations including from the Mycenaean period. As Steno is situated on a rugged and naturally defended chersonese, it would be an excellent defensive platform for the Potami bays. To the east of Steno is the other tiny gulf in Potami called Sotira bay. Further east, Agios Isidoros is the last bay sampled by our team. On its western side, there is larger beach, with a smaller one on the east. While the larger beach has little shelter, the smaller one is well protected from wind. Along the southern coast of the Agios Isidoros bay is the promontory site of Vroulia where numerous Mycenaean sherds have been collected. There is a small modern marina near Agios Isidoros’s eastern beach where our team docked the research vessel each evening during the expedition. There is little question that the Antikyra Bay area rather than the Itsea Bay provisioned Kastrouli during the Mycenaean occupation. From a topographic perspective, there are no easily accessible valleys that lead from Kastrouli down to the west and the Itsea Bay. On the other hand, almost due south of Kastrouli is gentle topography that leads directly to the Antikyra Bay. The modern road that leads from Kastrouli to the town of Antikyra follows most of this route. The location of the small Potami bays fed by freshwater streams and dominated by the Steno Mycenaean small fort led us to focus the “sea” portion of our Kastrouli–Antikyra Bay project here.

Sediment coring was achieved by the use of a hammer core system operated by a UC San Diego scuba diver team of four individuals, all trained as science divers (Fig. 9.80) and one professional Greek diver (Fig. 9.80 coring underwater). Cores were collected with 6 m length of agricultural supply pipe, 10.2 centimeters in diameter. These core barrels were fitted with stainless steel cutters, and core catchers riveted into place designed and manufactured at the Scripps Institution of Oceanography by Prof. Richard Norris. The cores were driven into the seabed by the use of a stainless steel sliding hammer that seated onto a set of adjustable handles that could be moved along the length of the core barrel as the core penetrated the bottom. Cores were extracted from the bottom by the use of a shipboard boat winch and inflated lift bag. Oxygen refills for scuba tanks were kindly provided by a local fish farm situated in the Potami Bay.

Visual observations of the split cores were combined with core-scanning XRF measurements of major and minor element sediment chemistry. In the Potami Bay, 2–3 m cores typically have an upper 70–100 cm interval of red-brown clayey silt in the core top, overlying 1–2 m of green shelly sand (see Fig. 9.81). The sand is rich in molluscs and often the roots of *Posidonia* seagrasses and sometimes contains fragments of wood and probably charcoal. Thin interbeds of red-brown silty sedi-



**Fig. 9.80** Thomas Levy using hammer core system in Potami Bay. The hammer has two handles on the hammer, which is raised by the diver and released to hammer down the core barrel (Photo – Richard Norris, Scripps Institution of Oceanography, UC San Diego)

ment occur within the green shelly sand and are typically 10–20 cm thick. Potami Core 1 (Fig. 9.81) contains a layer about 30 cm thick at the bottom of the core of this red-brown silty sediment. Interbeds almost always have bioturbated boundaries with adjacent layers. We interpret the green shelly sand to represent the normal marine accumulation in the bay. This sediment tends to be coarser grained and has a higher percentage of pebble sand fine gravel in places within the bay that are exposed to the wind and bottom currents. The green shelly sand often contains molluscs such as small bivalves and *Dentalium* that are in life position, suggesting that the sediment is not substantially reworked. The abundance of shell in the sediment is shown by elevated Sr/Ca ratios, reflecting strontium-rich aragonitic mollusc shells.

In contrast, the red-brown clayey silt is much finer grained and has higher K/Fe ratios in XRF records than the green shelly sand (Fig. 9.81). This chemistry is consistent with the clayey silt (high in potassium) as being derived from eroded soils, particularly the terra rosa soils typically developed on carbonate bedrock in the area. The K/Fe ratios are consistent with the records of other lithogenic elements such as Fe, Ti, Ba, Si, and Zr. Therefore, we interpret the record to indicate a shift in recent times (representing the core top) toward soil loss from upland areas. The existence of multiple layers of red-brown clayey silt in most of our Potami Bay cores suggests that the delivery of eroded soil occurred throughout the depositional record represented by our cores and was interspersed with periods of marine sedimentation of additional shelly green sand.

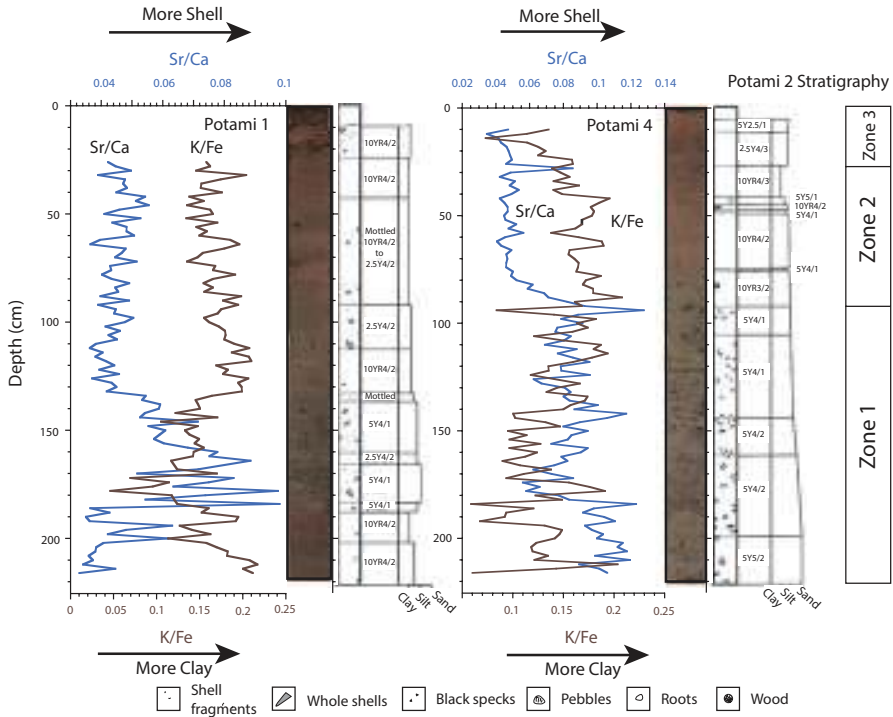


**Fig. 9.81** Potami 4 Core (right) and Potami 1 core (left), showing the K/Fe ratio (brown line) and Sr/Ca ratio (blue line) against the core images and core drawings. A drawing is not available for Potami 4, so we show the stratigraphy of Potami 2 (taken within a few meters of the site of Potami 4) for comparison. The K/Fe record reflects clay abundance, with generally higher amounts of clay in the red-brown intervals of the cores. Increases in the Sr/Ca ratio are associated with the shelly green sands suggesting elevated abundance of marine aragonitic shells relative to the red-brown sediment layers. Note the upward increase in abundance of clay-rich sediment, likely reflecting erosion of terra rosa soils from nearby limestone slopes. Similar increased delivery of soil toward the tops of our core records is seen in the other cores collected during the Antikyra coring program consistent with a regional increase in soil erosion in recent times. However, we await dating the cores before we can evaluate the rate and timing of local soil erosion in the area. (Courtesy of R. Norris and I. Rivera-Collazo, as we both contributed to the graph).

During coring operations, we drove the cores into the seabed until they would no longer penetrate further. The core penetration depths (~2–2.5 m) were broadly in agreement with the expected sediment thicknesses obtained from geophysical records derived from a sub-bottom profiler system (see marine geophysics section above). Hence, we expect that our cores have captured the entire recent (late Holocene) record of sedimentation in Potami Bay. The bay is surrounded by exposures of well-cemented pebble and cobble conglomerates associated with alluvial fans of Pleistocene age. Although the start date for sedimentation in our cores has not yet been established, it is almost certainly from no older than early to middle Holocene, after sea level stabilized near its current position.

## Geomorphological Implications of the Cores

The preliminary assessment of Potami 1 and 2 provides an initial understanding of the local land and sea conditions. The final interpretation of all cores requires additional laboratory analyses, including high-resolution absolute dating. The sedimentary sequence of both cores accumulated in the marine environment. No in situ paleosols are evident in the record. XRF analysis was performed to Potami 4, but sedimentary assessment was done to Potami 2. These two cores were obtained from the same location, and it is therefore possible to compare the results, but it is also evident that the records are not precisely equal. Additional analyses will be performed to improve understanding of the sedimentary sequences of the basin.

Potami 1 (Fig. 9.81) presents a fine-grained sequence, suggesting a low-energy environment, possibly influenced by the local wetland. The deepest section (Zone 1) records the accumulation of terrigenous sediments, including terra rosa soils. This suggests slope instability and inland erosion. This sequence of reddish clayey silts fines upward to silty clay suggesting even more intense soil erosion. The smaller grain size content, which is yet to be analytically measured, suggests that the erosion could have reached deeper soil horizons, indicating possible intensification of deforestation. This sequence was only briefly interrupted by what seems to be a slight stabilization that also presents increased Sr/Ca ratio and coincides with a stratigraphic break in deposition between ~185-135 cm depth. This short break suggests possible forest recovery or decreased soil erosion, combined with stabilization of the marine environment.

Zone 1 is followed by a coarser sequence of gray sandy silts with high shell content in growth position (Zone 2). The contact with Zone 1 presents the lowest levels of K/Fe of the entire deposit, suggesting a dramatic change in the characteristics of the sediments transported to the embayment. It suggests that erosion decreased dramatically, possibly to the extent that the water column was clear of suspended sediments, fostering a thriving marine environment, as suggested by the in situ mollusc shells. This change could have been caused by reduced precipitation, by stabilization of forests or a combination of both. While more analyses are needed, we are inclined to link this shift to forest recovery, but this still needs to be tested. The uniformity of the deposit suggests that, overall, erosion of soils into the basin dramatically decreased, particularly during the deepest section of this zone. The upper section, between ca. 130 and 160 cm in depth, presents a slightly finer sequence, which coincides with a return to lower Sr/Ca and higher K/Fe readings. While these measures are not as high as those in Zone 1, it is possible that slope soils were again starting to be exposed or available for erosion, but their input to the basin was not significant enough as to cause evident impact. It is possible that sediment suspension was still low. This section is topped off by a mottled layer of grayish and reddish sediments, suggesting mixing and instability.

Zone 3 presents a fining-up sequence that coarsens in the upper 15 cm of the core. In the lower section of the Zone, at the contact with the mottled layer capping Zone 2, the sequence presents reddish clayey silt indicating a return to the erosional conditions that were dominant in Zone 1. K/Fe readings are not as high as before,

suggesting that, while the color represents erosion of fresh terra rosa soils, it might not have been as intense as before, or the soils were more immature. The drastic reduction in shell content, together with the very low Sr/Ca readings, indicates that this return to soil erosion on land affected the marine environment, possibly due to suspended sediments in the water column and high mud deposition rates. Sedimentologically, erosional conditions seem to have stabilized slightly, as indicated by a return to grayish sediments and in situ shells between ca. 85 and 105 cm. However, the XRF results suggest that, in contrast with Zone 2, this decrease in terra rosa input was not absolute, as terrigenous sediments continued to be accumulated. A mottled sequence with finer silty clay and a decrease in shell content indicates instability and mixing of the depositional environment, topped by a reddish layer that continues to the present.

Even though located in the same basin, Potami 2/4 presents a very different sedimentary sequence to Potami 1. The first observation is that the sequence is significantly coarser. This makes sense in the context of the geographical location of the sample, near the head of a rocky coastal foreland. Potami 2 begins with coarse to very coarse sands and pebbles with silt inclusions and fines upward to a silty clay layer in Zone 3. The presence of angular and subangular pebbles and grains suggests the local provenience of the sediments, which could not have been transported in long distances. It is possible that the sediment source is the rocky foreland itself, therefore constituting an immediately local record of land conditions.

Zone 1, the deepest section, presents a marine deposit with thick and stable *Posidonia* seagrass ecosystems, evidenced by often dense root systems. Soil input to this sequence was minimal, although the XRF results suggest that terra rosa input could have increased irregularly in the upper section of the zone. Overall, Zone 1 fines upward from very coarse sand to sandy silt. These characteristics suggest overall clear water column and stability of the soils on the slopes immediately around the core collection point. The fining-upward sequence suggests deepening water, possibly indicating increasing sea level.

Zone 1 in Potami 2 core was drastically interrupted by Zone 2, as evidenced by a sharp contact between the layers and sudden color change to reddish brown. This sequence is a reddish deposit of sandy silt that fines upward to silty clay. Potami 4, in contrast, shows a gradational contact between the shelly sand and overlying red-brown clay-rich sediment. While Potami 4 seems to present a fairly uniform sequence. Potami 2 presents a series of gray laminations at 60 cm and again between ca. 35 and 45 cm, which need to be further explored. Zone 2 suggests the sudden exposure of soils to erosion into the basin. The disappearance of *Posidonia* grasses from the sequence and the identification of a well-preserved wood fragment suggest forest clearance and strongly point toward human intervention.

Zone 3, the uppermost deposit, presents a return to slightly coarser sediments (sandy silt). While color is not dramatically different between Zones 3 and 2, the XRF results suggest a significant change in the mineral composition of the transported sediments, which deserves further exploration. It is possible that this change reflects a change in the availability of soils for erosion and transport in the recent past, very near the present.

Absolute dating and additional high-resolution analyses are still required to be able to interpret these results and the relationship in the sedimentary sequences of Potami 1 and Potami 2/4. A cursory assessment suggests that Zone 2 of Potami 1 and Zone 1 of Potami 2/4 might be related, indicating that the deeper sequence of Potami 1 might correspond to an early human intervention in the Potami basin, followed by abandonment and forest recovery, which is evidenced as decreased fine-grained terrigenous sediment input in the basin. Zone 3 of Potami 1 might correspond to Zone 2 of Potami 2/4, indicating a return to intensive intervention with local soils that continues to the present. Zone 3 of Potami 2/4, which suggests a change in terrigenous sediment erosion to the basin, might correspond to the uppermost section of Potami 1 Zone 3 and relate to changes in settlement patterns or population destabilization as recently as the twentieth century or possibly at the end of the Late Bronze Age (cf. Knapp and Manning 2016). Absolute dating of the cores should resolve this issue.

### **Summary Remarks on the Sediment Cores and Bays**

The next step in the analyses will be to extract suitable samples from the cores for radiocarbon or uranium–thorium (U-Th) dating to finalize the chronological history of sediment deposition in Valtos, Potami, Sotirios, and Agios Isodoros bays. U-Th dating may provide the most accurate method of dating the cores from this project. In a recent study by Cramer et al. (2017), U-Th dating of Caribbean reefs provided a high-resolution chronology to monitor changes in fish, coral, and urchin composition and reef accretion rates over a 3000 year period. Working with lake sediments in Macedonia using novel isotopic proxies that track soil erosion and development, Athony Dosseto (personal communication) found an unprecedented erosion event beginning at ca 3500 yr. BP (and culminating at 2500 yr. BP) that would encompass the Late Bronze Age collapse in the Aegean region. These are the kinds of exciting new developments in dating techniques and sedimentology research that will provide new research directions for examining the marine cores collected during the Kastrouli–Antikyra expedition. These methods may provide the kind of temporal resolution needed to link the geomorphological and environmental record revealed in the cores with the settlement history of this part of ancient Phokis during the Late Bronze Age when a number of Mycenaean sites were established along the northern coast of Antikyra Bay (cf. Sideris 2014). The small bays studied here on the northern shore of the Gulf of Corinth have two Mycenaean sites in close proximity.

### **Conclusion**

The Kastrouli–Antikyra Bay Land and Sea Project near Greece’s Gulf of Corinth was inspired by a number of interwoven research goals including: (a) applying a range of cyber-archaeology and geophysical tools to address the issue of at-risk

cultural heritage in the eastern Mediterranean; (b) using this study to help develop a marine archaeology methodology suitable for studying human coastal adaptation during the late Holocene across time and space; (c) focusing on the end of the Late Bronze Age in the Eastern Mediterranean to address the problem of the collapse of Mycenaean, Hittite, and New Kingdom Egyptian civilizations to investigate the role that climate, environmental, and social factors may have played in this process; and (d) finally to engage in the more local problem of understanding the nature of Mycenaean coastal worlds.

As this is a preliminary study, we do not have definitive answers to the issues raised above. This paper has been more of a methodological treatise on how researchers can integrate an archaeological land and sea project using the tools of cyber-archaeology and marine science. By combining transdisciplinary approaches to cyber and marine archaeology within an anthropological analytical context, we believe important new research horizons will unfold. Where do we stand with the four research goals of the project? The Kastrouli–Antikyra Bay Land and Sea Project successfully addressed the issue of “at-risk world heritage,” one of the major goals of our University of California Office of the President Catalyst Grant. The site of Kastrouli (Fig. 9.2) was selected for investigation because several late Mycenaean tombs were robbed and in a state of deterioration (Raptopoulos 2012), and it is located approximately midway between Delphi where we have been conducting a major digital heritage project (Liritzis et al. 2016; Liritzis et al. in press), and only 5 km from the Antikyra Bay providing an ideal “land and sea” study area. As Kastrouli had never been systematically investigated, to adequately record the damaged tombs, we used the tools of cyber-archaeology to establish a state-of-the-art research infrastructure based on digital data capture, curation, analyses, and dissemination. As shown above, this included beginning with the establishment of a 3D photogrammetric network of trigonometric points at Kastrouli under the direction of Prof. Andreas Georgopoulos of the National Technical University of Athens (Fig. 9.4). This was followed by mapping the site using SfM aerial photography using a helium balloon system (Fig. 9.37) and georeferenced using the trigonometric network linked to the Greek (Hellenic) Geodetic Reference System. These integrated mapping systems provided the spatial foundation on which the Mycenaean tomb was excavated using the cyber-archaeology fieldwork workflow that includes real-time GIS data recording using *ArchField* (Smith et al. 2015; Smith and Levy 2014; Smith and Levy 2012) and *ArchaeoSTOR*, a web-based geospatial database that archives all the digital data collected in the field and lab (Gidding et al. 2011, 2014). As part of the Catalyst project, to enhance the curation of archaeological field data, *ArchaeoSTOR* has been improved so that the web-based program now feeds field data directly into a permanent archive in the University of California, San Diego Library Digital Collections (<http://library.ucsd.edu/dc/>). Accordingly, the Kastrouli *ArchaeoSTOR* records (and any other excavation) can now be uploaded directly from *ArchaeoSTOR* to the online digital collections (Smith et al. 2017). The full citation for the dataset is Levy, Thomas E; Sideris, Athanasios; Liritzis, Ioannis; Howland, Matthew D; Liss, Brady (2017): Kastrouli Mycenaean

Excavations, Greece 2016. UC San Diego Library Digital Collections. <https://doi.org/10.6075/J0NG4NSV>. It is our contention that the ultimate repository for digital archaeological data should be in a research university's digital library and the 2016 Kastrouli excavation provides a model for how this can be achieved.

Three days prior to the Kastrouli excavation, to identify additional subterranean features associated with Tomb A and other archaeological targets at the site, a series of detailed geophysical surveys were carried out at the site under the direction of Prof. Gregorios N. Tsokas of the Aristotle University of Thessaloniki that included resistivity tomography, magnetic gradiometry, and ground-penetrating radar (GPR). As described above, from a site perspective, numerous potentially significant archaeological features were located across the site on various flat terrace areas using this complement of geophysical techniques. On the smaller scale, in the vicinity of Tomb A, the electrical resistivity tomography results identified an additional subterranean feature linked to Tomb A that ground-truth excavation showed to be a significant addition to the Mycenaean mortuary architecture at the site. For future work at the site, the geophysical survey results described above may help identify important target areas for excavation.

The 2016 excavation of Tomb A at Kastrouli has been published in detail elsewhere (Sideris et al. 2017). The significance of Tomb A can be summarized as follows. It is a hybrid between a rock-cut chamber tomb and the built tomb types with a dromos passage. Based on the ceramic assemblage (Fig. 9.55) made up of numerous Mycenaean stirrup jars and Psi figurines, the tomb must have been constructed at the beginning of the LH (Late Hellenic IIIA 2 or slightly later period). The tomb contained a large number of human comingled human remains found in a carved depression in the limestone bedrock at the eastern extremity of the tomb. In a preliminary study of the human remains, Chovalopoulou et al. (2017) identified a minimum number of 19 individuals (MNI) in the bone pile: 15 adults, 2 subadults, an infant, and a fetus. Domestic animal bones were also found here including bones and/or teeth of *Gallus gallus domesticus* (chicken), *Bos taurus* (domestic cow), *Sus scrofa domesticus* (domesticated pig), and *Ovis aries/Capra hircus* (sheep/goat) (2017:269). As these domestic animal remains were found with the comingled human remains, we suggest that they represent feasting associated with the burial ritual at the site. As shown in the compendium of studies assembled by James Wright (2004) in *The Mycenaean Feast*, the presence of domestic animals related to feasting is common in Late Bronze Age settlement and mortuary contexts. Contemporary with Kastrouli, the Late Helladic IIIA 2 occupation at Tsoungiza at ancient Nemea produced evidence of ceremonial feasting (Dabney et al. 2004). The deposit showed dominance of head and foot bones from MNI 6 cattle, suggesting on-site butchery with possible redistribution for the meat elsewhere (2004:77). Post-mortuary event intrusion by snakes is indicated by a large number of snake vertebrae and different species of gastropod (snail) shells. As Kastrouli is a relatively small isolated Mycenaean site (6 ha), we had assumed it was a relatively poor LH IIIA 2–LH IIIC agricultural site. In addition, based on the SfM mapping of the site and geophysical surveys, there seems to be a cluster of tombs around the north-

western edge of the summit of the site. During the excavation of Tomb A, another mortuary structure was found immediately to the south. Thus, there may be a cemetery in this part of the site providing an ideal locale for investigating the social organization of this LH site. To our surprise, Tomb A with its well-built mortuary structure with large stone slabs and dromos (over 10 m in length), Psi figurines, and gold foil probably associated with prestige goods (textiles, wood?) indicates a much more complex society at Kastrouli than previously assumed. The nature of the complex society at Kastrouli within the Mycenaean “world system” is beyond the scope of this paper.

In terms of Kastrouli’s site size (1.67 ha), it is useful to compare it to settlement patterns in other regions of Greece. In spite of the problems associated with estimates for site size in the region of Messenia (and elsewhere in Greece), Simpson (2014:19) uses provisional categories such as “village,” “hamlet,” and “farm.” Accordingly, Mycenaean sites with LH sherd scatters larger than 1.0 ha (i.e., over 10,000 m<sup>2</sup>) are considered “villages,” 0.5–1.0 ha are classified as “hamlets,” and sites below 0.5 ha are designated “farms.” Settlements that are over 2.5 ha are characterized as “large.” When the habitation area, cemetery, and palace are included, the mega site of Pylos (Davis et al. 1997) is ca. 18 ha in size. While there is a Mycenaean Atlas Project (<http://www.helladic.info/>) that could serve as a platform for coordinating research on ancient site size in a systematic fashion for the whole of Greece and larger Mycenaean world, having the data available in a user friendly Google Earth platform like the Digital Archaeology Atlas of the Holy Land (<https://daahl.ucsd.edu/DA AHL/>) would expedite settlement pattern studies for this key period. Thus, at 1.67 ha in size, it is justifiable to consider Kastrouli as a “small” site. The discovery of a rich burial assemblage at such a seemingly peripheral site suggests a need for further excavation to clarify the nature of the small Mycenaean coastal world (Sherratt 1993) that linked Kastrouli to the Bay of Antikyra and larger Gulf of Corinth during the Late Bronze Age.

As noted above, the Potomoi bay is the most likely candidate for Kastrouli’s maritime access to the larger Mycenaean coastal world. Situated between the Trachilos peninsula in the west and the Pharyngion (Mounta) peninsula in the east (Sidiris 2014:176), the Potami small bays have a number of features that support this hypothesis: (a) extensive pebble beaches suitable for beaching small boats, (b) a number of freshwater springs close to these beaches making the provisioning of boats and human occupation here relatively easy, (c) the natural topography of the drainage system that leads down from Kastrouli to Antikyra but shifts to the west emptying into Potomoi Bay near the Mycenaean site of Steno, and (d) the Steno small fort situated on a promontory overlooking and defending the two small bays of Potami and Sotira. Tartaron (2013:186) has proposed a framework for classifying Mycenaean maritime cultural landscapes that include different spheres of interaction in relation to geographical scale, temporality, operators, typical vessels, some examples of archaeological evidence, and suggestions for typical modes of exchange. The range for local systems to interregional ones includes coastscape, maritime small world, and regional/intracultural maritime spheres to the largest interregional/intercultural maritime spheres. As seen in Fig. 9.3, Steno is one of four

coastal Mycenaean occupations (LH II and III sherds have been found at Antikyra, cf. Sidiris 2014:185) around the Antikyra Bay, and there are numerous Mycenaean sites along the northern coast of the Gulf of Corinth in this region of Phokis (<http://www.helladic.info/>). Thus, the Potami bay and its link to LH III Kastrouli form a coastscape territorial interaction sphere with linkage to the interior as well as a maritime small world that connected many coastscales around the Gulf of Corinth. For the study presented here, we focus on the local Kastrouli–Potami Bay coastscape. This coastscape would have been the scene of everyday interaction where specialist seafarers, craft specialists, farmers, and other nonspecialists would have interacted. Based on Bronze Age archaeological parallels such as the Akrotiri Flotilla Fresco boats (Marinatos 1974; Strasser 2010), the Mitrou boat (Van de Moortel 2009), Cretan seals (Wedde 2000), and boat models, it is possible that fishing boats, pilot boats, and coasting vessels frequented Potami Bay. Home-based and reciprocity exchange would have characterized the inland and coastal maritime interaction. How this Mycenaean maritime cultural landscape system related to sea level rise, the identification of paleo-beaches in our side-scan sonar survey described above, and environmental change will become more clear once the sediment cores described here are carefully dated. Together, the land and sea approach to Mycenaean coastal advocated here can provide a more holistic way of investigating climate, environmental, and social change on a global scale.

**Acknowledgments** The authors would like to thank the Ministry of Culture of Greece for granting permission to excavate at Kastrouli and Mrs. A. Tsaroucha, member and representative of the Ephoreia of Antiquities at Phokis (EAPh) in Delphi, for excellent collaboration. All archaeological works and surveys at Kastrouli were supervised by the EAPh's delegate, Anthoula Tsaroucha, and made possible through the constant support of the EAPh and Nancy Psalti, its director. Thanks also to Dr. Nikolaos Petrochilos of the EAPh for his help and support. We thank also Dr. Fotis Dasios for discussing with us the Sykia chamber tomb and its finds. We are grateful to the villagers of Kastrouli for hosting the 2016 expedition in their homes and tavernas with warmth and good will. The Desfina municipality was very helpful throughout the project, and we are grateful for their help and support of the following: Mr. Babis Kaliakoudas (president of Desfina municipality community) for excellent support prior, during, and after the 2016 fieldwork; Mrs. Panagiota Karamani (conservator) for her assistance; Mrs. Fotini Koukou (the guardian) for excellent cooperation; and Mrs. Alina Levy for her care with logistics and the whole project. At the University of Patras, we would like to thank Nikos Georgiou, MSc, PhD candidate, Laboratory of Marine Geology and Physical Oceanography (LMGPO), Department of Geology; Xenophon Dimas, MSc, PhD candidate, LMGPO; Spyros Sergiou, MSc, PhD candidate, LMGPO; and Nikos Georgioud, professional diver, Patras, Greece. We also appreciate the help of Sophia Margaritis, owner of the Hotel Arimar in Antikyra, which served as our base during the work in that area. For useful suggestions on Aegean archaeology, we warmly thank Eric Cline, Malcolm Weiner, and Assaf Yasur-Landau. Some US graduate student support was provided by the University of California Office of the President through a Research Catalyst Grant for At-Risk Cultural Heritage and the Digital Humanities (Grant ID: CA-16-376911; Lead PI: Thomas Levy, Ph.D.). Tom Levy would like to warmly thank Norma Kershaw for her support, and we are especially grateful to Liz Anne and Phokion Potamianos of La Jolla, California, for their generous support of this project given to Tom Levy and the Scripps Center for Marine Archaeology. Richard Norris would like to thank Dr. Katie Cramer for assistance in organizing the shipment of core pipe and other gear to Greece for this study.

## References

- Ainsworth, R. A. (2012). *Stereo panoramic photography for virtual reality*. Ridgeway: Ainsworth & Partners.
- Aitken, M. J. (1974). *Physics and archaeology*. Oxford: Clarendon Press.
- Annan, P. A. (1992). Ground Penetrating Radar: workshop notes. Sensors and Software, Mississauga, Ontario.
- Barker, R. D. (1992). A simple algorithm for electrical imaging of the subsurface. *First Break*, 10, 53–63.
- Ben-Shlomo, D., Shai, I., Zukerman, A., & Maeir, A. M. (2008). Cooking identities: Aegean-style cooking jugs and cultural interaction in iron age Philistia and neighboring regions. *American Journal of Archaeology*, 112(2), 225–246.
- Chovalopoulou, M., Bertsatos, A., & Manolis, S. (2017). Identification of skeletal remains from a Mycenaean burial in Kastrouli-Desfina, Greece. *Mediterranean Archaeology and Archaeometry*, 17(1), 265–269.
- Cline, E. H. (2014). *1177 B.C. : The year civilization collapsed*. Princeton: Princeton University Press.
- Constable, S., Parker, R., & Constable, C. (1987). Occam's inversion: A practical algorithm for generating smooth models from electromagnetic sounding data. *Geophysics*, 52, 289–300.
- Cramer, K. L., O'Dea, A., Clark, T. R., Zhao, J., & Norris R. D. (2017). Prehistorical and historical declines in Caribbean coral reef accretion rates driven by loss of parrotfish. *Nature Communications*, 8, 14160. <https://doi.org/10.1038/ncomms14160>:1-8.
- Dabney, M. K., Halstead, P., & Thomas, P. (2004). Mycenaean feasting on Tsoungiza at ancient Nemea. In J. C. Wright (Ed.), *The Mycenaean feast* (pp. 77–95). Athens: American School of Classical Studies at Athens.
- Davis, J. L., Alcock, S. E., Bennet, J., Lolos, Y. G., & Shelmerdine, C. W. (1997). The Pylos regional archaeological project Part I: Overview and the archaeological survey. *Hesperia: The Journal of the American School of Classical Studies at Athens*, 66(3), 391–494.
- Degroot-Hedlin, C., & Constable, S. (1990). Occam's inversion to generate smooth, two-dimensional models from magnetotelluric data. *Geophysics*, 55, 1613–1624.
- Edwards, L. S. (1977). A modified pseudosection for resistivity and IP. *Geophysics*, 42, 1020–1036.
- Fassbinder, J. W. E. (2015). Seeing beneath the farmland, steppe and desert soil: Magnetic prospecting and soil magnetism. *Journal of Archaeological Science*, 56, 85–95.
- Gidding, A., Matsui, Y., Levy, T. E., DeFanti, T., & Kuester, F. (2011, December). *e-Science and the Archaeological Frontier*. In 2011 IEEE Seventh International Conference on eScience (pp. 166–172). IEEE.
- Gidding, A., Levy, T. E., & DeFanti, T. A. (2014). ArchaeoSTOR: The development and utilization of a web-based database for the field and lab. *Near Eastern Archaeology*, 77(33), 198–202.
- Goodman, D., & Piro, S. (2013). *GPR remote sensing in archaeology*. New York: Springer.
- Goodman, D., Nishimura, Y., & Rogers, J. D. (1995). GPR time slices in archaeological prospecting. *Archaeological Prospection*, 2, 85–89.
- Griffiths, D., Turnbull, J., & Olyianka, A. (1990). 2-dimensional resistivity mapping with a computer controlled array. *First Break*, 8, 121–129.
- Knapp, A. B., & Manning, S. W. (2016). Crisis in context: The end of the Late Bronze age in the Eastern Mediterranean. *American Journal of Archaeology*, 120(1), 99–149.
- Killebrew, A. E. (2005). *Biblical Peoples and Ethnicity – An Archaeological Study of Egyptians, Canaanites, Philistines, and Early Israel, 1300–1100 B.C.E.* Atlanta: Society of Biblical Literature.
- Langgut, D., Finkelstein, I., & Litt, T. (2013). Climate and the late bronze collapse: New evidence from the Southern Levant. *Tel Aviv*, 40, 149–175.
- Langgut, D., Neumann, F. H., Stein, M., Wagner, A., Kagan, E. J., Boaretto, E., & Finkelstein, I. (2014). Dead Sea pollen record and history of human activity in the Judean highlands (Israel) from the intermediate bronze into the iron ages (~2500–500 BCE). *Palynology*, 38(2), 280–302.

- Le Borge, E. (1955). Susceptibilité magnetique anormal du sol superficial. *Annales de Geophysique*, 8(11), 399–419.
- Levy, T. E., Petrovic, V., Wypych, T., Gidding, A., Knabb, K., Hernandez, D., Smith, N. G., Schlulz, J. P., Savage, S. H., Kuester, F., Ben-Yosef, E., Buitenhuis, C., Barrett, C. J., Najjar, M., & DeFanti, T. (2010). On-site digital archaeology 3.0 and cyber- archaeology: Into the future of the past—New developments, delivery and the creation of a data avalanche. In M. Forte (Ed.), *Introduction to cyber-archaeology* (pp. 135–153). Oxford: Archaeopress.
- Levy, T. E., Najjar, M., & Ben-Yosef, E. (2014). *New insights into the iron age archaeology of Edom, southern Jordan – surveys, excavations and research from the Edom Lowlands Regional Archaeology Project (ELRAP)*. Los Angeles: Cotsen Institute of Archaeology Press UCLA.
- Linford, N. (2006). The application of geophysical methods to archaeological prospection. *Reports on Progress in Physics*, 69, 2205–2257.
- Liritzis, I., Zhengyao, J., Anchuan, F., Sideris, A., & Drivaliari, A. (2016). Late Helladic and later reuse phases of Kastrouli settlement (Greece): preliminary dating results Mediterranean. *Archaeology and Archaeometry*, 16(3), 245–250.
- Lipschitz, O., & Maeir, A. M. (2017). *The Shephelah during the iron age: Recent archaeological studies*. Winona Lake: Eisenbrauns.
- Liritzis, I., Pavlidis, G., Vosynakis, S., Koutsoudis, A., Volonakis, P., Petrochilos, N., Howland, M., Liss, B., & Levy, T. E. (2016). DELPHI4DELPHI: first results of the digital archaeology initiative for ancient Delphi, Greece. *Antiquity*, Project Gallery On-line December 2016:6 p. <http://www.antiquity.ac.uk/projgall/liritzis354>
- Marinatos, S. N. (1974). Excavations at Thera VI (1972). Athens: Vivliothiki tis en Athinis Archaeologikis Etereias 64.
- Papadopoulou, N. G., Tsourlos, P., Tsokas, G. N., & Sarris, A. (2006). 2D and 3D resistivity imaging in archaeological site investigation. *Archaeological Prospection*, 13(3), 163–181.
- Parasnis, D. S. (1997). *Principles of applied geophysics* (3rd ed.). London: Chapman and Hall.
- Raptopoulos, S. Y. (2012) ΜΥΚΗΝΑΪΚΟΣ ΘΟΛΩΤΟΣ ΤΑΦΟΣ ΣΤΗ ΔΕΣΦΙΝΑ ΦΩΚΙΔΟΣ. In ΑΡΧΑΙΟΛΟΓΙΚΟ ΕΡΓΟ ΘΕΣΣΑΛΙΑΣ ΚΑΙ ΣΤΕΡΕΑΣ ΕΛΛΑΔΑΣ (pp. 1071–1078).
- Scollar, I., Weidner, B., & Segeth, K. (1986). Display of archaeological magnetic data. *Geophysics*, 51(3), 623–633.
- Sherratt, A. (1993). What would a bronze-age world system look like? Relations between temperate Europe and the Mediterranean in later prehistory. *Journal of European Archaeology Archive*, 1(2), 1–58.
- Shima, H. (1990). 2-D automatic resistivity inversion technique using alpha centers. *Geophysics*, 55, 682–694.
- Sideris, A. (2014). *Antikyra history & archaeology*. Athens: Municipality of Distomo.
- Sideris, A., Liritzis, I., Liss, B., Howland, M., & Levy, T. E. (2017). At-risk cultural heritage: New excavations and finds from the Mycenaean site of Kastrouli, Phokis, Greece. *Mediterranean Archaeology and Archaeometry*, 17(1), 271–285.
- Simpson, R. H. (2014). Mycenaean sites in Messenia. In R. H. Simpson (Ed.), *Mycenaean Messenia and the Kingdom of Pylos* (Vol. 45, pp. 15–44). Philadelphia: INSTAP Academic Press.
- Smith, N. G., & Levy T. E. (2012). Real-time 3D archaeological field recording: ArchField, an open-source GIS system pioneered in Jordan. *Antiquity*, 85(331):on-line <http://antiquity.ac.uk/projgall/smith331/>
- Smith, N. G., & Levy, T. E. (2014). ArchField in Jordan: Real-time GIS data recording for archaeological excavations. *Near Eastern Archaeology*, 77(3), 166–170.
- Smith, N. G., Howland, M., & Levy, T. E. (2015). *Digital archaeology field recording in the 4th dimension: ArchField C++ a 4D GIS for Digital Field Work* (pp. 251–258). Granada: Digital Heritage.
- Smith, R. E., Breeze C., Harman T., Gupta A., Reece F., Liss B., Burton M. M., & Levy T. E. (2017). *ArchaeoSTOR: A User-Friendly Archaeological Database*. Poster presentation at the 45th Computer Applications & Quantitative Methods in Archaeology International Conference, March 14–16, 2017, Atlanta, Georgia.

- Strasser, T. F. (2010). Location and perspective in the Theran Flotilla Fresco. *Journal of Mediterranean Archaeology*, 23(1), 3–26.
- Tartaron, T. F. (2013). *Maritime networks in the Mycenaean world*. New York: Cambridge University Press.
- Thomatos, M. (2006). *The final revival of the Aegean bronze age : A case study of the Argolid, Corinthia, Attica, Euboea, the Cyclades and the Dodecanese during LH III C middle*. Oxford: Archaeopress.
- Tite, M. S., & Mullins, C. (1971). Enhancement of the magnetic susceptibility of soils on archaeological sites. *Archeometry*, 13(2), 209–219.
- Tsourlos, P. (1995). *Modeling interpretation and inversion of multielectrode earth resistivity datasets*. Ph. D. Thesis. University of York.
- Tsourlos, P., & Ogilvy, R. D. (1999). An algorithm for the 3-D inversion of tomographic resistivity and induced polarisation data: Preliminary results. *Journal of the Balkan Geophysical Society*, 2(2), 30–45.
- Tsourlos, P., Szymanski, J., Dittmer, J. & Tsokas, G. N. (1993). The use of back-projection for fast inversion of 2-D resistivity data. *Proceedings of the 2nd congress of the Greek Geophysical Union, Florina Greece, 5–7 May*, Vol. 1, 71–81.
- Tsourlos, P., Dittmer, J. & Szymanski, J. (1995). A study of non-linear techniques for the 2- D inversion of earth resistivity data. Expanded abstracts of the 57th meeting of the EAEG, Glasgow, Scotland, 29 May-2 June.
- Tsourlos, P., Szymanski, J., & Tsokas, G. N. (1999). The effect of terrain topography on commonly used resistivity arrays. *Geophysics*, 64, 1357–1363.
- Van de Moortel, A. (2009). Middle Bronze Age Boat of Mitrou, Central Greece. *Between continents : proceedings of the Twelfth Symposium on Boat and Ship Archaeology* (pp. 17–26), Istanbul Istanbul: Ege Yayinlari.
- Ward, S. H. (1990). Resistivity and induced polarization methods. In: S. H. Ward (Ed.), *Geotechnical and environmental geophysics 1: Review and tutorial (Investigations in Geophysics 5)* (pp. 147–189). Tulsa: SEG.
- Wedde, M. (2000). *Towards a hermeneutics of Aegean bronze age ship imagery*. Mannheim: Bibliopolis.
- Weiner, M. H. (n.d.). *The impact of climate change, famine, pandemics, and warfare in the collapse of civilizations*. Greece: On file: INSTAP.
- Witten, A. (2006). *Handbook of geophysics and archaeology*. London: Equinox.
- Wright, J. C. (Ed.). (2004). *The Mycenaean feast*. Princeton: American School of Classical Studies at Athens.